博士論文

Strain tuning and piezoresistive detection in MEMS beam resonators for terahertz bolometer applications

（テラヘルツボロメータ応用に向けた MEMS 梁共振器構造における
歪みチューニングとピエゾ抵抗効果に関する研究）

令和 3 年 6 月 1 日提出

指導教員　　　平川　一彦　教授

東京大学大学院　工学系研究科

電気系工学専攻

37-187251　　邱　博奇

Strain tuning and piezoresistive detection in MEMS beam resonators for terahertz bolometer applications

（テラヘルツボロメータ応用に向けた MEMS 梁共振器構造における
歪みチューニングとピエゾ抵抗効果に関する研究）

A Dissertation submitted to
Department of Electrical Engineering and Information Systems
The University of Tokyo

for the degree of
Doctor of Engineering

presented by
QIU Boqi
born 15th July 1994

supervised by
Professor HIRAKAWA Kazuhiko

June 2021

Acknowledgement

During my PhD research, I have received supports, helps, suggestions and encouragements from many people. Without them, I cannot finish this thesis.

First of all, I would like to express my deepest and sincerest appreciation to my supervisor, Professor Kazuhiko Hirakawa for all supports he has provided throughout my course of this thesis. He is can outstanding scientist, his explanation on complicated solid physics is always simple and easy understanding. I learned a lot from his broad knowledge and also passion for the research. His altitude on research always encourages me to do better. I also appreciate for his helping me revise the paper manuscripts, conference abstracts, presentation slides and research proposals. I am sorry for my poor expressions and writing skills, and your fruitful rehearsals greatly helped me improve my skills.

I want to express my deep gratitude to my close collaborator, Professor Ya Zhang. He worked as a tutor in my experiments. He taught me almost every detail about the MEMS resonator, from theory to experiment. He taught me the using of all complicated machines with detailed instructions and great patience. He is an outstanding researcher, discussions with him always bring me new insights. I wish him every success in his new position.

I would like to thank Mr. Suguru Hosono for his teaching me doing fabrication and measurement when I first joined the group. I would like to thank Dr. Naomi Nagai for her credible sample growth. I want to show thanks to all of my formers and current members in our group for their discussions and helps in everyday life: Dr. Yukiko Otsuka, Dr. Kenji Yoshida, Dr. Shaoqing Du, Dr. Marc Bescond, Dr. Kazuyuki Kuroyama, Dr. Sylvain Chambon, Dr. Chiu-Chun Tang, Dr. Aymen Yangui, Dr. Chloe Salhani, Dr. Nobuaki Watanabe, Dr. Akira Aiba, Mr. Chenyang Li, Mr. Takuma

Abstract

In this thesis, effect of internal strain and detection scheme on doubly clamped MEMS beam is investigated for THz bolometer applications. Previously, we reported a very sensitive bolometer structure by using a GaAs doubly clamped beam resonator. The MEMS resonator detects THz radiation by measuring a shift in its resonance frequency induced by heating of the MEMS beam due to THz absorption. Speed of the device can be up to 10kHz, which is much faster than other kinds of room temperature THz thermal sensors. The MEMS bolometers are superior to other room-temperature THz bolometers, but still not comparable with the low temperature detectors in aspect of the sensitivity and speed.

In order to realize a high sensitivity, high speed MEMS bolometer for THz detection, a common method to modify the speed and sensitivity is to change the thermal conductance of the MEMS beam. A small thermal conductance of the bolometer indicates a large temperature rise and good sensitivity, but the thermal time constant also increases which means a low detection speed. Such a trade-off always exists and limits the performance of common bolometers.

In this thesis, we have proposed to obtain the high sensitivity and high speed of the MEMS bolometer by using short InGaAs MEMS beam detected by piezoresistive detection. This method can evade the speed-sensitivity trade-off of the MEMS bolometer. Changing the beam material to InGaAs provides a high thermal responsivity, the short MEMS beam provides a high speed and the piezoresistive detection provides a large output voltage.

Outline of this thesis is shown as follows.

In Chapter 2, the operation principle of the MEMS bolometer is explained. In this work, a GaAs doubly clamped MEMS beam resonator is used to detect THz radiations.

When the beam is heated by THz radiation, the temperature rise is detected as a resonance frequency shift of the beam. A long beam has a small thermal conductance. It can keep the THz heat and show a high responsivity but a low speed. Such a trade-off exists and we cannot obtain the high sensitivity and high speed at the same time.

In Chapter 3, origins of a deflection in the MEMS beam are discussed. Such a deflection brings difference from the theory to the experiment result of the MEMS bolometers and makes it difficult to predict the devices' performance. We found that there are two factors that induce the beam deflection. First is the initial bending of the MEMS beam. To reduce the bending, we introduce a tensile strain to the MEMS beam using GaAsP as the beam structure and finally we reduced the deflection from 150 nm to 50 nm. Another reason of the beam deflection is a step structure on the beam surface. The step structures are used for driving and detection of the beam vibration. We reduced the step height and finally the deflection is reduced to as small as 10 nm. Fabrication and measurement of the MEMS beam is also introduced in this chapter.

In Chapter 4, we propose to enhance the responsivity of the MEMS bolometer by preloading a critical buckling strain. With the deflection of the beam reduced to 10 nm, the beam is nearly ideal and shows a high responsivity around its buckling point, as predicted in the theory. To achieve this high responsivity, we preload a critical buckling strain to the beam through lattice mismatch between InGaAs and the GaAs substrate. Preloading such a strain does not change the thermal conductance of the beam, so it can evade the speed-sensitivity trade-off. Finally we achieve a 15-time-enhancement of responsivity. Also, the noise density of the bolometer is introduced and, we demonstrated that the noise density of the strained beam has strong dependence on its vibration amplitude.

In Chapter 5, we will discuss the detection scheme of the MEMS beam vibration. Since the speed-sensitivity trade-off is evaded, short beams can exhibit a high sensitivity and high speed at same time. However, the piezo-capacitive detection of the present device is not suitable for detecting vibration of short beam, because the output

voltage from the piezoelectric capacitor is shunted by the stray capacitance of measurement cables and shows smaller than 1 μV. Therefore, we need to develop another detection scheme. Piezoresistive effect is suitable for the detection of the short beams. Since the resistance is determined by *L/W* ratio of a resistor, the output voltage is not affected be the beam length decrease. We designed MEMS beams with piezoresistive detection, and tried NiCr film, 2D electrons and 2D holes as piezoresistive materials. Results shows that by using 2D holes as the piezoresistive material, the output voltage increases to as large as 10 mV which is 10000 times of that of the piezo-capacitive detection. Also, effect of the source voltage and the crystallographic orientation is discussed. both of which has influence on the detection performance.

In Chapter 6, a conclusion and an outlook for future development is also given.

Table of Contents

Chapter 1
Introduction

1.1   Terahertz electromagnetic waves

Terahertz (THz) radiation usually means the electromagnetic radiation within the frequency range from 0.3 to 3 THz (1 THz = 10^{12} Hz). The wavelength of the radiation correspondingly ranges from 1 mm to 0.1 mm. THz radiation occupies the frequency range between the microwaves and the infrared light. As a result, THz radiation possesses characteristics of both microwave and infrared light and has numerous attractive applications. As in the microwave range, THz waves can be used in the field of communications. Since THz has a higher frequency, it is expected to realize a higher speed wireless data transmission. A group from Tokyo Institute of Technology[1] demonstrated that they use a resonant tunneling diode (RTD) oscillator to produce radiation in the THz band and send a signal at 0.542 THz, resulting in a data transfer rate of 3 Gbps. Potential use of THz communication exists in in-door network systems and space technologies. On the other hand, because of the long wavelength of the THz radiation, it can penetrate a wide variety of nonconducting materials such as clothing, paper, wood, plastic and ceramics. Unlike X-rays, THz waves is not an ionizing radiation and its low photon energies in general do not damage living tissues and DNA. Therefore, the THz nondestructive imaging is widely used for biomedical, security, material characterization applications.
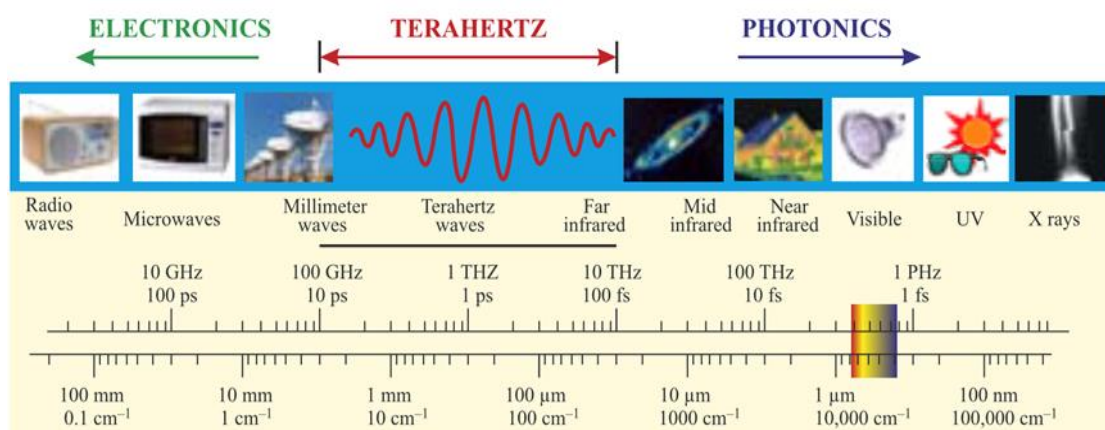

Fig. 1-1 Terahertz waves lie at the far end of the infrared band, just before the start of the microwave band.

1.2   Conventional THz detectors

Although the THz radiation is expected to have a wide range of applications, THz technology is still in its infancy. Particularly, the technology for detecting THz radiation is rather limited. The small photon energy of the THz radiation requires the THz detectors based on photoexcitation of impurities and quantum wells to be cooled down to liquid helium temperatures, which greatly limits their applications. In the following three kinds of THz detectors will be introduced.

Schottky barrier diodes (SBDs) are one of the most basic THz detectors. SBD THz detectors take use of the nonlinearity in the I-V characteristics to rectify THz waves, as shown in Fig. 1-2(a).[2] This kind of THz detector can work at the room temperature, with a low noise equivalent power (NEP) around ~10 pW/Hz$^{1/2}$. However, the useful frequency range is limited due to the existence of junction capacitance.[3] Fig. 1-2(b) shows the dependence of the voltage sensitivity on frequency.[4]

Another kind of THz detector is bolometer, which measures the electrical resistance change induced by radiation heating. One of the most famous THz bolometer is composite bolometer, which consists of two elements perform separately the two functions of absorption and bolometric detection,[5–7] as shown in Fig. 1-3. The absorbers can be made with metallic films deposited on dielectric substrates and works as broadband absorbers. The bolometric detection is accomplished by semiconductor thermometers such as Ge and Si thermometers. Although, in principle the composite bolometers can work in room temperature, cooling is necessary for high sensitivities.

Vanadium oxide (VOx) is a recently developed temperature sensing material works at room temperature which can be used as the bolometric detection material in composite bolometers. Such material has a large temperature coefficient of resistance, around 3%/K.[8,9] Fig. 1-4 shows an example of VOx bolometer, the device shows a low NEP around ~40 pW/Hz$^{1/2}$ at room temperature, but the operation speed is lower than 100Hz.[10]

In order to realize high sensitivity, high speed detection, wide band THz radiations at room temperature, new schemes of THz detection are highly desirable.
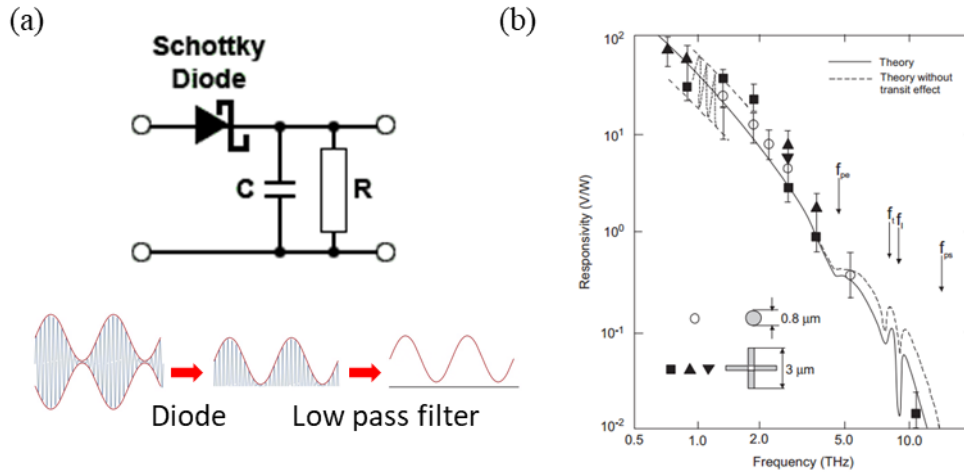

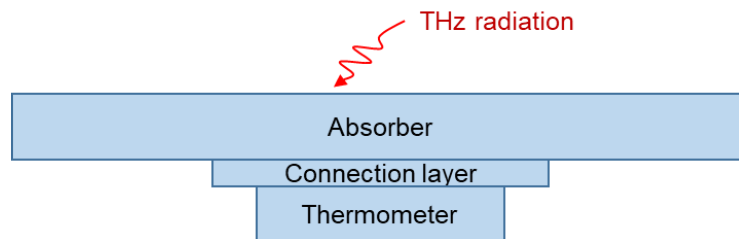Fig. 1-2 Schottky barrier diodes used as THz detectors.
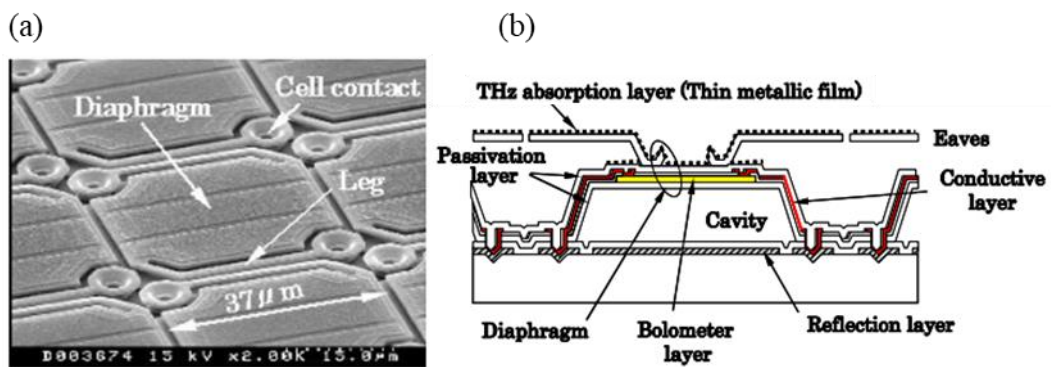

Fig. 1-3 Schematic of composite bolometers.

Fig. 1-4 VOx bolometer: (a) SEM image, (b) schematic cross section .

1.3   Novel THz bolometers using MEMS resonators

Microelectromechanical system (MEMS) resonators are very attractive candidates for high sensitivity measurements. Owing to their high quality (Q) factors,[11,12] the MEMS resonators can detect ultra-small changes in the resonance frequency. Such properties are suitable for detecting changes in mass,[13–22] charge,[23–27] spin orientation,[28,29] temperature,[30–33] and infrared radiation.[34–39]

Previously, we reported a very sensitive bolometer structure by using a MEMS resonator.[40–47] As shown in Fig. 1-5, we fabricated a GaAs doubly clamped beam resonator, whose excitations are driven and detected by utilizing the piezoelectric effect.[28,48–51] When the MEMS beam absorbs THz power and a temperature rise of the beam is induced, a strain is generated in the MEMS beam due to thermal expansion and leads to the reduction in the resonance frequency. The device detects the resonance frequency shift caused by radiation heating and works as a very sensitive bolometer, which can detect a small temperature rise (~1 µK) in the beam with a high operation speed (~10 kHz). Fig. 1-6 illustrates the principle of THz detection.

The MEMS bolometer is superior to other room temperature THz detectors, but still not good as the ones works in low temperatures. Fig. 1-7 plots the performance of the MEMS bolometer compared with other kinds of commercial THz detectors. Compared with the room temperature detectors such as pyroelectric (PE) detectors and vanadium oxide detectors, the MEMS bolometer shows a good sensitivity and 100 times faster speed, but it is still 2~3 orders lower than that of the hot electron bolometers (HEB) which works at liquid helium temperature. Such shortage in sensitivity and speed limits the application of the MEMS bolometer in the field of broadband spectroscopy such as Fourier transform infrared (FTIR) spectroscopy, where high sensitivity and high speed are necessary for measuring short wavelength signals.[52]

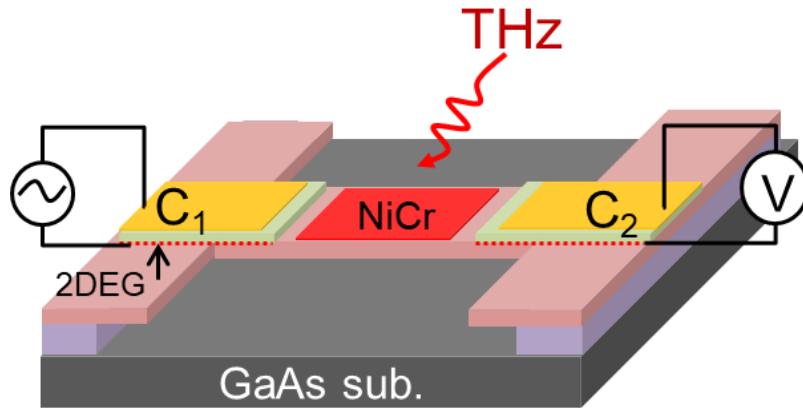Fig. 1-5 Schematic of MEMS beam resonator as THz bolometer.
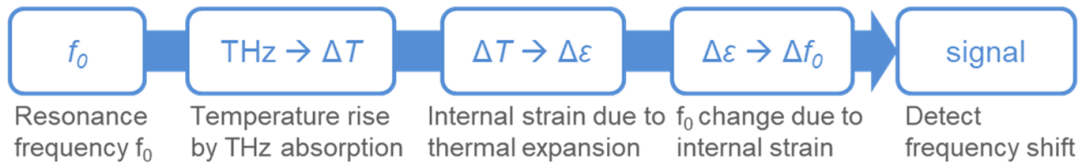

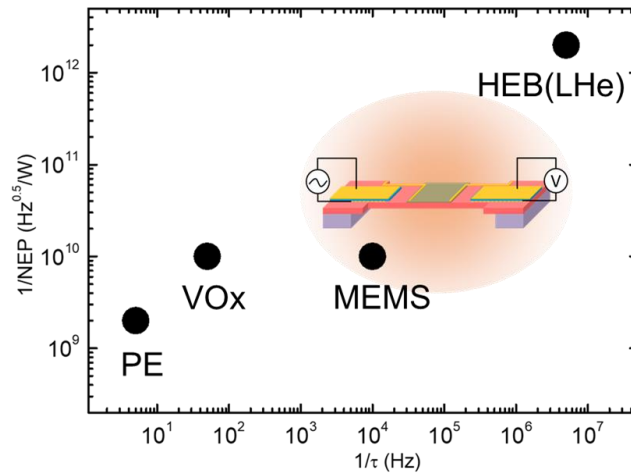Fig. 1-6 Principle of THz detection using MEMS beam resonator.

Fig. 1-7 Performance of the MEMS bolometer compared with other kinds of commercial THz detectors. The horizontal axis shows the sensitivity and the vertical axis shows the speed.

1.4 Research purpose and outline

In this thesis, the detection performance of GaAs-based doubly clamped MEMS beam bolometer is investigated. We aim at realizing a high sensitivity, high speed MEMS bolometer for THz detection. A common method to modify the speed and sensitivity is to change the thermal conductance of the bolometer (in our case, the MEMS beam). A small thermal conductance of the bolometer indicates a large temperature rise and good sensitivity, but the thermal time constant also increases which means a low detection speed. Such a trade-off always exists and limits the performance of common bolometers.

In order to obtain the high sensitivity and high speed at the same time, we propose to evade the speed-sensitivity trade-off and enhance the responsivity of the MEMS bolometer by tuning the strain. Outline of this thesis is shown as follows.

In Chapter 2, the operation principle of the MEMS bolometer is explained. In this work, a GaAs doubly clamped MEMS beam resonator is used to detect THz radiations. When the beam is heated by THz radiation, the temperature rise is detected as a resonance frequency shift of the beam. A long beam has a small thermal conductance. It can keep the THz heat and show a high responsivity but a low speed. Such a trade-off exists and we cannot obtain the high sensitivity and high speed at the same time.

In Chapter 3, origins of a deflection in the MEMS beam are discussed. Such a deflection brings difference from the theory to the experiment result of the MEMS bolometers and makes it difficult to predict the devices' performance. We found that there are two factors that induce the beam deflection. First is the initial bending of the MEMS beam. To reduce the bending, we introduce a tensile strain to the MEMS beam using GaAsP as the beam structure and finally we reduced the deflection from 150 nm to 50 nm. Another reason of the beam deflection is a step structure on the beam surface. The step structures are used for driving and detection of the beam vibration. We reduced the step height and finally the deflection is reduced to as small as 10 nm. Fabrication

and measurement of the MEMS beam is also introduced in this chapter.

In Chapter 4, we propose to enhance the responsivity of the MEMS bolometer by preloading a critical buckling strain. With the deflection of the beam reduced to 10 nm, the beam is nearly ideal and shows a high responsivity around its buckling point, as predicted in the theory. To achieve this high responsivity, we preload a critical buckling strain to the beam through lattice mismatch between InGaAs and the GaAs substrate. Preloading such a strain does not change the thermal conductance of the beam, so it can evade the speed-sensitivity trade-off. Finally we achieve a 15-time-enhancement of responsivity. Also, the noise density of the bolometer is introduced and, we demonstrated that the noise density of the strained beam has strong dependence on its vibration amplitude.

In Chapter 5, we will discuss the detection scheme of the MEMS beam vibration. Since the speed-sensitivity trade-off is evaded, short beams can exhibit a high sensitivity and high speed at same time. However, the piezo-capacitive detection of the present device is not suitable for detecting vibration of short beam, because the output voltage from the piezoelectric capacitor is shunted by the stray capacitance of measurement cables and shows smaller than 1 µV. Therefore, we need to develop another detection scheme. Piezoresistive effect is suitable for the detection of the short beams. Since the resistance is determined by L/W ratio of a resistor, the output voltage is not affected be the beam length decrease. We designed MEMS beams with piezoresistive detection, and tried NiCr film, 2D electrons and 2D holes as piezoresistive materials. Results shows that by using 2D holes as the piezoresistive material, the output voltage increases to as large as 10 mV which is 10000 times of that of the piezo-capacitive detection. Also, effect of the source voltage and the crystallographic orientation is discussed. both of which has influence on the detection performance.

In Chapter 6, a conclusion is given. To achieve high responsivity and high speed of the MEMS bolometer, we propose to use short InGaAs MEMS beam detected by

piezoresistive detection. Changing the beam material to InGaAs provides a high thermal responsivity, the short MEMS beam provides a high speed and the piezoresistive detection provides a large output voltage. Also, an outlook for future development is also given.

Chapter 2

Operation principle of MEMS bolometers

2.1　　Properties of beam structure

The Euler-Bernoulli beam theory is a simplification of the linear theory of elasticity which provides a means of calculating the characteristics of beams.

For a thin uniform beam ($L/h > 10$, Fig. 2-2), the rotational inertia and the shear deformation can be neglected. The equation of motion of a thin beam can be derived by means of the equilibrium of forces for an infinitesimal piece of beam. Assuming a linear elastic material and a small displacement $Y(x, t)$, the equation of motion of a thin beam is[53–55]

$$\rho A \frac{\partial^2 Y(x,t)}{\partial t^2} + EI_z \frac{\partial^4 Y(x,t)}{\partial x^4} = 0 \,, \tag{2-1}$$

where ρ is the mass density, A is the cross sectional area, E is the Young's modulus, and I_z is the geometric moment of inertia, which, for a beam with rectangular cross section, can be derived as:

$$I_z = \frac{Ah^2}{12} \tag{2-2}$$

The solutions of Eq. 2-1 have the form:

$$Y(x, t) = [C_1 \cos \beta x + C_2 \sin \beta x + C_3 \cosh \beta x + C_4 \sinh \beta x]\, e^{-i\omega t} \tag{2-3}$$

where coefficients C_1, C_2, C_3, C_4 and the value of β can be found from the boundary conditions, and natural frequencies of the beam are given as:

$$f = \beta^2 \sqrt{\frac{EI}{\rho A}} \tag{2-4}$$

For doubly clamped beams, the boundary conditions are as follows:

$$Y(0,t) = Y(L,t) = 0$$
$$\frac{\partial Y(0,t)}{\partial x} = \frac{\partial Y(L,t)}{\partial x} = 0$$

(2-5)

Substituting Eq. 2-5 into Eq. 2-1 and finally we get solution:

$$Y_n(x,t) = C_n[\sin\beta_n x + \sinh\beta_n x + \alpha_n(\cos\beta_n x + \cosh\beta_n x)]e^{-i\omega_n t}$$

(2-6)

where

$$\alpha_n = \left(\frac{\sin\beta_n L - \sinh\beta_n L}{\cosh\beta_n L - \cos\beta_n L}\right)$$

(2-7)

$$\cos\beta_n L \cdot \cosh\beta_n L = 1, \beta_n^2 \cong (2n+1)\pi/2L^2$$

Mode shape describes vibration amplitude of a beam, which is the contour of Y_n:

$$S_n(x) = C_n[\sin\beta_n x + \sinh\beta_n x + \alpha_n(\cos\beta_n x + \cosh\beta_n x)]$$

(2-8)

In the n-th mode, each point of the beam vibrates with an amplitude proportional to the value of S_n at that point. Calculations of mode shape for the first three modes are shown in Fig. 2-1. The mode corresponding to $n=1$ is called the fundamental mode.
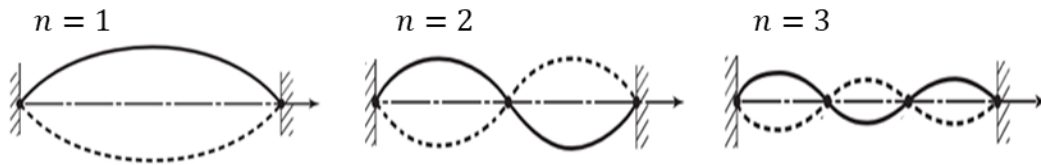
Fig. 2-1 Mode shapes of a doubly clamped beam.

The natural frequencies of doubly clamped beam are given by

$$f_n = \frac{(2n+1)\pi}{2}\frac{h}{L^2}\sqrt{\frac{E}{12\rho}} \tag{2-9}$$

where f_1 is called the fundamental frequency, which can be derived as:

$$f_1 = 1.028\frac{h}{L^2}\sqrt{\frac{E}{\rho}} \tag{2-10}$$

General solution of Eq. 2-1 is given by the sum of all Y_n:

$$Y(x,t) = \sum_n a_n Y_n(x,t) \tag{2-11}$$
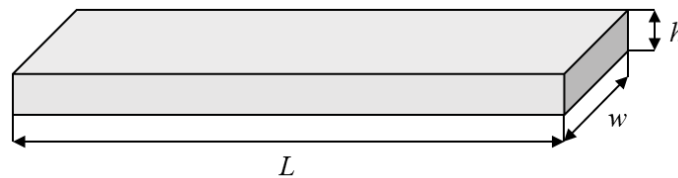
Fig. 2-2 A thin beam.

2.2 Vibration of beam structure

When we apply a harmonic driving force $Fe^{i2\pi f_c t}$ which is uniform in the beam direction, the equation of motion is[56]

$$\rho A \frac{\partial^2 Y(x,t)}{\partial t^2} + EI_z \frac{\partial^4 Y(x,t)}{\partial x^4} = Fe^{i2\pi f_c t} \tag{2-12}$$

Substituting Eq. 2-11 into Eq. 2-12, assuming that driving frequency f_c is close to f_n, then we get the amplitude of n-th mode:

$$a_n = \frac{F}{4\pi^2 M} \frac{\eta_n}{f_n^2 - f_c^2 + if_n^2/Q} \tag{2-13}$$

where $M = \rho AL$ is the mass of the beam, $\eta_n = \int_0^L W_n(x)dx / L^2$ is a constant with $\eta_1 = 0.8309$, Q is the quality factor of the system.

Then we get the amplitude and phase of forced vibration as the real part and imaginary part of a_n:

$$\begin{cases} A_n = \dfrac{F}{4\pi^2 M} \dfrac{\eta_n}{\sqrt{(f_n^2 - f_c^2)^2 + (f_n^2/Q)^2}} \dfrac{F}{M} \\ \theta = \tan^{-1} \dfrac{f_n^2/Q}{f_n^2 - f_c^2} \end{cases} \tag{2-14}$$

Calculations of amplitude and phase of the forced vibration are shown in Fig. 2-3. When the driving frequency $f_c = f_n$, the beam vibration shows maximum amplitude, this frequency is called resonance frequency.
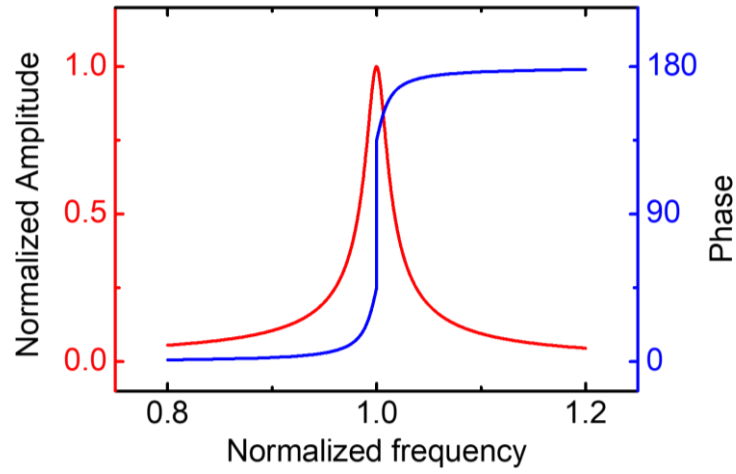
Fig. 2-3 Calculated resonance spectra of forced vibration.

2.3   Influence of axial strain

Assuming that an axial compression N is induced by a displacement u of the clamped ends, as shown in Fig. 2-4. Mention that $\varepsilon = u/L$ represents the strain induced in the beam, we have

$$N = \hat{E} A \varepsilon = \hat{E} A \frac{u}{L} \tag{2-15}$$

where $\hat{E}$ is the Young modulus modified with the Poisson ratio ν

$$\hat{E} = \frac{E}{1 - \nu^2} . \tag{2-16}$$
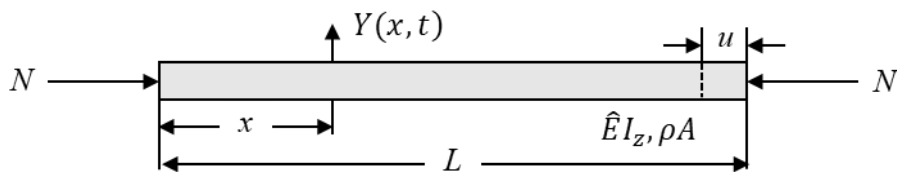
Fig. 2-4 Axial load N result a displacement u and induce an internal strain ε

The equation of motion of a thin beam with compressive strain can be described by:[57]

$$\rho A \frac{\partial^2 Y(x,t)}{\partial t^2} + \hat{E} I_z \frac{\partial^4 Y(x,t)}{\partial x^4} = N \frac{\partial^2 Y(x,t)}{\partial x^2} \; . \tag{2-17}$$

The natural frequency of the strained beam is given by:

$$f_n(\varepsilon) = f_n(0) \sqrt{\left(1 - \gamma_n \frac{L^2}{h^2} \varepsilon\right)} \; , \tag{2-18}$$

and γ_n is a constant related with β_n:

$$\gamma_n = \frac{12(\beta_n - 2)}{\beta_n^3} \; , \gamma_1 = \frac{3}{\pi^2} \; . \tag{2-19}$$

Fig. 2-5 plots the relationship between the normalized fundamental frequencies ($n = 1$) and the normalized axial load.
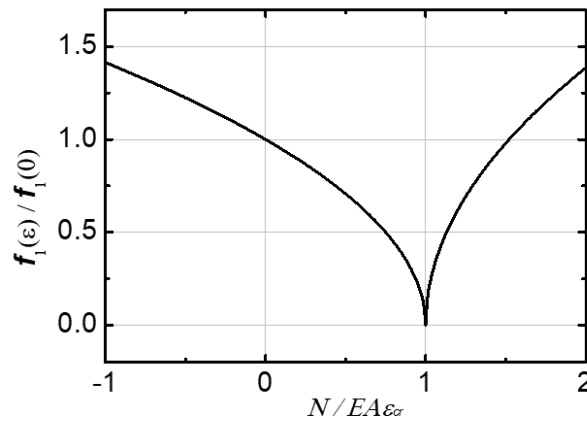
Fig. 2-5 Resonance frequency change with the axial load.

With an increasing compress strain, the resonance frequency first decreases until a critical load called the Euler's critical load is reached and, then, starts to increase. The Euler's critical load is given by the formula:[58]

$$\varepsilon_{cr} = \frac{\pi^2 h^2}{3L^2}$$ (2-20)

The Euler's theory shows that, with increasing N, the internal strain first increases and the beam stays flat. However, the beam cannot support a strain larger than the critical load and, with further increase in N, the beam is buckled. The critical load is smaller for longer beams: for beams with geometry of L100×W30×H1.2 μm^3 the critical strain is around 0.03%, while for beam as long as 1000 μm, the critical load decreases by 100 times.

2.4　　Thermal responsivity of MEMS resonance frequencies

In chapter 1.3, we described the working principle of the THz detection using MEMS beam resonator: when a MEMS beam absorbs THz power P_{in} and has a temperature rise ΔT, a strain $\Delta \varepsilon$ is induced in the beam due to thermal expansion, leading to the natural frequency decrease by Δf.

Principle of THz detection by MEMS
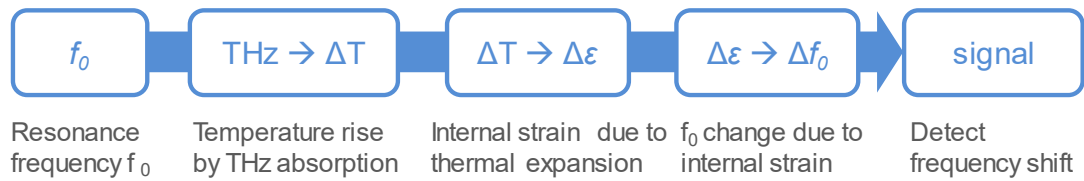
Fig. 2-6 Principle of THz detection using MEMS beam resonator

Thermal responsivity of MEMS beam resonator, defined as the relative frequency shift per unit heating power, is given by:

$$R = \frac{\Delta f}{P_{in}} \frac{1}{f_0} = \frac{\Delta T}{P_{in}} \cdot \frac{\Delta \varepsilon}{\Delta T} \cdot \frac{\Delta f}{\Delta \varepsilon} \cdot \frac{1}{f_0} \tag{2-21}$$

where the right side of Eq. 2-21 is consist of the temperature rise, thermal expansion and frequency decrease process of THz detection.
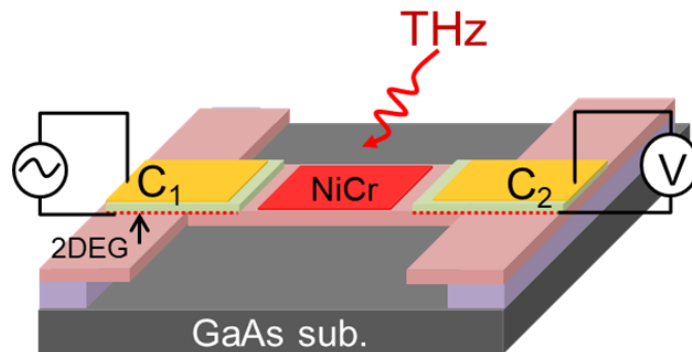
Fig. 2-7 Schematic of MEMS beam resonator as THz bolometer.

2.4.1 Temperature rise

Fig. 2-8 shows a schematic of heat transfer in the MEMS beam. When the center part of the beam (l_1) is heated with a heating power of P_{in}, the temperature rises by ΔT. Then, the heat flows to each end of the beam with a power of P_{out}.
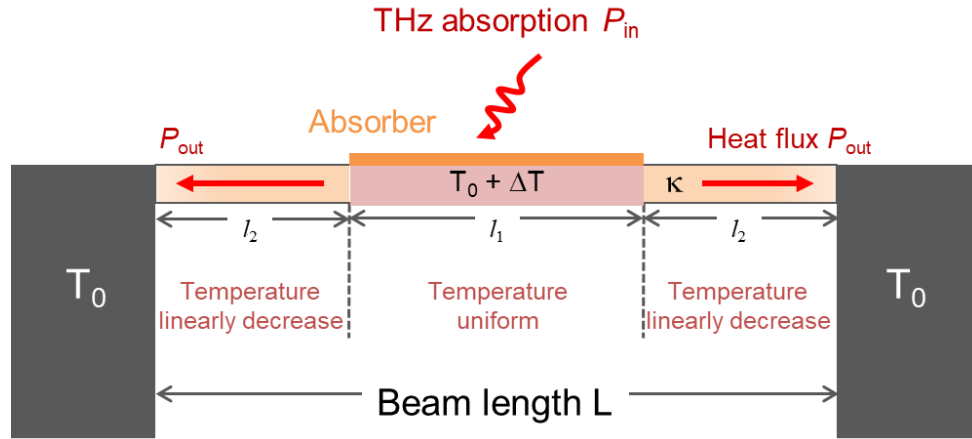
Fig. 2-8 Schematic of heat transfer in a MEMS beam.

Fourier's law describes the process of thermal conduction. According to the Fourier's law, the power of heat transfer through a material is proportional to the gradient in the temperature and to the area:

$$P_{out} = \kappa A \frac{\Delta T}{l_2} \tag{2-22}$$

where κ is the thermal conductivity and $l_2 = (L - l_1)/2$

When $P_{in} = 2P_{out}$, the process is in a steady state, and the relationship between heating power and temperature rise can be written:

$$\frac{\Delta T}{P_{in}} = \frac{L - l_1}{4\kappa A} . \tag{2-23}$$

2.4.2   Thermal expansion

For a free beam of length L, the thermal expansion in the linear dimension can be estimated to be:

$$\frac{\Delta L}{L} = \alpha_L \Delta T \ , \tag{2-24}$$

where α_L is the coefficient of thermal expansion.

As shown in Fig. 2-8, thermal expansion of the beam can be divided into two parts; in the center part, the beam is directly heated and has a uniform temperature rise of ΔT. Thermal expansion of this part is given by:

$$\Delta l_1 = \alpha_L \Delta T l_1 \tag{2-25}$$

On the other hand, on both sides of the beam, which are not heated, the temperature linearly decreases to the end of the beam, and the thermal expansion of this part comes with:

$$\Delta l_2 = \int_0^{l_2} \alpha_L \Delta T \frac{x}{l_2} dx$$
$$= \alpha_L \Delta T \frac{L - l_1}{4} \ . \tag{2-26}$$

For a doubly clamped beam, strain $\Delta \varepsilon$ is induced in the beam direction instead of displacement:

$$\Delta \varepsilon = \frac{\Delta L}{L} \ . \tag{2-27}$$

With the total displacement of $\Delta L = l_1 + 2l_2$, the relationship between thermal

expansion and temperature rise:

$$\frac{\Delta \varepsilon}{\Delta T} = \frac{\Delta l_1 + 2\Delta l_2}{L} \frac{1}{\Delta T}$$

$$= \frac{1}{2} \alpha_L \left(1 + \frac{l_1}{L}\right) \ .$$

(2-28)

2.4.3　Frequency decrease

In Chapter 2.3 we calculated the natural frequency of doubly clamped flat beam with an axial strain ε:

$$f_n(\varepsilon) = f_n(0) \sqrt{\left(1 - \gamma_n \frac{L^2}{h^2} \varepsilon\right)} \ .$$

(2-29)

When $\gamma_n \frac{L^2}{h^2} \varepsilon \ll 1$, $\omega_n(\varepsilon)$ can be approximated by

$$f_n(\varepsilon) \cong f_n(0) \left(1 - \gamma_n \frac{L^2}{2h^2} \varepsilon\right) \ .$$

(2-30)

Hence, the frequency shift can be written as:

$$\Delta f_n = f_n(\Delta \varepsilon) - f_n(0)$$

$$= -\gamma_n \frac{L^2}{2h^2} \Delta \varepsilon \cdot f_n(0) \ .$$

(2-31)

Here shows the frequency shift Δf_n of the n-th mode. Since γ_n decreases with increasing n, the fundamental mode shows the largest frequency shift. It should be noted that, when there is a compressive strain $\varepsilon > 0$, the natural frequency of MEMS beam decrease.

The relationship between the fundamental frequency shift and the strain:

$$\frac{\Delta f_1}{\Delta \varepsilon} = \frac{\gamma_1}{2}\left(\frac{L}{h}\right)^2 \cdot f_0 \ .$$

(2-32)

Finally, the thermal responsivity of MEMS beam resonator for the fundamental mode can be calculated:

$$R = \frac{\Delta \omega}{P_{in}} \frac{1}{\omega_0} = \frac{\Delta T}{P_{in}} \cdot \frac{\Delta \varepsilon}{\Delta T} \cdot \frac{\Delta f}{\Delta \varepsilon} \cdot \frac{1}{f_0}$$

$$= \frac{\gamma_1 \alpha_L}{16\kappa} \frac{1}{w}\left[1 - \left(\frac{l_1}{L}\right)^2\right]\left(\frac{L}{h}\right)^3 \ .$$

(2-33)

The thermal responsivity of the MEMS bolometer is determined only by the thermal and mechanical properties, such as geometry of the MEMS beam, thermal expansion ratio and thermal conductivity of the beam material. This allows a good reproducibility of the devices.

2.5   Summary

We have considered a GaAs doubly clamped MEMS beam resonator as THz bolometer. The resonance frequency of the MEMS beam resonator can be detected by applying a harmonic driving force on the beam. When the MEMS beam is heated by THz radiation, a compressive strain is induced in the MEMS beam due to thermal expansion and cause the resonance frequency shift. By using this frequency shift we can detect the THz power. Thermal responsivity of the MEMS beam is determined only by thermal and mechanical properties, which allows a good reproducibility of the devices.

Chapter 3

Effect of the beam deflection on MEMS bolometers

3.1 Introduction

In Chap2.2, we mentioned that, when we apply a harmonic driving force $Fe^{i2\pi ft}$ to the beam and the driving frequency f_c is equal to the natural frequency f_n, the beam vibration shows maximum amplitude, which is called resonance. The resonance frequency is sensitive to the thermally induced strain. In order to measure the resonance frequency, we apply a driving force and find the frequency with maximum vibration amplitude.

In our device the driving force is applied to the MEMS beam by using piezoelectric effect. Fig. 3-1 shows a schematic of our device. On the two ends of the MEMS beam we fabricate piezoelectric capacitors, with conductive n-GaAs bottom electrodes, Au top electrodes, and undoped GaAs layer as a dielectric material. By applying a harmonic voltage between the Au electrode and the conductive n-GaAs layer, a stress along the beam direction is generated, leading to a bending moment in the beam, which causes the beam to vibrate. The inverse process happens on the other side of the beam: a vibration induced piezo-voltage, which is proportional to the vibration amplitude, is generated between the two electrodes.

Here presents one of the reasons why we use GaAs, instead of silicon: GaAs is a kind of piezoelectric material because of its asymmetrical lattice structure.
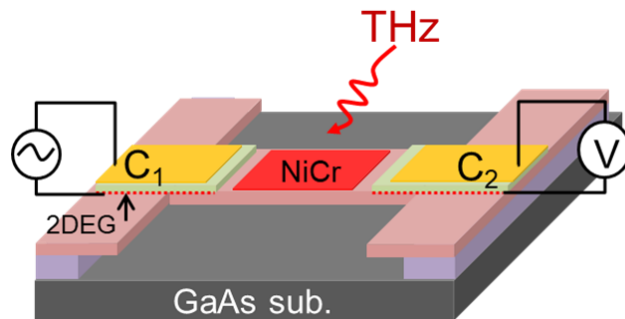
Fig. 3-1 Schematic of MEMS beam resonator as THz bolometer.

3.2 Sample fabrication process

3.2.1 Wafer structure

Fig. 3-2 shows the wafer structure of our samples. The wafer is grown on a GaAs (100) substrate, by using molecular beam epitaxy (MBE). According to the theory of piezoelectric effect, bending moment in the beam is most efficiently generated along the [110] direction,[48] which is assigned as the beam direction to improve the driving efficiency.

The wafer structure can be divided into three parts: mesa, beam, and sacrificial layer. The mesa part acts as the piezoelectric capacitor on the two ends of the MEMS beam. With a gold electrode deposited above the undoped GaAs layer, a sandwich structure of a conductive – insulating – conductive layer is formed, acting as the piezoelectric capacitor. The beam part includes a 1um GaAs layer above periodic superlattice buffer layer of GaAs and AlGaAs, which is designed to improve the flatness. The sacrificial layer can be selectively etched by diluted HF (20%) and makes the beam part suspended.

Wafer growth of GaAs samples are kindly done by Nagai-san in our group.

Fig. 3-2 Wafer structure of the MEMS resonator.

3.2.2   Mesa structure

To fabricate the mesa structure, we first design a pattern on the wafer using photoresist, then use hydrogen peroxide-phosphoric acid mixture to perform etching. The designe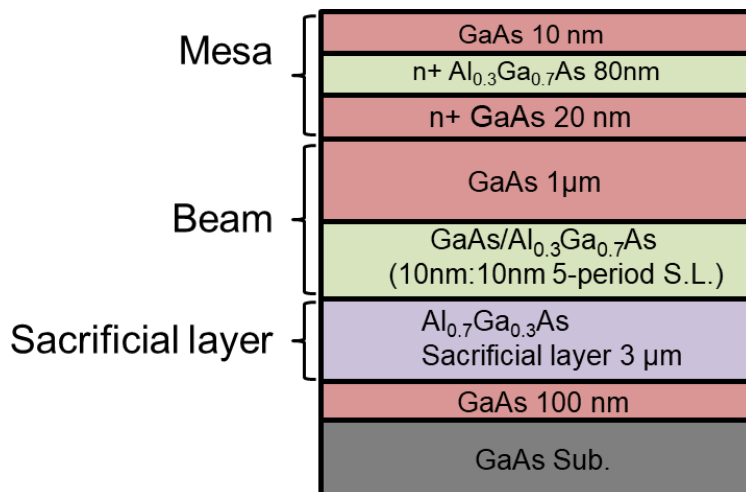d capacitor region is covered by photoresist and remains on the beam surface after mesa etching. Fig. 3-3 shows the detailed process.

We first spin-coat photoresist (Series: AZ1500) on the wafer. The rotation speed of the spin coater starts with 5s of 500 rpm, then gradually increase to 4500 rpm in 5s and continues 45s. Thickness of photoresist after spin coating is ~1 μm. After spin coating, the resist is baked at 90°C for 10 min. Photoresist used in the fabrication process was positive type: the region exposed to UV light is dissolved in the developer.

Then, we expose the sample with UV. We use a chrome photomask, which was fabricated in advance to define the patterns. Since our patterns are in a μm-scale, sample chips are directly touched with the photomask, without any zoom in or out. Typically, the time of exposure is around 10s, which depends on the intensity of UV light source. After exposure, the sample is developed in 1:1 solution of AZ-developer and water. Resist exposed to UV light is dissolved in the developer, and it takes around 90s to complete development process.

To etch the sample, we use H_3PO_4-H_2O_2-H_2O solution with a 1:1:75 ratio. The etchant is kept at 27 °C using a water bath and the etching rate is around 1 nm/s. In the H_3PO_4-H_2O_2-H_2O system, H_2O_2 acts as an oxidizer of GaAs, and H_3PO_4 removes oxides. In the presence of H_2O_2 and H_3PO_4, the etching process is done efficiently.[59]

After finishing the process, we use acetone to dissolve the photoresists, and then wash the sample chip in methanol and water.
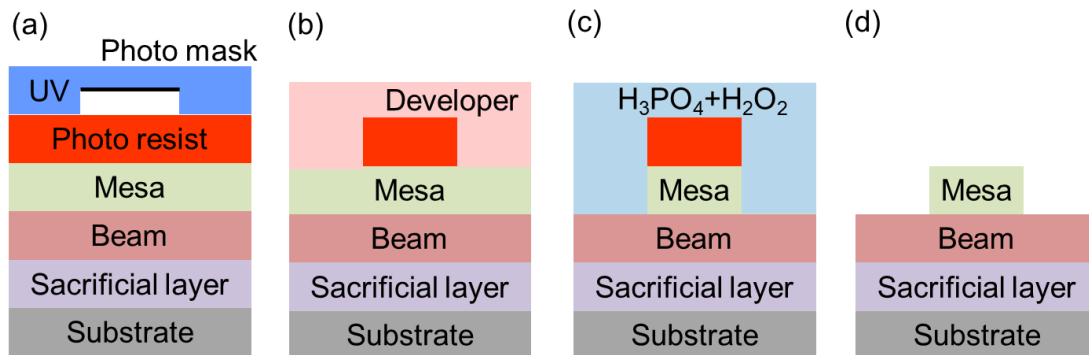
Fig. 3-3 Procedure of mesa etching: (a) Exposure (b) Develop (c) Etching (d) Remove the photo resist.
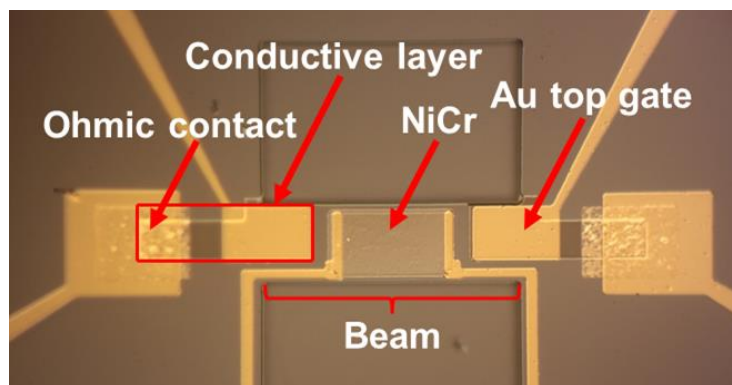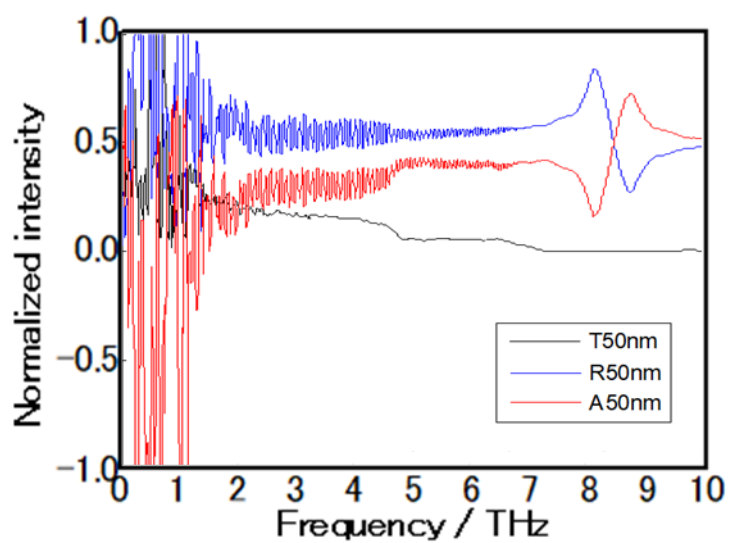

Fig. 3-4 Microscope image of fabricated sample.

Fig. 3-5 Transmission, reflection and absorption of 50nm NiCr film.

3.2.3　Metal deposition

Fig. 3-4 shows a microscope image of our sample. In the figure we can see the patterns of different metals. The metals are deposited using electron beam (EB) evaporator, in vacuum of 10^{-4} Pa.

AuGeNi (8:1:1) is deposited on the edge of mesa as an ohmic contact metal, which is subsequently annealed at an elevated temperature. AuGeNi can provide a reliable, low-resistance ohmic contact to n-type GaAs; Ni enhances the diffusion of Ge and Au enhances the out-diffusion of Ga. As a result, Ge atoms go substitutionally into Ga sites.[60] This helps to create a thin n-type highly doped layer on the GaAs surface. In our case, the sample is annealed at 450°C for 1min, in Ar gas atmosphere. The thickness of AuGeNi is 70nm, covered with 80nm gold.

NiCr (8:2) is deposited on the center of the beam structure, acting as THz absorber. The optical response of metals depends on the sheet resistivity of the conduction electrons. It is calculated to achieve impedance matching and obtain the highest absorption. It is found that, when the sheet resistivity of the NiCr film is ~50 $\Omega/\square$, the impedance matching is obtained. Fig. 3-5 plots the transmission, reflection and absorption spectra of 50nm NiCr film, measured using FTIR, showing that the absorption in 1~4THz is around 20%.

Finally, Au are deposited as the top electrodes for driving and detecting piezoelectric capacitors, and also as electrical connections to apply DC voltage on the NiCr layer, to generate an assigned heat, instead of THz radiation. The thickness of the Au layer is around 100 nm, above a 5 nm adhesion layer of NiCr.

To remove the surplus metal, we use acetone to dissolve the resists and lift off the metal. Ultrasonic cleaner is also used to clean the sample chip.

3.2.4　Sacrificial layer

After finishing the metal deposition, we etch the sacrificial layer and make the MEMS beam suspended. As shown in Fig. 3-6(a) and (b), we first use H_3PO_4-H_2O_2-H_2O solution to etch through the beam layer and expose the sacrificial layer. Then, we use a diluted HF solution to selectively etch the sacrificial layer.

H_3PO_4-H_2O_2-H_2O solution used in this process has a ratio of 1:1:15, which provides a higher speed of 7 nm/s, since the etching thickness is around 2 μm. During this process, the beam geometry is determined. Since the etching takes place not only in the vertical direction but also in the lateral direction of the wafer, the etched geometry is larger than designed pattern, with a tilted edge, as shown in Fig. 3-6(c).

Then, we use diluted HF acid (20%) to selectively etch the sacrificial layer. The composition of the sacrificial layer is $Al_xGa_{1-x}As$ with $x = 0.7$. HF reacts with AlAs, as investigated in Ref. [61,62], the etching rate has a large selectivity $(> 10^6)$ for AlGaAs over GaAs, which enables us to selectively etch the sacrificial layer. The etching rate of $Al_xGa_{1-x}As$ depends on the ratio x and the temperature. In our case, the etchant is kept in a 23°C water bath and the etching rate is around 10 μm/min.

The concentration of HF solution also affects the result. It was shown that 5% HF in the process results in a formation of residues of $AlF_2(H_2O)_{3(s)}$ as insoluble product of the reaction.[61,63]
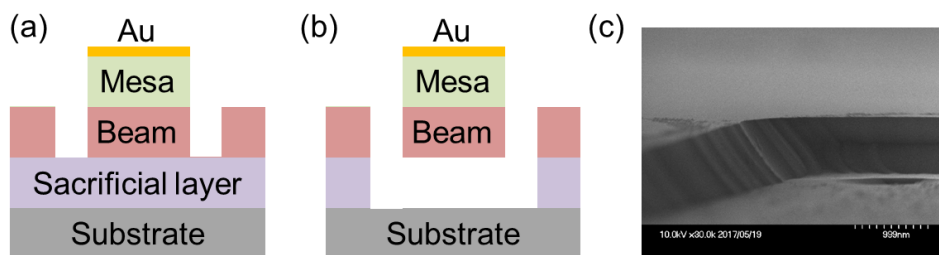
Fig. 3-6 (a) Expose and (b) remove the sacrificial layer. (c) Tilled beam edge.

3.2.5   Drying process

After sacrificial layer etching, the MEMS beam is suspended in the water, and the final process is to dry it up.

Typically, we apply a heat using an incandescent light bulb to dry the samples. When reaching the critical temperature, the liquid changes into gas at a finite rate, and the amount of liquid decreases. Since under the MEMS beam there is only a small gap between the bottom of the beam and the substrate, surface tension in the liquid pulls the beam structure and tends to break the beam. To avoid this, we first put the sample in isopropyl alcohol (IPA), which has a smaller surface tension, and then do the drying. By using this method, MEMS beams up to 200 μm can be fabricated, as shown in Fig. 3-7(a). (100 μm safely and 200 μm risky) But for longer beams, we need to use the supercritical drying.

The supercritical drying is a method to dry samples from the liquid phase to the gas phase without crossing the liquid–gas boundary on the phase diagram, as shown in Fig. 3-7(b).[64] In this process we use low-toxic fluorocarbon liquid (HFE) as the supercritical liquid, and operate the drying process at 2.6 MPa, 473K. The use of a supercritical drying machine (model: PCO-4SC) was kindly offered by Prof. Nakano and Dr. Watanabe.
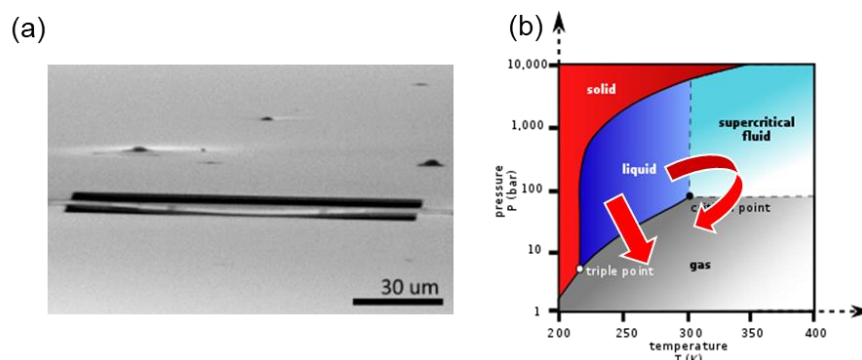
Fig. 3-7 (a) Damaged MEMS beam due to surface tension. (b) Principle of supercritical drying.

3.3   Measurement setup

In the measurement, we want to measure the resonance frequency of the MEMS resonator, in order to evaluate its thermal responsivity. By using the piezoelectric effect, our sample can be driven and detected electrically.[65] Fig. 3-8 shows the measurement circuit of the electrical measurement.

On the driving side, we use a function generator to apply a sinusoidal voltage at a fixed frequency f_0. This signal is also sent to a lock-in amplifier (model: Ametek 7280) as a reference signal. On the detection side, we use a lock-in amplifier to detect the output signal.

To apply a quantitative heat and characterize the thermal response of the samples, we generate heat by apply a DC voltage to the NiCr film at the beam center. Mention that this DC voltage along the beam direction also generate a strain in the beam due to the piezoelectric effect, although very small, we may use a $\pm V$ shape square wave to reduce the influence.

The samples are kept in vacuum ($\sim 10^{-4}$ torr) and room temperature during the measurement.
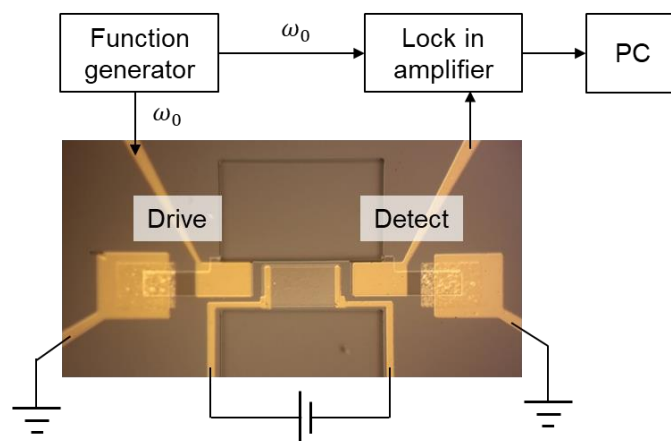
Fig. 3-8 Measurement circuit.

3.4　　Thermal responsivity of GaAs MEMS resonators

We fabricated GaAs MEMS beam samples with dimension of L100×W30×H1.2 μm^3 and measured its resonance spectrum and thermal response. Red curve in Fig. 3-9 shows a resonance spectrum of the MEMS beam resonator. On the driving side we sweep the driving frequency and detect the output signal as the amplitude of beam vibration. In the resonance spectrum we can find the resonance frequency at the peak is 579 kHz. The quality factor, Q, is defined as the ratio of the energy stored in the oscillating resonator to the energy dissipated per cycle by damping processes, which is expressed by the frequency-to-bandwidth ratio:

$$Q = 2\pi \times \frac{\text{energy stored}}{\text{energy dissipated per cycle}} \tag{3-1}$$

For this sample, $Q = 7500$.

Black curves in Fig. 3-9 shows the resonance frequency shift when we apply a heat to the MEMS beam, and if we plot the relationship between the resonance frequency and the heating power, we can see it is almost linear for the THz power range studied here. Consider that the power of THz source is usually smaller than several mW, the thermal responsivity of the MEMS beam resonator can be calculated as the slope of this linear frequency dependence. For this sample, as shown in Fig. 3-10 the responsivity R = 48.2 W^{-1}.

Fig. 3-9 Frequency shift as applying heat to the MEMS beam.
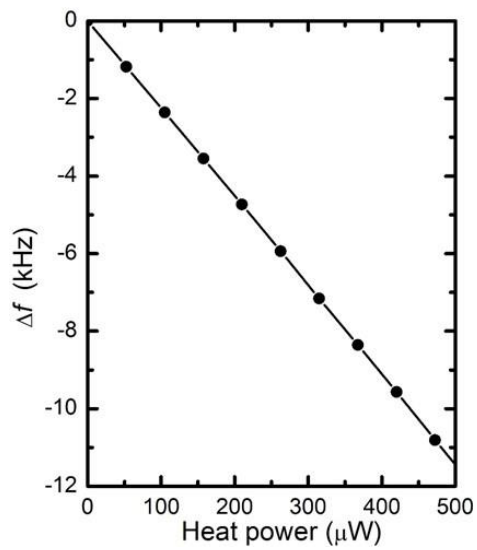
Fig. 3-10 Resonance frequency as function of applied heat power.

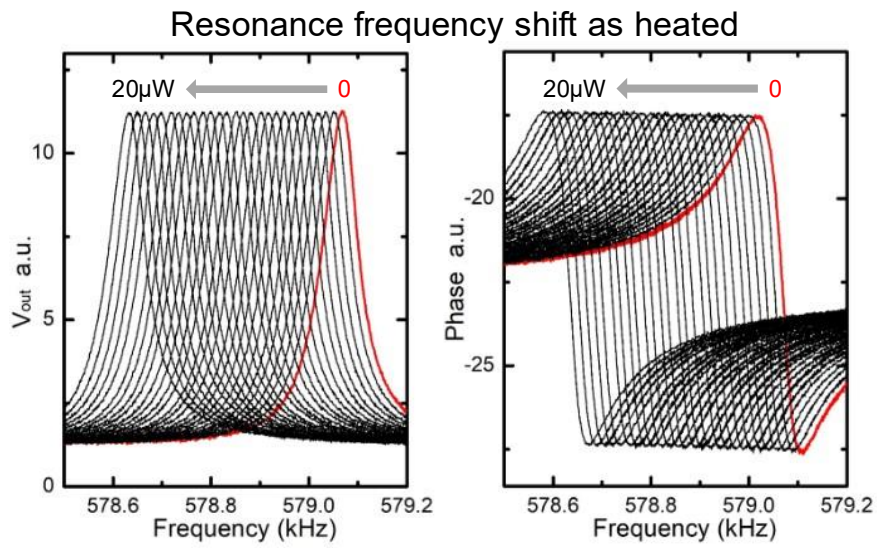We have prepared GaAs MEMS beam resonators with various beam lengths from 80 to 1000 μm. Measured resonance frequency is plotted in Fig. 3-11 together with theoretical calculations by:[57]

$$f_0 = 1.028 \frac{h}{L^2} \sqrt{\frac{E}{\rho}} \tag{3-2}$$

Since the resonance frequency depends only on the beam geometry and mechanical properties of the beam material: the mass density ρ and the Young's modulus E, the experiment results match well with the theory.

To evaluate the thermal responsivity, we generated a quantitative joule heat by apply a DC voltage to the NiCr film. With a heating power P (suppose that all the heat is absorbed by the MEMS beam), the thermal responsivity is derived as:

$$R = \frac{\Delta f}{P} \frac{1}{f_0} = \frac{\gamma_1 \alpha_L}{16\kappa} \frac{1}{w} \left[1 - \left(\frac{l_1}{L} \right)^2 \right] \left(\frac{L}{h} \right)^3 = \frac{9}{64\pi^2} \frac{\alpha_L}{\kappa} \frac{1}{w} \left(\frac{L}{h} \right)^3 \tag{3-3}$$

where length of the NiCr heater l_1 is designed as $0.5L$. The thermal responsivity depends on the beam geometry and thermal properties: the coefficient of thermal expansion α_L and the thermal conductivity κ.

The thermal responsivity of the MEMS beam resonator is expected to be proportional to cubic of the beam length. Responsivity as a function of the beam length is plotted in the Fig. 3-12 together with the experimental results. Theory shows that long beams should have very high responsivity, but in experiment R decreases with increasing L for 250 μm $< L <$ 400 μm and, then, the polarity of R is changed for even longer beams.
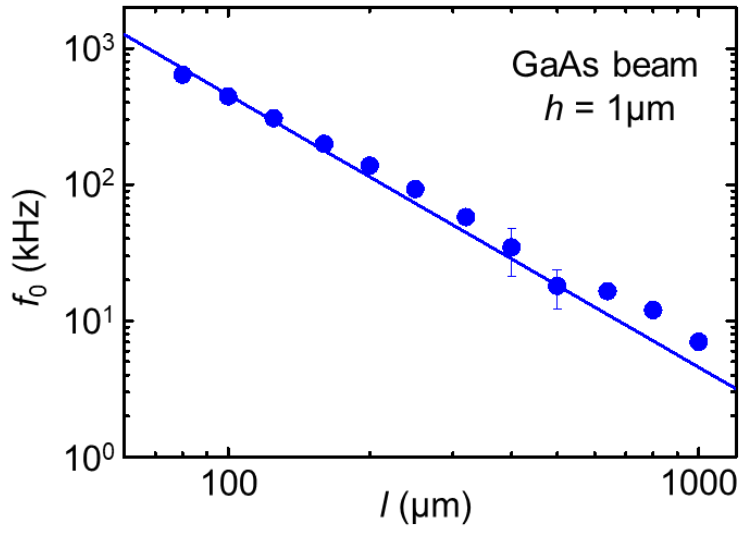
Fig. 3-11 Resonance frequency as a function of beam length.
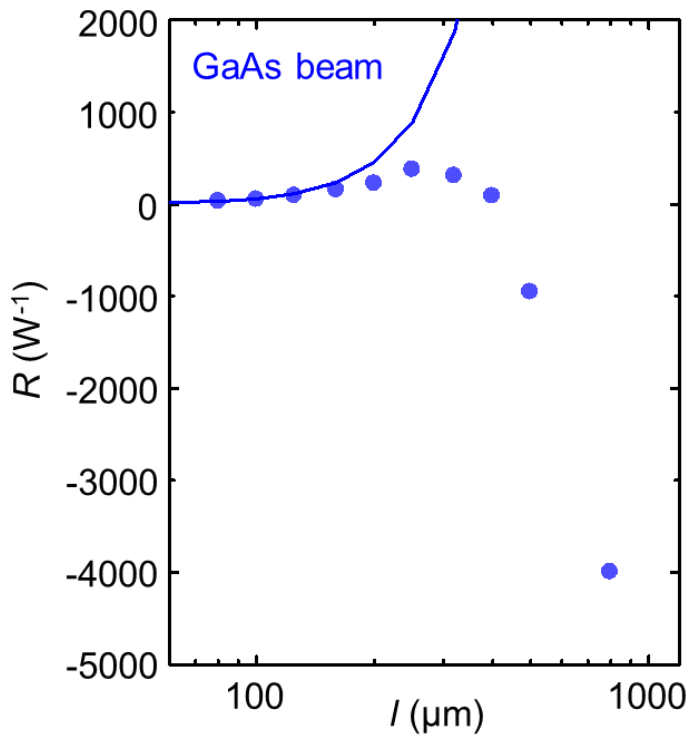
Fig. 3-12 Responsivity as a function of beam length.

Fig. 3-13 shows the resonance frequencies of the GaAs samples as a function of the heating power P. As P increases, the resonance frequency first decreases with P, but for $L > 320$ μm, the resonance frequency starts increasing with P. This is different from the theory in Chap2, for an ideal doubly clamped beam.

For unstrained GaAs samples in Fig. 3-13, when L increase from 100 μm to 200 μm, the critical input heating power is reduced from 5.9 mW to 1.4 mW, proportional to $1/L^2$ as expected by Eq. 3-2. But for longer beams, the critical input heating power reduction is not as expected. Let us look at f/f_0 at the critical point. When $L = 80$ μm, f decreases down to $0.73 f_0$ and, for longer beams, the resonance frequencies at the critical point increases with the beam length, which is again different with the theory mentioned in Chap2: the resonance frequency would decrease to zero at the critical buckling point. This result shows that our MEMS beam is different from an ideal doubly clamped beam, and in the next we consider that the MEMS beam is not ideally flat and has an initial deflection.
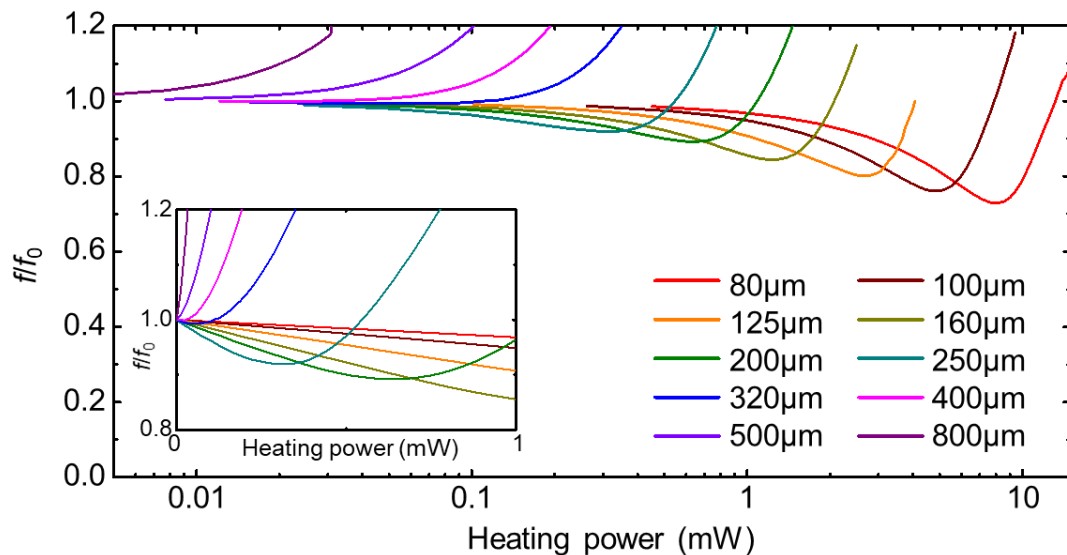
Fig. 3-13 Resonance frequency as function of large heat power of MEMS beams. The frequency is normalized by the resonance frequency of the first bending mode of the MEMS beam without heating. The inset shows the same plot on a linear scale.

3.5   Influence of beam deflection

In Chap2 we mentioned that, for an ideal flat beam the resonance frequency should decrease to zero at the critical buckling strain. However, in practice most of the thin beams are not ideally flat. Here presents a model for the static behavior and for the natural frequencies of the beams with a small initial deflection, subject to an axial end displacement of the clamped ends.[57] Fig. 3-14 shows a schematic representation of the deflected shapes with and without the axial displacement u, respectively.

Approximation: the shape of a deflected beam with $\psi(x) = (1 - \cos(2\pi/L))/2$ the relationship between the axial displacement u, center deflection y and axial compressive strain ε becomes:

$$
\begin{cases}
\dfrac{u}{L} = \varepsilon + \left(\dfrac{\pi z}{2L}\right)^2 - \left(\dfrac{\pi y}{2L}\right)^2 \\[3mm]
y = \dfrac{z}{1 + \varepsilon/\varepsilon_{cr}} \text{ with } \varepsilon_{cr} = \dfrac{\pi^2 h^2}{3L^2}
\end{cases}
\tag{3-4}
$$

Fig. 3-15 plots the relationship between the normalized axial load $N/\hat{E}A\varepsilon_{cr}$ and the normalized center displacement $\sqrt{3}y/2h$ as a function of the normalized axial strain $\varepsilon/\varepsilon_{cr}$, for various values of the normalized initial deflection $Z = z/h$. For a flat MEMS beam ($Z = 0$), at first the strain is proportional to the axial load N. For values of N beyond the critical buckling value $\hat{E}A\varepsilon_{cr}$, however, the center displacement is no more zero, which means the flat beam is buckled. The exceeding force is relaxed by an increase of the center displacement, and the axial strain does not change with the axial load increase.[57] While for MEMS beams with a deflection, as plotted with dashed lines, the deflection is enhanced by an axial compression, and the center displacement gradually increase when $N < \hat{E}A\varepsilon_{cr}$.

A buckled beam has a longer effective length, which will change the resonance frequency of the MEMS resonator.
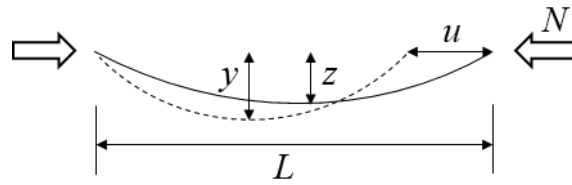
Fig. 3-14 Shape and center deflection *z* and *y* of deflected beam with and without axial load *N*.
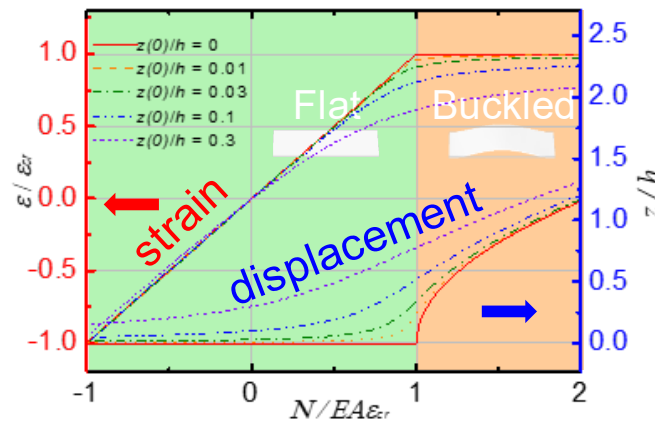

Fig. 3-15 Normalized axial strain and beam deflection as a function of normalized axial load, for different values of normalized initial deflection.
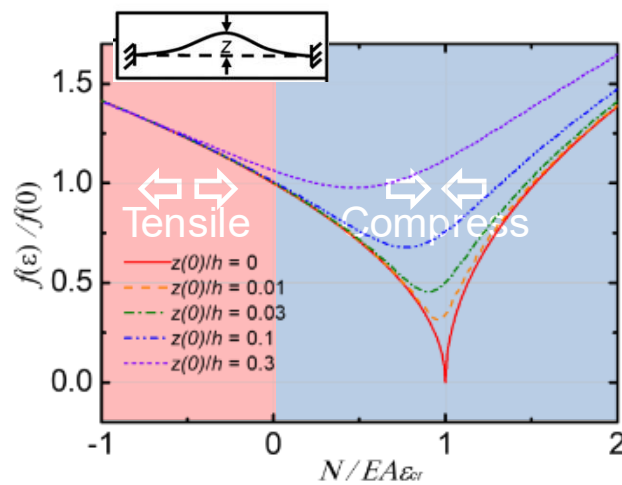

Fig. 3-16 Normalized fundamental frequencies as a function of normalized axial load, for different values of normalized initial deflection.

When a deflected beam vibrates, the axial strain due to dynamic stretching of the beam is given by:[57]

$$\varepsilon(t) = \frac{1}{2L} \int_0^L \left(y \frac{\partial \psi(x)}{\partial x} + \frac{\partial Y(x,t)}{\partial x} \right)^2 - \left(y \frac{\partial \psi(x)}{\partial x} \right)^2 dx \qquad (3\text{-}5)$$

The equation of motion of a buckled beam becomes:

$$\rho A \frac{\partial^2 Y(x,t)}{\partial t^2} + \hat{E} I_z \frac{\partial^4 Y(x,t)}{\partial x^4}$$
$$= N \frac{\partial^2 Y(x,t)}{\partial x^2} + \frac{\hat{E} A}{L} \int_0^L \left(y \frac{\partial \psi(x)}{\partial x} \cdot \frac{\partial Y(x,t)}{\partial x} \right) dx \cdot y \frac{\partial^2 \psi(x)}{\partial x^2} \qquad (3\text{-}6)$$

To solve Eq. 3-6, Ref. [57] uses the Galerkin method, approximating the solution *S(x)* with a series of the exact mode shapes of initially flat doubly clamped beams under zero axial stress. Fig. 3-16 gives a graphical representation of the normalized fundamental frequency as a function of normalized axial load for various values of the initial deflection. With a small strain $-1 < N/\hat{E}A\varepsilon_{cr} < 1.3$ the curves are well approximated by:

$$f_1(\varepsilon) = f_1(0) \sqrt{1 + \gamma_1 \frac{L^2}{h^2} \varepsilon + 1.5 \cdot \frac{y^2}{h^2}} . \qquad (3\text{-}7)$$

In Fig. 3-16 the resonance frequency of the resonator decreases with the axial load increase and starts increase at a critical point. However, different from the flat beam, resonance frequency of the beams with initial deflection does not decrease to zero at the critical point; the resonance frequency becomes higher when the deflection is larger and the slope of frequency decrease becomes smaller, indicating a lower thermal responsivity. Around the critical buckling strain, flat beam shows a sharp dip, which is suitable for a high thermal responsivity of MEMS bolometer. However, with a larger deflection, the sharp dip gradually disappears.

From the comparison between theory and experiment (Fig. 3-13 and Fig. 3-16), the magnitude of the initial deflection of the MEMS beams can be estimated from the resonance frequency at the critical buckling point, f_c. For the case of $L = 100$ μm GaAs sample, $f_c = 0.76 f_0$, which corresponds to an initial beam deflection $z_0 \sim 150$ nm at the beam center. For longer beams, f_c/f_0 gradually increases, indicating that the initial deflection becomes larger for longer beams. The MEMS beams with $L > 400$ μm is buckled from the beginning and f increases when the beam is heated. This corresponds to the situation when $z_0/h > 0.6$ in Fig. 3-16.

3.6　Use GaAsP to introduce tensile strain

From the theory of beam deflection, we know that our MEMS beam is not ideally flat and long beams shows larger beam deflections, which may result in a lower responsivity. For long and thin beams, a small compression will easily make the beam bent and reduce the beam deflection. Such small compression is always introduced to the MEMS beam by lattice mismatch between GaAs and AlGaAs, and also the plastic deformation during the fabrication process such as the drying process.[66]

To solve this problem, we propose to introduce a preloaded tensile strain to stretch the MEMS beam. Therefore, we can avoid the residual compressive strain, suppress the beam deflection and increase the responsivity for long beams.

There are some works about introducing tensile strain to GaAs MEMS resonators by using a lattice mismatch.[67–70] Onomitsu *et al*. added a small amount of nitrogen in the beam structure.[68] Because GaN has a smaller lattice constant than GaAs, there is a preloaded tensile strain in the MEMS beam when nitrogen is introduced in the beam layer. They achieved an enhancement in resonance frequency, from 140 kHz to more than 700 kHz, and also increased quality factor by 30 times (Fig. 3-17).

However, as shown in Fig. 3-18, since nitrogen acts as deep levels in GaAs, GaNAs will trap the electrons from the conduction band, and make the n-type GaAs layer insulating. Therefore, it is very difficult to create a conductive layer in the MEMS beam and form piezoelectric capacitors. In their work they used an optical detection scheme.
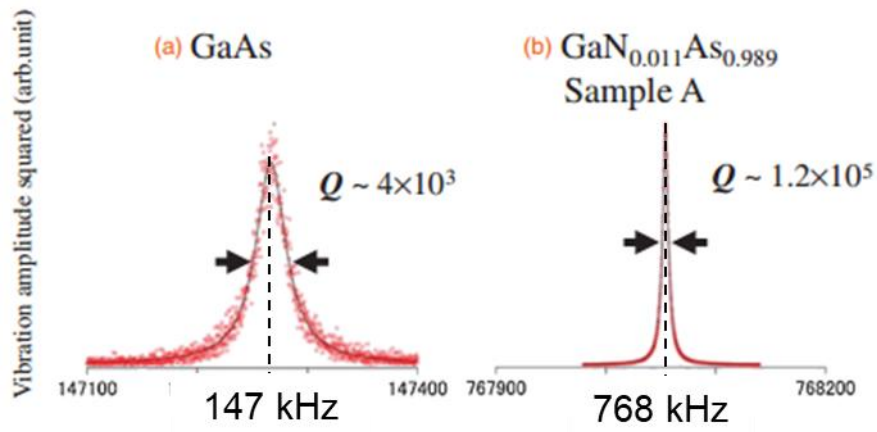
Fig. 3-17 Use GaNAs to induce tensile strain in the MEMS beam.[68]
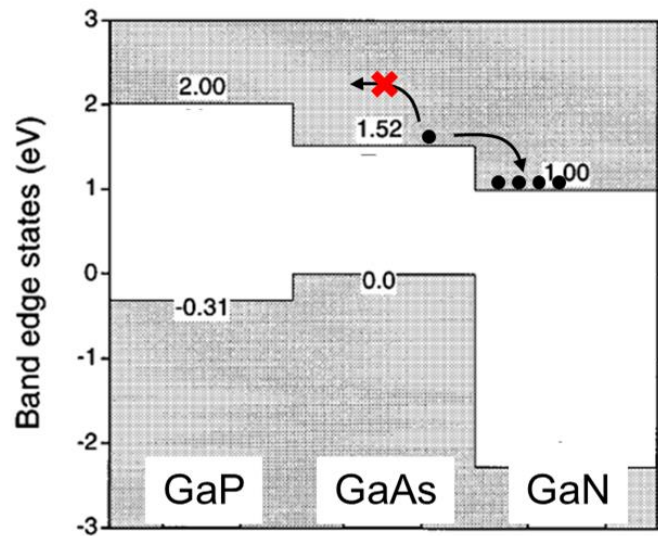
Fig. 3-18 Band-gap energy of GaP, GaAs and GaN.[71]

In this work, we have introduced phosphorus, instead of nitrogen, to introduce a tensile strain to the MEMS beam. As shown in Fig. 3-19, since GaP has a smaller lattice constant than GaAs and also has a larger bandgap, it will not trap carriers from the conduction band. Therefore, we can achieve a conductive layer and a tensile strain at the same time.

Fig. 3-20 shows the wafer structure. We add a small amount of phosphorus to the GaAs MEMS beam. As the ratio of phosphorus x to be 0.01, the induced tensile strain is estimated by

$$\varepsilon = \frac{(a_{\text{GaAs}} - a_{\text{GaP}}) \cdot x}{a_{\text{GaAs}}} = 0.035\% \qquad (3\text{-}8)$$

where a_{GaAs} and a_{GaP} is the lattice constant of GaAs and GaP, respectively.
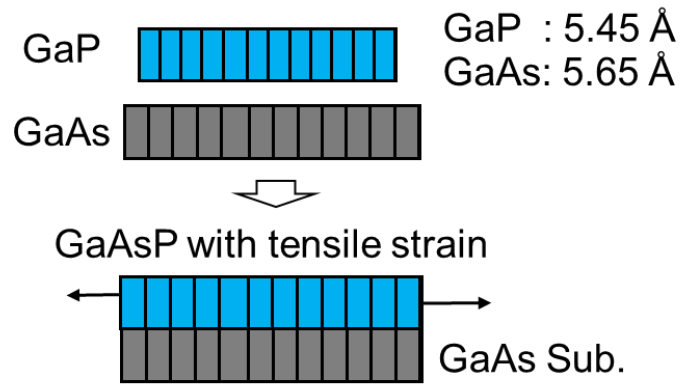
Fig. 3-19 Use GaAsP to induce tensile strain in the MEMS beam.
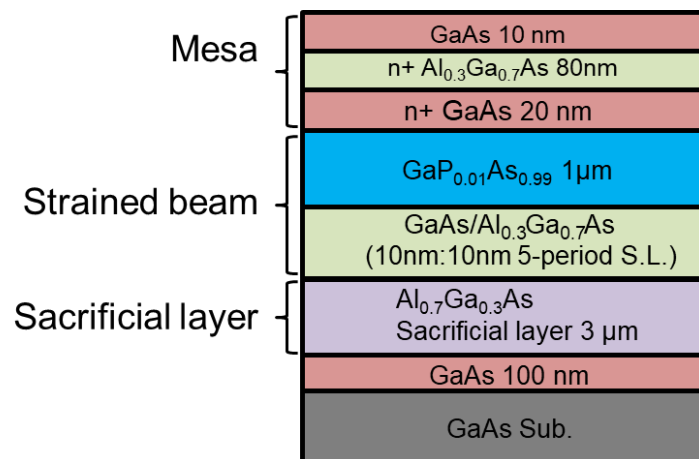
Fig. 3-20 Wafer structure of GaAsP sample.

3.7   Thermal responsivity of GaAsP MEMS resonators

We have prepared samples with a standard doubly clamped MEMS beam resonator by using GaAs or strained $GaAs_{1-x}P_x$ ($x = 0.01$ and 0.06) on the GaAs substrates. Samples with various beam lengths from 80 to 1,000 μm were fabricated for the GaAs and GaAsP structures. Fig. 3-21 shows an SEM image of the fabricated 200 μm GaAsP sample. Measured resonance frequencies of the samples of various beam lengths plotted in Fig. 3-22 agree with theoretical expectation by Eq. 2-18, indicating that by using GaAsP, we have successfully applied a tensile strain in the MEMS beam. Mention that compared with GaAs samples, GaAsP samples with same length shows a higher resonance frequency f_0.

Next, we applied a heat to the MEMS beams and measured their thermal response. Fig. 3-23 shows the resonance frequencies of the $GaAs_{1-x}P_x$ ($x = 0.01$) samples as a function of the heating power, P. When $L = 100$ μm, the resonance frequency at the critical buckling point f_c reaches $0.55f_0$, suggesting that the initial beam deflection z_0 is reduced to ~50 nm, which is approximately 1/3 of that for the GaAs sample of the same length. For longer L, f_c/f_0 decreases with increasing L, suggesting that the beam deflection is almost constant to be ~50 nm and does not increase with increasing L.

Fig. 3-24 shows the measured R as a function of L for the $GaAs_{1-x}P_x$ samples with $x = 0.01$ and 0.06, together with R for the GaAs samples (replotted from Fig. 3-12). As seen in the figure, R for the $GaAs_{1-x}P_x$ samples keeps increasing with L. This result indicates that, by preloading a small amount of tensile strain to the MEMS beam, we can efficiently suppress the beam deflection and avoid unpredictable behavior in R. Fig. 3-25 plots the normalized resonance frequency (red) and its derivative (blue) as function of the normalized axial compressive load, $N/EA\varepsilon_{cr}$, calculated for an ideally flat MEMS beam. In the case of $GaAs_{1-x}P_x$ MEMS beams, N consists of the lattice mismatch, $EA\varepsilon_l$, and the thermal expansion, $EA\varepsilon_{th}$. The blue curve plots df/dN, which is proportional to R of the MEMS bolometers ($R \propto df/d\varepsilon_{th}$). df/dN decreases with increasing tensile strain, meaning that R decreases with increasing phosphorus

concentration. Indeed, as seen in Fig. 3-24, R for $x = 0.06$ is smaller than that for $x = 0.01$. Therefore, preloading a tensile strain to the MEMS beam is, in general, not favorable to achieving high responsivities. However, we want to emphasize here that, by preloading a small amount of tensile strain to the MEMS beam, we can avoid unpredictable behavior in R due to the beam deflection and achieve high thermal responsivities as designed for long MEMS beams.

Briefly to conclude, we find that for unstrained, long GaAs MEMS beams, the thermal responsivity deviates from theoretical expectations and even decreases with L due to large initial beam deflection. To reduce the beam deflection, we have introduced a preloaded tensile strain in the MEMS beam by using lattice mismatch between $GaAs_{1-x}P_x$ ($x = 0.01$) and GaAs. We find that the deflection of $GaAs_{1-x}P_x$ MEMS beam is efficiently suppressed and the responsivities increase for increasing beam length, demonstrating that the introduction of tensile strain is useful for achieving high thermal responsivities predicted for long MEMS beams.
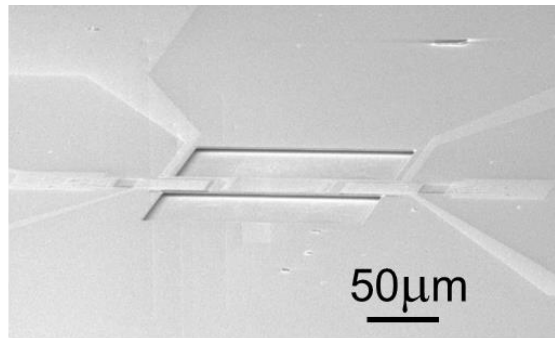
Dimension: $200L \times 30W \times 1.1H\ \mu m^3$

Fig. 3-21 SEM image of fabricated sample.
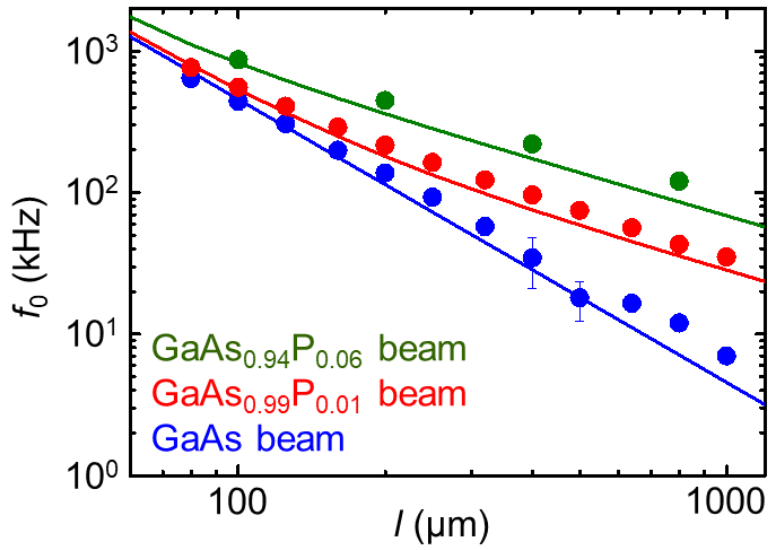
Fig. 3-22 Resonance frequency of the GaAs and GaAs$_{1-x}$P$_x$ MEMS samples as a function of the beam length. Dots: experimental results; line: theory.
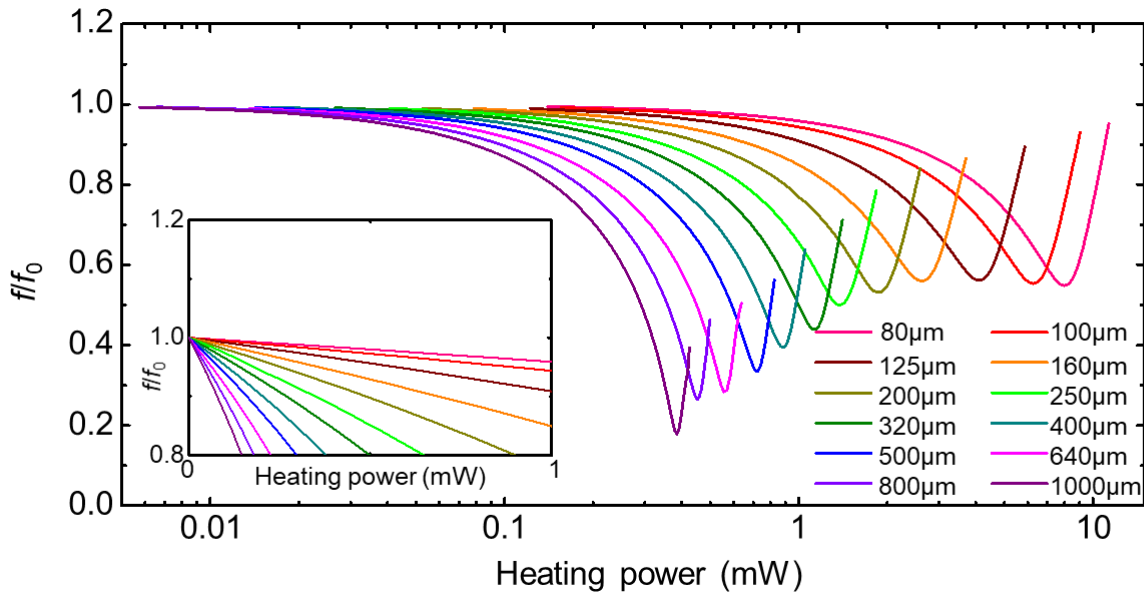
Fig. 3-23 Resonance frequency as function of large heat power of GaAs$_{1-x}$P$_x$ (x = 0.01) MEMS beams. The inset shows the same plot on a linear scale.
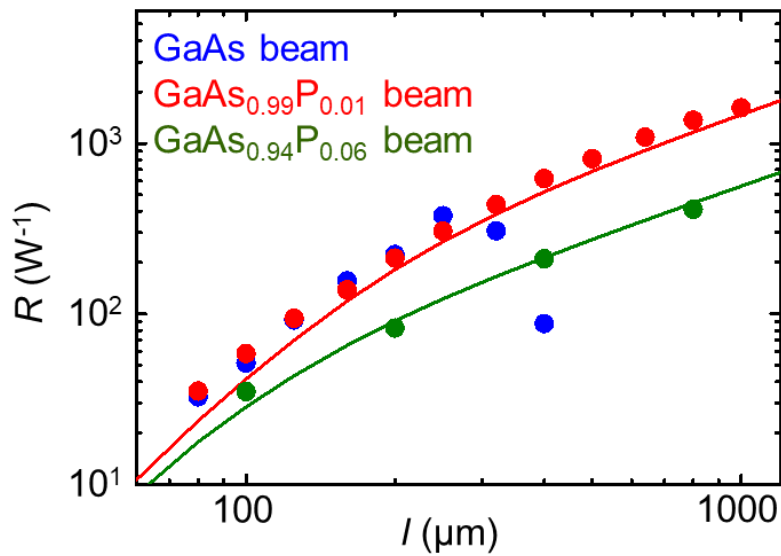
Fig. 3-24 Responsivity of the GaAs and GaAs$_{1-x}$P$_x$ MEMS samples as a function of the beam length. Dots: experimental results; line: theory.

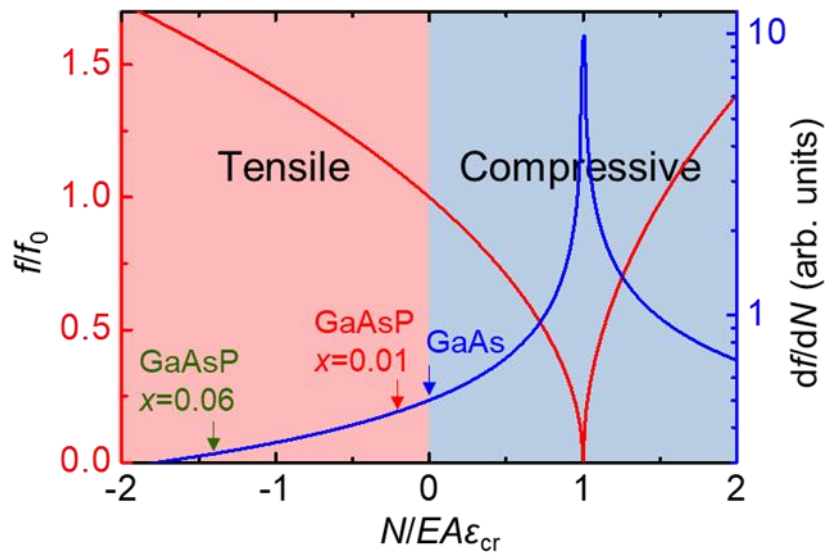Fig. 3-25 Normalized resonance frequency (red) and its derivative (blue) as a function of the normalized axial compressive load, $N/EA\varepsilon_{cr}$, calculated for an ideally flat MEMS beam. Arrows denote $N/EA\varepsilon_{cr}$ for the tensile-strained GaAs$_{1-x}$P$_x$ beam layers.

3.8　　Effect of surface step structures on the beam deflection

By introducing a tensile strain to the MEMS beam, we have successfully reduced the beam deflection for long MEMS beams. However, for short beam, there still exists a residual deflection. For 80 μm GaAsP MEMS beam, $f_c/f_0 = 0.55$, suggesting that there is a deflection of 50 nm. The reason for this residual deflection is still unknown.

To clarify the reason of this residual deflection, we first think the deflection is induced by residual strain in the 100nm-Au layer.[72] GaAs and Au shares similar stiffness, whose Young's modulus are $E_{[100]\,GaAs} = 85.9\text{GPa}$ and $E_{Au} = 79\text{GPa}$, both of which are much softer than Si with $E_{[100]\,Si} = 130\text{GPa}$. We fabricated samples using a 17nm-NiCr layer instead of the 1000nm-Au layer as the top electrode of the piezo capacitors. With the metal layer become thinner, the residual strain should become much smaller. We applied Joule heat to the sample and measured the resonance frequency shift, the result is plotted as red curve in Fig. 3-26. For sample A with an Au electrode, $f_c/f_0 = 0.86$ and $z_0 = 0.23t = 273\text{nm}$ and for sample B with thin NiCr electrode, f_c, slightly reduces to $0.83f_0$, indicating an initial deflection of 237nm. By using a thin NiCr film as the electrode, the deflection is not reduced as expected, suggesting that there is some other reasons for the deflection.

Then we consider that the residual deflection is induced by the step structure on the MEMS beam surface. We fabricated samples with different step height, h, and measured the thermal response. The step height is changed by controlling the mesa etching depth, where the etching depth various from 0 to 183nm. Fig. 3-27 shows the profiles of the sample surface. Table 3.1 list the etching depth and electrode material of different samples. We applied heat to the MEMS beams and measured their thermal response. Fig. 3-28 shows the resonance frequencies of the MEMS beams as a function of the heating power. As shown in Fig. 3-28, with increasing h, the minimum resonance frequency increase, dots in Fig. 3-29 plots f_c/f_0 as a function of h.
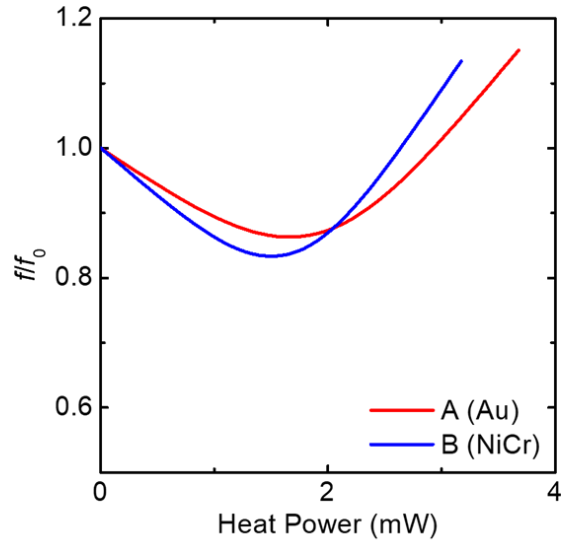
Fig. 3-26 Resonance frequency as function of large heat power of MEMS beams with different electrodes.
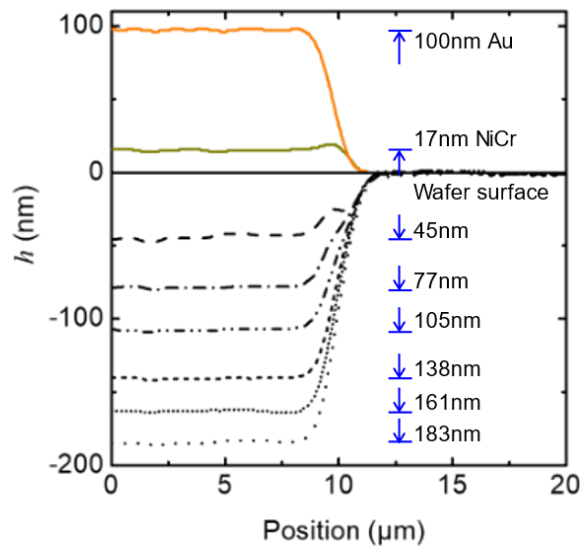
Fig. 3-27 Profile of the mesa etching depth and the electrodes.

Table 3.1 List of samples with different surface structure.

Sample #	Etching depth (nm)	Electrode material	Step height h (nm)
A	183	100nm Au	283
B	183	17nm NiCr	200
C	161		178
D	138		155
E	105		122
F	77		94
G	45		62
H	0		17
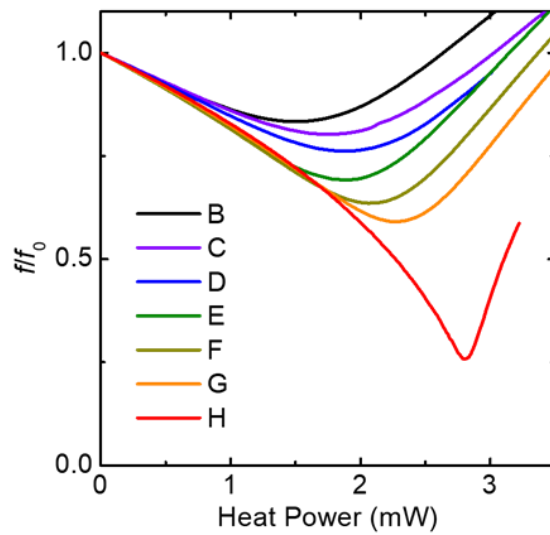
Fig. 3-28 Resonance frequency as function of large heat power of MEMS beams with different surface structure.
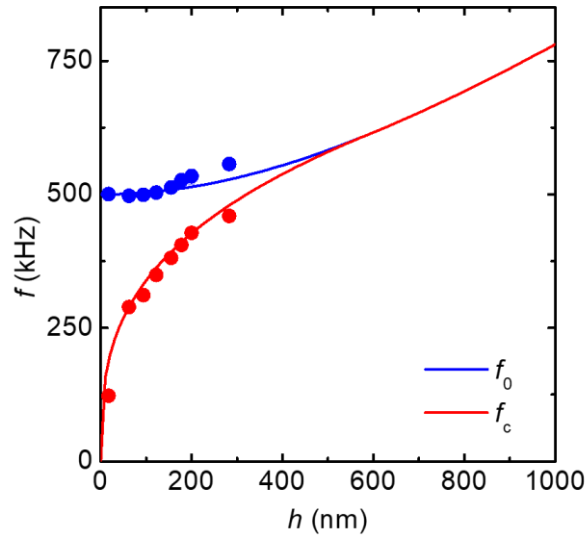
Fig. 3-29 Resonance frequency without heating as function of the step height. Dots: experimental results; line: theory.

We can estimate the magnitude of deflection from the comparison between theory and experiment (Fig. 3-13 and Fig. 3-28). For sample H which has the minimum step height, $f_c/f_0 = 0.24$ and the MEMS beam has a deflection as small as $z_0 = 12$nm. Fig. 3-30 plots the estimated beam deflection of samples B~H, z_0, as a function of h. Relationship between z_0 and h is linear relation, which gives the formula applicable to our case as follows:

$$z_0 = 1.059h - 0.001\text{nm}, \tag{4}$$

of which the coefficient of determination is $r^2 = 0.991$. We can see an almost identical relationship between z_0 and h, and intercept of the fitting line is almost zero, which means the surface step is the dominating reason of the beam deflection. R_0 as function of the h is plotted as dots in Fig. 3-31. As seen in the result, R_0 decreases with increasing h and follows the theoretical calculation. R_0 of sample A is reduced by 35% due to the large beam deflection, demonstrating the importance of reducing the deflection in MEMS resonator device.

Furthermore, an improvement of thermal responsivity, R, can be observed for samples with small deflection. As seen in Fig. 3-28, for samples with small deflection (sample E~H), a steep dip can be observed around the buckling point, where the slope of f-P curve becomes steeper and indicates a larger R. Fig. 3-32 plots R as a function of P. For each sample, R will decrease to zero at its buckling point. Before the buckling point, R of sample A~D decrease monotonically due to the large deflection and decreasing slope in the f-P relationship, while for sample E~H, R increases when the MEMS beam is slightly heated. For sample H, R increases by 6 times at the buckling point, compared with the value of without thermal strain, showing a possibility of increasing the thermal responsivity by preloading compressive strain in the MEMS beam.
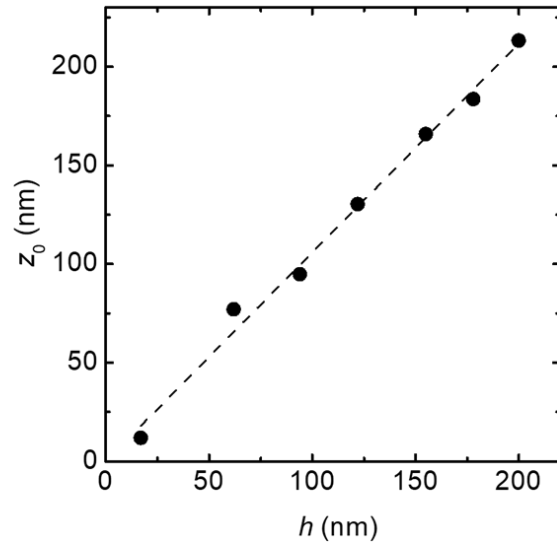
Fig. 3-30 Estimated beam deflection of samples B~H, as a function of the step height.
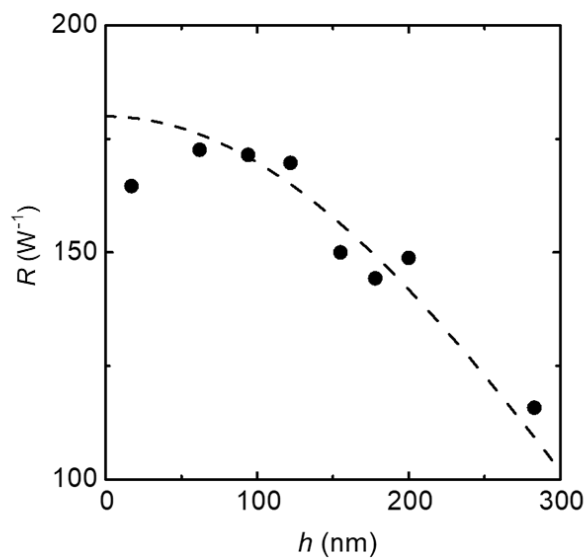
Fig. 3-31 Responsivity of samples B~H, as a function of the step height.
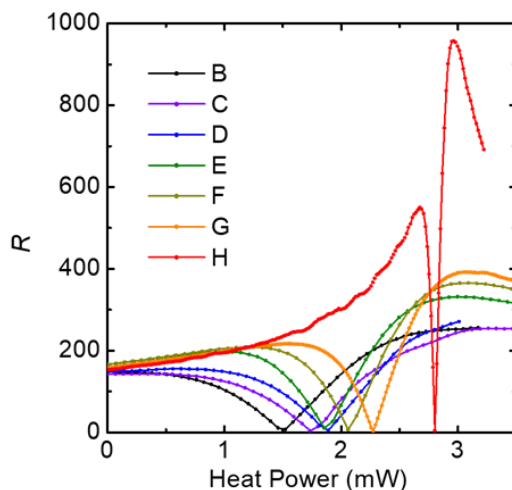
Fig. 3-32 Responsivity change as function of large heat power of MEMS beams with different surface structure.

3.9   Summary

We have found that the deflection in the MEMS beam affects the thermal responsivity of the MEMS bolometers. There are two factors that induce the beam deflection. First is the initial bending of MEMS beam due to a residual compression. This kind of initial bending increases with the MEMS beam length. In order to reduce the initial bending, we have introduced GaAsP to induce a tensile strain in the MEMS beam to suppress the beam deflection. The tensile strain is induced by lattice mismatch between GaAs and $GaAs_{1-x}P_x$ and stretches the MEMS beam to make it flat. We have chosen phosphorus instead of nitrogen as the alloy material because nitrogen atoms trap electrons from the conductive layer that we use to realize electrical driving and detection. We find that the deflection of $GaAs_{1-x}P_x$ MEMS beam is efficiently suppressed and the responsivities increase for increasing beam length, demonstrating that the introduction of tensile strain is useful for achieving high thermal responsivities predicted for long MEMS beams.

On the other hand, for short beams, there are other reasons that causes the beam deflection. Another reason of the beam deflection is step structure on the beam surface. We have investigated the effect of surface step structure of the beam on the thermal responsivity of the MEMS beam resonator structures. We find that, a step structure on two ends of the beam will effectively induce a deflection of the MEMS beam and reduce its thermal responsivity. By reducing the mesa height, we finally suppressed the beam deflection to 10 nm in 80 μm MEMS beam. Furthermore, we calculate the thermal responsivity as the slope of these curves and plot it as function of heating power. For samples which has smaller deflection, we see the responsivity increase when we heat the MEMS beam with large power. This is because the slope of frequency-power curve gets steeper around the buckling point. For sample with beam deflection of 10nm, we observed a sharp dip around its buckling point, and the responsivity becomes 6 times higher than the fundamental point.

In this chapter we clarified the two factors that induce the beam deflection. One is the initial bending of MEMS beam and the other is the surface step structures. This knowledge will help with designing of beam structures and predicting the device performance in the following research.

Chapter 4

Introduce compressive strain to the MEMS beam

4.1   Introduction

We proposed to utilize a GaAs MEMS beam resonator to detect THz radiation at room temperature. When the MEMS beam is illuminated with THz radiation, the beam is heated. Due to the thermal expansion of the beam and the rigid boundaries set by the substrate, a compression is generated along the beam and changes the resonance frequency. Our device uses the piezoelectric effect to detect this resonance frequency shift and works as a very sensitive THz bolometer. Speed of the device can be up to 10kHz, which is much faster than other kinds of room-temperature THz thermal sensors.

In order to improve the sensitivity of the MEMS detector, a larger value of frequency shift by absorbed THz heat is preferred. Fig. 4-1 shows the heat flow in the MEMS beam. When the center part of the beam is heated by THz radiation, the heat flows to the substrate. For a short MEMS beam, it is easier for heat to escape, and there is a small temperature rise. Therefore the responsivity of short beams is low. On the other hand, the system can quickly achieve thermal equilibrium, therefore, the response time of the short beams is short which means a high operation speed. In contrast, a long MEMS beam keeps the heat for a long time and has a higher temperature rise. Therefore, the longer MEMS beam shows higher responsivity, but lower speed.

High responsivity and high speed cannot be achieved at the same time by simply changing the beam dimensions. We also tried other methods to increase the temperature rise, such as adopting phononic crystals to reduce thermal conductivity of the beam. However, all these methods have a trade-off between the speed and the responsivity. Another method is to increase the thermal strain induced by the temperature rise. However, it is very difficult to modulate the thermal expansion coefficient. Finally we look into the relationship between resonance frequency and internal strain. In last chapter we see the possibility of increasing the devices' thermal responsivity by introducing a compressive strain to the MEMS beam. Introducing a strain does not change the thermal conductivity of MEMS beams and should be a promising method for realizing high responsivity and high speed at the same time.
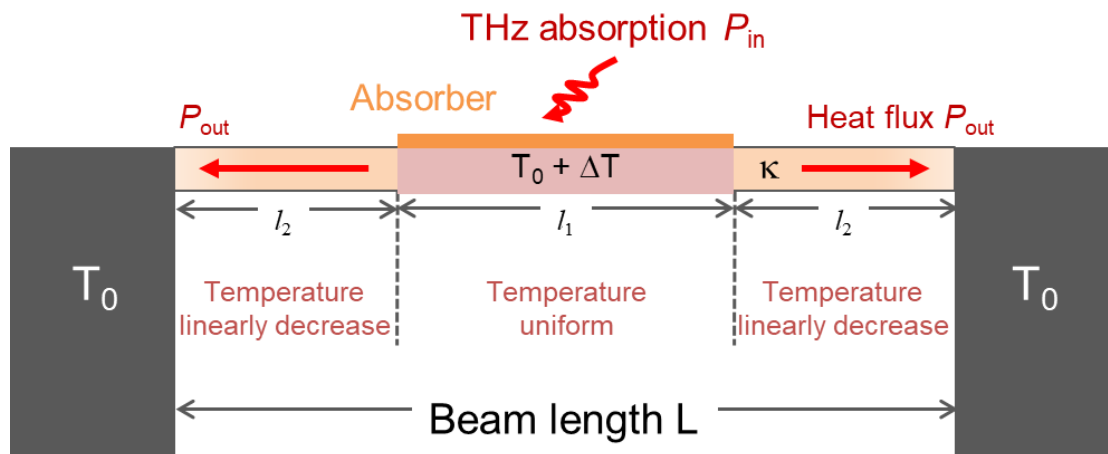
Fig. 4-1 Schematic of heat flow in the MEMS beam

4.2　　Introduce compressive strain to MEMS beam

Red curve in Fig. 4-2 plots the relationship between the resonance frequency and the compression applied to the MEMS beam. when a compressive strain is applied, the curve becomes steeper as the buckling point is approached. Around buckling point of the MEMS beam, there is a sharp dip in the resonance frequency. This shows the device shows a larger frequency shift around the buckling point. This effect can benefit the MEMS bolometer application, because the bolometer measures the frequency change induced by thermal compression and the responsivity of the bolometer is proportional to the slope of the frequency-strain curve. The blue curve in Fig. 4-2 plots the deviation of the frequency-strain curve, which is proportional with the thermal responsivity of the MEMS detector. Around the buckling point we expect a more than 10 times higher responsivity than that of the MEMS beam without any strain.

In order to obtain this high responsivity, we have preloaded a compressive strain in the MEMS beam by adding 0.4 percent of In in the beam layer. Fig. 4-3 shows the wafer structure. Since InAs has a larger lattice constant than GaAs, as seen in Fig. 4-4, a preloaded compressive strain is introduced in the beam layer when we grow InGaAs on a GaAs substrate.
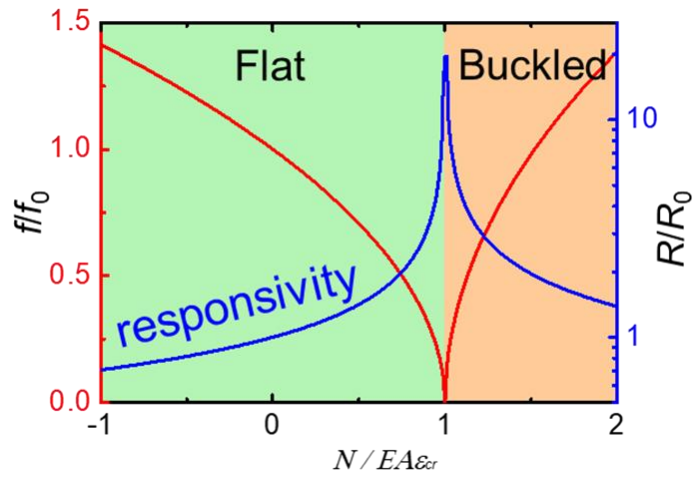
Fig. 4-2 Resonance frequency and thermal responsivity of MEMS resonator as a function of a compression applied to the MEMS beam
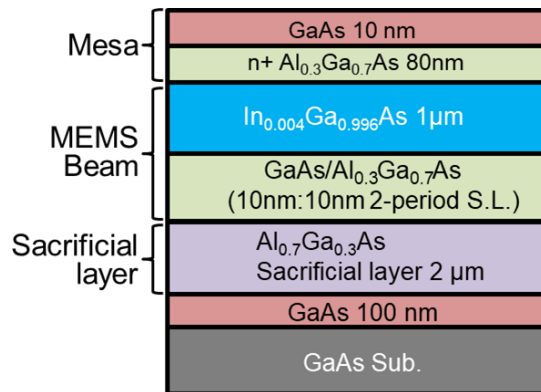
Fig. 4-3 Wafer structure of the InGaAs sample.
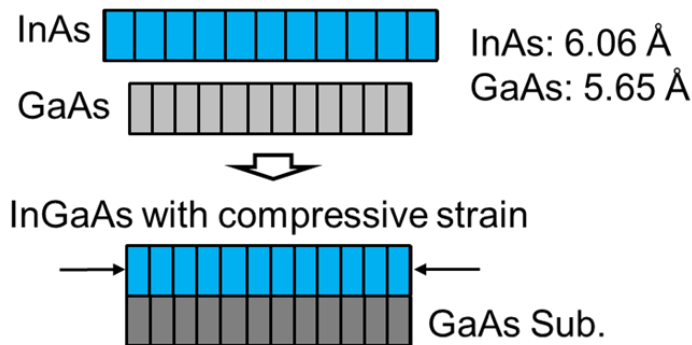
Fig. 4-4 Use InGaAs to preload a compressive strain in the MEMS beam.

Another question is how to set the MEMS beam exactly at the buckling point. In order to have a large responsivity the preloaded lattice strain needs to be equal to the critical buckling strain of the MEMS beam. If there exists even a slight shift from the critical condition, we cannot expect such a dramatic responsivity enhancement. However, it is not realistic to grow many wafers with various In concentrations to choose the best one. Therefore, we took a different approach.

The lattice strain is a function of the In concentration x in the $In_xGa_{1-x}As$ alloy:

$$\varepsilon_l = \left(\frac{a_{InAs}}{a_{GaAs}} - 1 \right) \cdot x. \tag{4.1}$$

On the other hand, the critical buckling strain is a function of the beam length:

$$\varepsilon_{cr} = \frac{\pi^2}{3} \frac{h^2}{L^2} \tag{4.2}$$

Instead of fixing the buckling strain and sweep In concentration x, we can sweep the buckling strain by changing the beam length L. Knowing the In concentration $x = 0.4\%$, it can be calculated that the lattice strain becomes equal to the critical buckling strain when the beam length $L = 104$ μm, and a large enhancement in the responsivity can be expected at this length. For MEMS beam shorter than 104 μm, the lattice strain is smaller than the buckling strain and the beam is flat. When a flat beam is heated, as the blue dot in Fig. 4-5, its resonance frequency first decrease until the buckling point, then start to increase with larger thermal compression. On the other hand, for MEMS beam longer than 104 μm, the lattice strain is larger than the buckling strain, and the MEMS beam is already buckled. In this case, its resonance frequency just increases when applied heat is increased, as plotted in the red dot in Fig. 4-5. This calculation shows that, we can control whether the fabricated MEMS beam is flat or is buckled by changing the MEMS beam length.
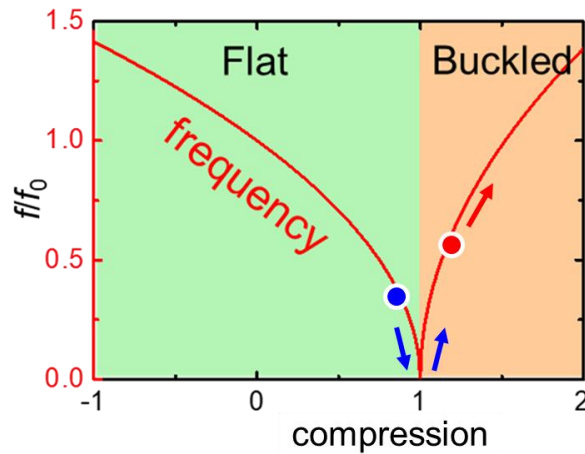
Fig. 4-5 Resonance frequency shift when heat is applied to a initially flat / buckled
MEMS beam

4.3 Under etching in MEMS beam

Although the critical buckling beam length is calculated to be 104 μm when $x =$ 0.4%, the experimental result does not match with the calculation. This can be explained by the under etching effect in the fabrication process of the MEMS beam. When the sacrificial layer is removed by diluted HF, not only just beneath the MEMS beam, but also sacrificial layer in the length direction is etched. This makes the fabricated MEMS beam slightly longer than designed. Fig. 4-6 shows the schematic of the MEMS beam, when the under etching takes place. Fig. 4-7 shows microscope image of the under-etched sample. When the sample is illuminated by a 940nm LED, the part etched by HF can be observed in an infrared camera. We can see the MEMS beam length becomes longer than the designed L.

To see the effect of the under-etching, we fabricated and measured GaAs samples with various beam lengths from 40 μm to 100 μm, Fig. 4-8 shows the measured resonance frequency of the GaAs samples as a function of the designed L. When we add 20 μm to the nominal L, theory in solid lines matches with the experiment result well. Previously when we fabricate MEMS beam length of several hundreds of μm, this effect is not significant. However, now it cannot be ignored when L is less than 100 μm.
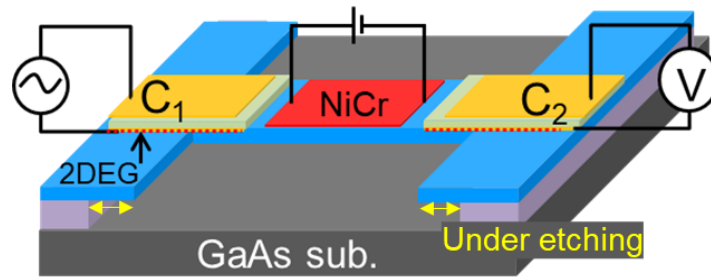
Fig. 4-6 Schematic of the MEMS device. A under etching happens in the sacrificial layer
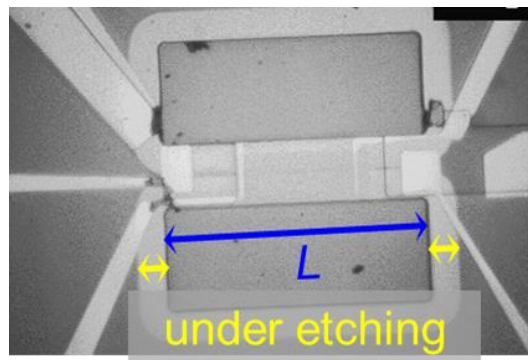
Fig. 4-7 Microscope image of under etching in MEMS beam. This image is kindly provided by Prof. Zhang.
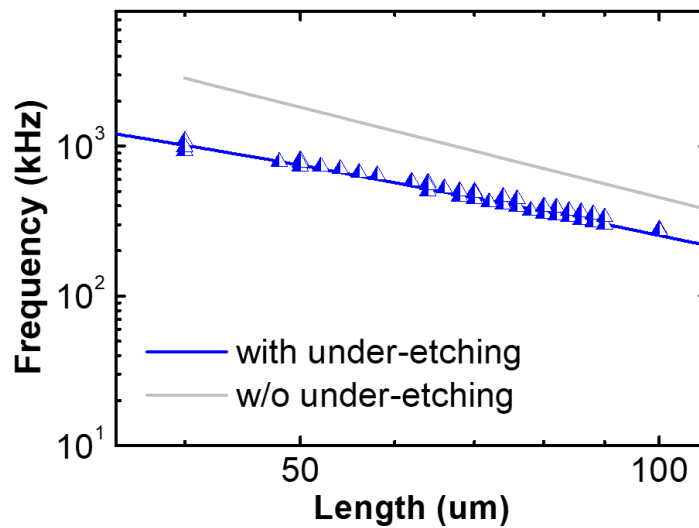
Fig. 4-8 Resonance frequency of GaAs samples as a function of the beam length. Dots: experimental results; line: theory.

4.4   Resonance frequency of InGaAs MEMS beam

We fabricated GaAs and InGaAs beam samples with various lengths from 40 to 100 μm. Fig. 4-9 plots the measured resonance frequency as a function of beam length. For standard GaAs samples shown by blue dots, the resonance frequency gradually decreases. For InGaAs samples shown in red, the resonance frequency first decrease and then increase with increasing L. The minimum resonance frequency occurs at 90 μm, which is identified to be the buckling beam length.

Fig. 4-10 plots color-coded the resonance spectra of the InGaAs samples with beam length L = 86 μm and 94 μm, as a function of heating power. When L = 86 μm, which is shorter than the buckling beam length 90 μm, the resonance frequency first decreases and then increases with increasing heating power, indicating the MEMS beam is initially flat. For a MEMS beam with L = 94 μm, the resonance frequency increases with increasing heating power, indicating the MEMS beam is buckled from the beginning.
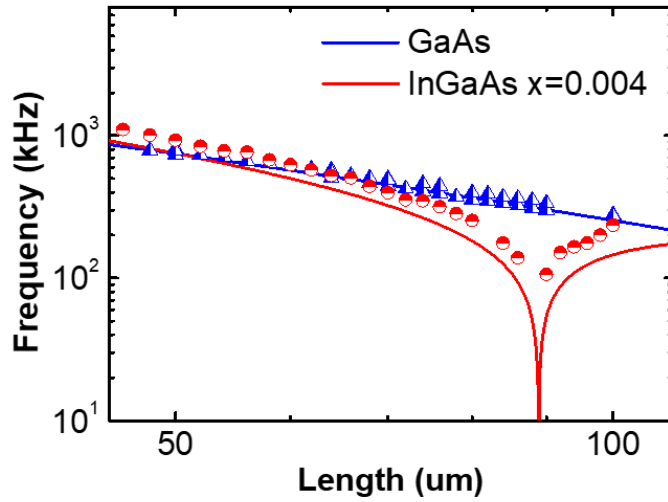
Fig. 4-9 Resonance frequency of GaAs and InGaAs samples as a function of the beam length. Dots: experimental results; line: theory.
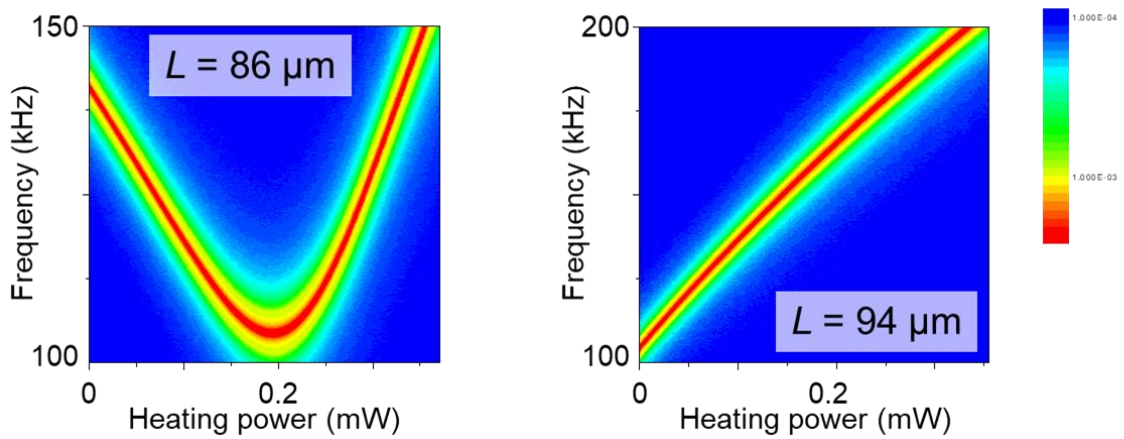
Fig. 4-10 Color-coded resonance spectra of the InGaAs MEMS beams as a function of heating power, (a): $L = 86$ μm and (b): $L = 94$ μm.

4.5   Enhanced thermal responsivity of InGaAs MEMS beam

Finally we measured the thermal responsivity of the InGaAs samples. In Fig. 4-11 we plot the responsivities as a function of the beam length for GaAs and InGaAs samples. We can see a peak in the responsivity for the InGaAs samples and the peak is located at L = 90 μm. When the MEMS beam is 90 μm-long, the responsivity of the InGaAs sample shows 2400 W^{-1}, which is 15 time higher than that of the standard GaAs samples. The result shows that by preloading compressive strain we can obtain a higher responsivity without sacrificing the thermal conductivity and sacrificing the detection speed.

However, the resonance frequency at the buckling point does not decrease to zero as shown in Fig. 4-10(a), indicating that the MEMS beam has a deflection around 10 nm. As a result, the thermal responsivity at the peak value is not as high as calculation.
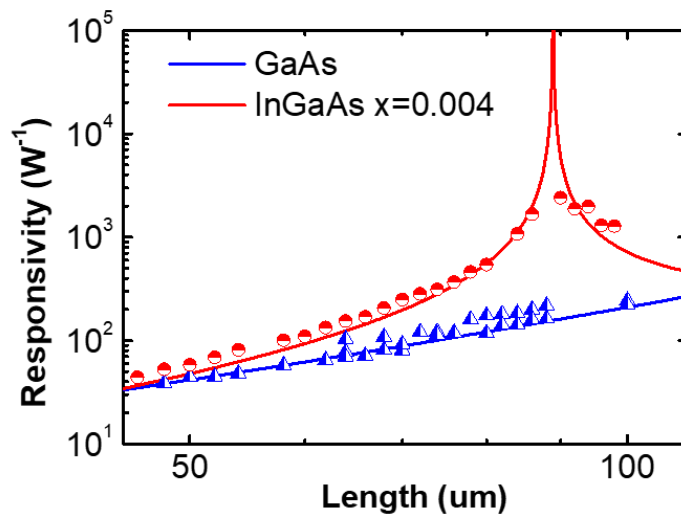
Fig. 4-11 Responsivity of GaAs and InGaAs samples as a function of the beam length. Dots: experimental results; line: theory.

## 4.6　　　Effect of vibration amplitude on the resonance frequency

By approaching the critical buckling point, the MEMS beam becomes very sensitive to internal strain such as thermal strain. As a result, thermal responsivity of the InGaAs beam is increased by 15 times. Other kinds of internal strain, such as the strain due to the beam vibration which is usually ignored for GaAs samples, also becomes crucial in the InGaAs samples. In this section, we introduce about how the vibration amplitude affect the resonance of InGaAs MEMS beams, and in the next section, the relationship of frequency noise on the vibration amplitude is discussed.

Equation of motion of the MEMS resonator can be expressed as:[73]

$$\ddot{x} + 2\Gamma\dot{x} + \alpha_1 x + \alpha_3 x^3 + \alpha_5 x^5 = (F_{ac}/m)\cos(\omega_d t), \qquad (4.3)$$

where x defines the beam vibration which is a function of time, F_{ac} is the driving force, and α_i contains contributions from restoring force of the spring. Here, the model contains nonlinear terms up to the fifth order, in order to figure out the complexed frequency response. As a result of the x^5 term, a four-order ω in the dependence of resonance frequency on the vibration amplitude a is generated as

$$\omega \approx \omega_1 + \kappa a^2 + \eta a^4. \qquad (4.4)$$

Eq. 4.4 solves the resonance frequency of MEMS beam from Eq. 4.3, where $\omega_1^2 = \alpha_1$ is the eigenfrequency, coefficient κ and η can be either positive or negative, depending on the spring nonlinearity coefficients. Inset curves in Fig. 4-12 plots the resonance spectrum when the driving amplitude F_{ac} is small. For small F_{ac}, the vibration amplitude is small and the $\alpha_5 x^5$ in Eq. 4.3 and the term ηa^4 in Eq. 4.4 can be neglected. In this case, the system reduces to the periodically driven underdamped Duffing oscillator[55,74–76] and ω is dominated by spring nonlinearity coefficient κ: with a positive cubic nonlinearity contribution, the resonance curve bends towards high frequency, as plotted in the inset curve (a) in Fig. 4-12; with a zero cubic nonlinearity

contribution, the asymmetry in the resonance peak is largely gone and the peak is well fitted by the response of a damped harmonic oscillator, as plotted in the inset curve (b); for a negative cubic nonlinearity contribution, the resonance curve bends towards a lower frequency, as plotted in the inset curve (c) in Fig. 4-12.

Such phenomenon is called Duffing effect of resonators, and it can also be explained in view of strain. For large vibration amplitude, the MEMS beam seems to be "stretched", and it works as if a periodic tensile strain is introduced to the MEMS beam. For a larger amplitude, there is a larger tensile strain. Fig. 4-12 plots the frequency-strain relationship of a deflected MEMS beam. Before the buckling point, a tensile strain makes the resonance frequency increase, the resonance spectrum bends to a higher frequency,[77,78] while after the buckling point a tensile strain makes the resonance frequency decrease and the resonance spectrum tills to a lower value.[79,80]

When the vibration amplitude becomes larger, the term ηa^4 in Eq. 4.4 cannot be neglected.[81,82] When the signs of κ and η are opposite, ω possesses a parabolic minimum as a function of a^2. In the view of strain, for a sample slightly exceeds the buckling point, with increasing vibration amplitude, the resonance curve first bends to lower frequency, and reaches the minimum resonance frequency at the buckling point, then bends to higher frequency with larger vibration amplitude.

Fig. 4-13 shows a schematic resonance spectrum of MEMS beam slightly exceeds the buckling point and vibrates with a large amplitude.[83–87] The solid lines are stable branches which can be measured in experiment and dashed lines are unstable. Arrows marks up- and down- sweep of frequency in experiment. The frequency response shows 4 bifurcation points noted B_i, at which the vibration amplitude jumps to destination points D_i on stable branches.[88] As the frequency is swept up from f_0, the output voltage follows the path $f_0 - D_2 - B_1 - D_1 - D_3 - f_1$. As the frequency is swept down from f_1, the path $f_1 - D_3 - D_1 - B_4 - D_4 - B_2 - D_2 - f_0$ is followed. The resonance peak B_3 can be obtained by manually control the driving frequency, following the path $f_1 - D_3 - D_1 - B_4 - D_4 - B_3 - D_3 - f_1$.
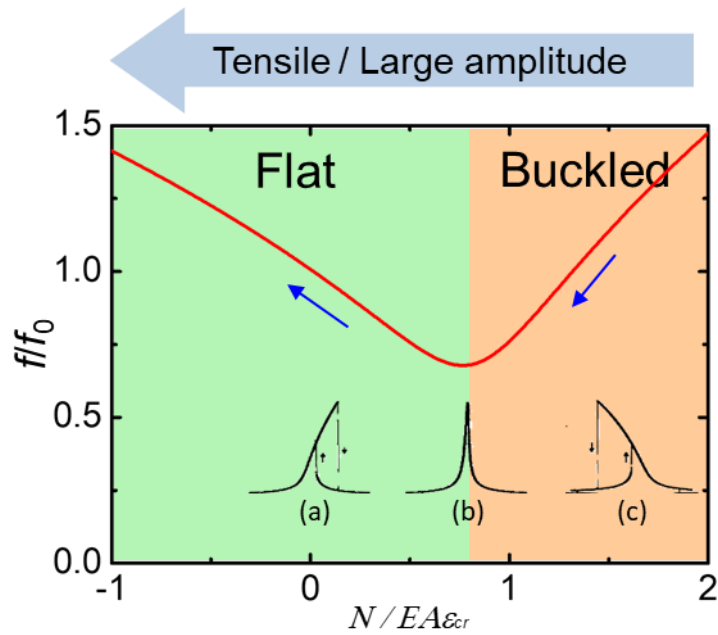
Fig. 4-12 Resonance frequency shift when vibration amplitude increase for a flat / buckled MEMS beam. Inset figures shows the corresponding resonance spectrum.
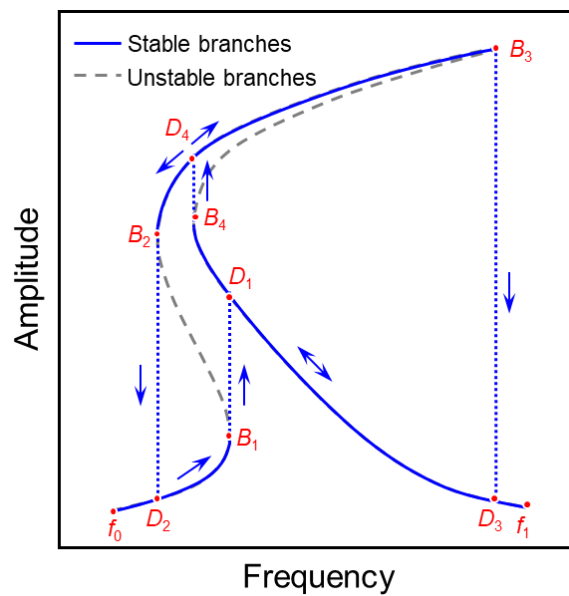
Fig. 4-13 Analytical resonance spectrum of MEMS beam around the buckling point. B_i are four bifurcation points where a jump of amplitude happens during frequency sweeping, and D_i ares the destination points after jumps. The two branches $\{B_1, B_2\}$ and $\{B_3, B_4\}$ in dashed lines are unstable.

The 90 μm InGaAs MEMS beam is very close to the buckling point and suitable for demonstrating such a phenomenon. We measured the InGaAs sample at different driving amplitude V_{in}. At small V_{in}, the resonance spectrum appears like Fig. 4-12(c), until $V_{in} = 127$ mV, the resonance frequency reaches a local minimum. With larger V_{in}, the resonance frequency again starts to increase. Fig. 4-14 plots the resonance spectrum of $V_{in} = 150$ mV, in which the 4 bifurcation points can be clearly observed. Fig. 4-15 summaries the resonance frequency as a function of vibration amplitude. The vibration amplitude is measured by using Doppler vibrometer. By plotting the resonance frequency as a function of a^2, the curve can be fitted by a parabola:

$$f = 193.9\text{kHz} - 1.86 \times 10^{15}a^2 + 1.93 \times 10^{28}a^4. \tag{4.5}$$

Around vibration amplitude of 200nm the resonance frequency reaches a local minimum, at which

$$\frac{df}{dA} = 0. \tag{4.6}$$

In this case the resonance frequency has no sensitivity to the vibration amplitude. Since such relationship prevents the amplitude noise transfer into frequency noise, the phenomenon can be utilized for reducing the frequency noise of the MEMS resonator.
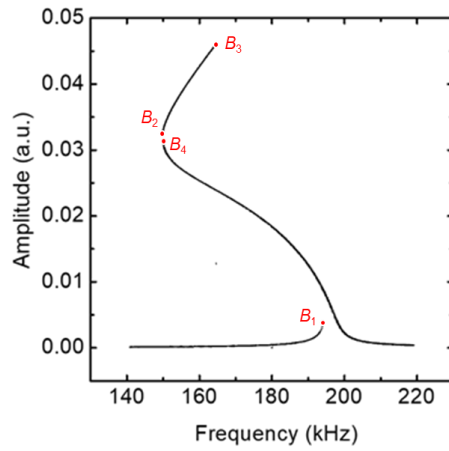
Fig. 4-14 Measured resonance spectrum of 90 μm InGaAs MEMS beam. The four bifurcation points B_i are denoted.
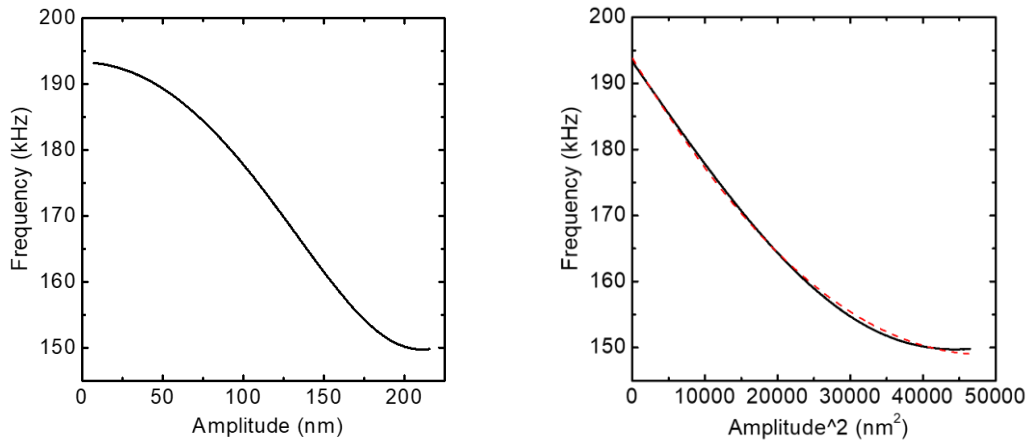
Fig. 4-15 Resonance frequency as a function of vibration amplitude a and a^2 of 90 μm InGaAs MEMS beam. The red dashed line is a parabolic fitting of resonance frequency as a function of a^2.

4.7   Frequency noise of InGaAs MEMS resonator

Frequency noise of the MEMS bolometer can be understood in terms of electrical and mechanical noise. The frequency noise N_f is given by

$$N_f = \sqrt{N_{fs}^2 + N_m^2}.$$

(4.7)

Here, N_{fs} denotes the blue noise from the measurement system including the piezo transducer and electrical circuit, which can be written as:

$$N_{fs} = \sqrt{2}\frac{n_{zs}}{A}f_m,$$

(4.8)

where n_{zs} the noise density, f_m the modulation frequency and A the vibration amplitude of the MEMS beam. N_{fs} is proportional to f_m.

N_m denotes the frequency noise from the mechanical resonator, which consists of two parts; i.e., fluctuations in f_0 resulting from the Duffing effect as discussed in last section, N_{fD}, and from the thermal Brownian motion, N_{fB}. N_{fD} is in shape of $1/f_m$ noise, and N_{fB} is a kind of white noise which can be written as:

$$N_{fB} = \sqrt{\frac{k_B T f_0}{\pi k Q A^2}}.$$

(4.9)

As shown in the equations, both the system noise N_{fs} and the thermal Brownian noise N_{fB} are inversely proportional to the vibration amplitude, thus using large vibration amplitude is a good way to reduce the frequency noise.

Fig. 4-16 plots the resonance spectrum of a standard GaAs MEMS beam measured as the driving amplitude is increased from 10 mV to 140 mV. Fig. 4-17 summarizes the resonance frequency as a function of the vibration amplitude. As seen in the figure, the

resonance frequency increases quadratically with increasing driving voltage.

Fig. 4-18 plots measured noise spectra for a GaAs MEMS beam at various driving amplitude. As seen in the plot, for $f_m < 200$Hz, a $1/f_m$ noise component due to the Duffing effect dominates. The amplitude of the $1/f_m$ noise increases with vibration amplitude, corresponding to a steeper slope in Fig. 4-17. For $f_m > 200$Hz, a blue noise (noise density proportional to f_m) dominates, which is the system noise N_{fS}. Such a noise is reduced with increasing vibration amplitude. Therefore, it is better to operate the MEMS resonator with a large amplitude for low noise. At large driving amplitude of $V_d > 200$ mV, the system noise is suppressed, and the device again limited by the $1/f_m$ noise N_{fD}. The Brownian noise, N_{fB}, is always smaller value than N_{fD} and cannot be seen in this sample.

However, for InGaAs MEMS resonators, we can suppress the $1/f_m$ noise by adjusting the vibration amplitude, when the resonance frequency reaches a local minimum, we expect the Duffing effect is dramatically suppressed. Fig. 4-19 plots noise spectrum measured from a 90 μm InGaAs MEMS beam with various driving amplitude. With V_d increase from 50 mV to 100 mV, the noise level does not decrease by half, and we consider at $V_d = 100$ mV the noise is limited by the $1/f_m$ noise. Furthermore, we increase the driving amplitude to 120 mV. From the previous data we know the resonance frequency now reaches the local minimum, and we can see the whole spectrum shift downward by 2/3. This result shows that we can reduce the frequency noise in InGaAs by adjusting the vibration amplitude.
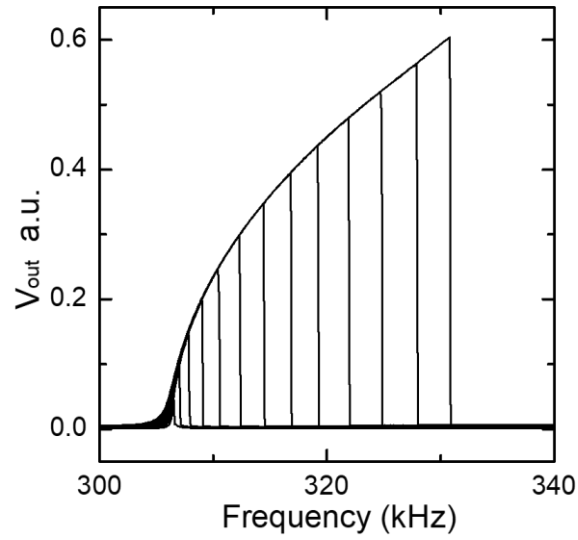
Fig. 4-16 Resonance spectrum of standard GaAs MEMS beam as driving amplitude V_d increase from 10 mV to 140 mV.
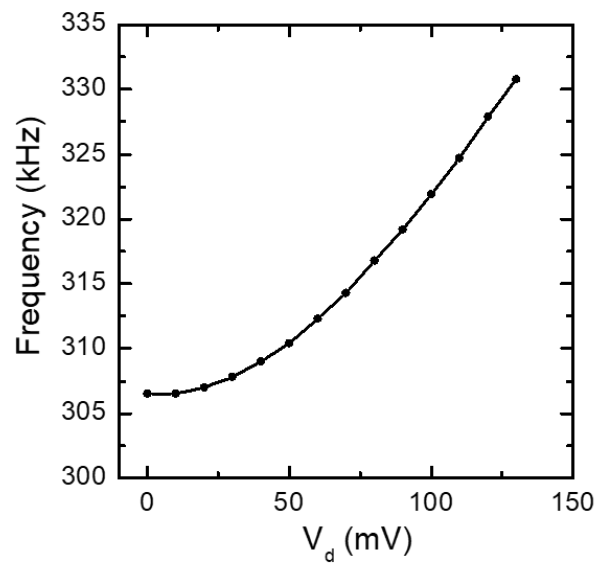
Fig. 4-17 Resonance frequency as a function of driving amplitude V_d.
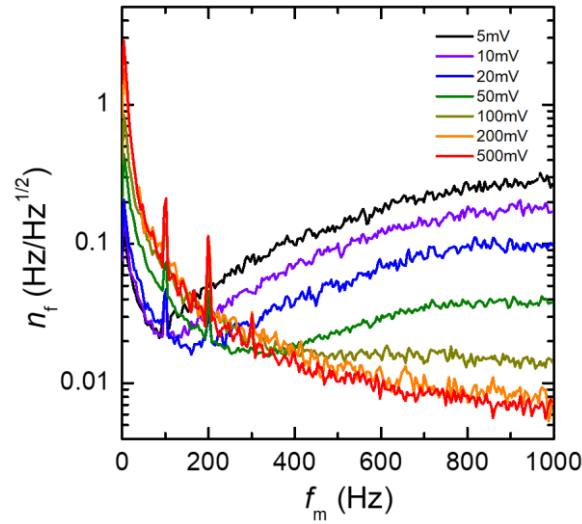
Fig. 4-18 Frequency noise of GaAs MEMS beam as a function of modulation frequency, when the MEMS beam is driven at various driving voltages.
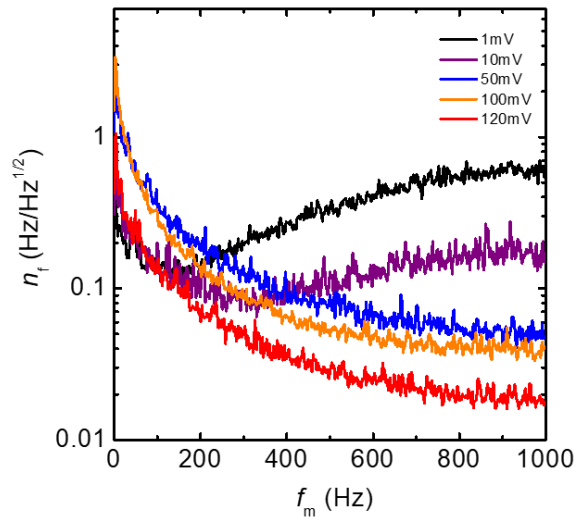
Fig. 4-19 Frequency noise of 90 μm InGaAs MEMS beam as a function of modulation frequency, when the MEMS beam is driven at various driving voltages.

4.8   Summary

To summary, we have proposed a novel method for improving the responsivities of the recently developed MEMS bolometer without deteriorating the detection speed, by utilizing the critical buckling phenomenon. We introduce a compressive strain in the MEMS beam using $In_xGa_{1-x}As$ as the beam material and apply a critical buckling strain to the beam. We have successfully increased the responsivity by 15 times without sacrificing the detection speed.

We also found that the InGaAs MEMS beam around the buckling point has a local minimum of frequency against the vibration amplitude, where the resonance frequency has no sensitivity with the vibration amplitude. Such phenomenon prevents the vibration noise transferring to the frequency noise, and helps reducing the frequency noise of the InGaAs MEMS resonator.

Chapter 5

Piezoresistive detection of the MEMS beam

5.1   Introduction

We are using a GaAs MEMS beam resonator to detect THz radiation at room temperature. The vibration of the MEMS beam is detected through the piezoelectric effect, as shown in Fig. 5-1(a), a voltage will be generated on the capacitor C_2 when the MEMS beam has a deformation. However, the output voltage from the piezoelectric capacitor is very small, because it is shunted by the stray capacitance of measurement cables. Fig. 5-2 plots the resonance spectra of a 200 μm MEMS beam, detected by using a piezoelectric capacitor. Signal amplitude is typically ~1 μV and for applications we need to use a buffer amplifier to suppress the effects of the stray capacitance.

On the other hand, in order to increase the thermal detection speed of the MEMS bolometer, shorter MEMS beams are preferred, of which the area of piezoelectric capacitors will be furthermore reduced. The capacitance can be calculated as

$$C_2 = \frac{\varepsilon_r A}{4\pi k d},$$
(5.1)

which is proportional to the electrode area, leading that the output voltage will become smaller for shorter MEMS beams. Therefore, we need to find another detection method before we shorten the MEMS beam for higher detection speed.

In this chapter, we propose to use the piezoresistive detection scheme, instead of the piezoelectric effect, to detect the MEMS beam vibration. Fig. 5-1(b) shows the scheme of the device. The resistance of R_x will be changed when the MEMS beam has a deformation. Since the resistance is decided by *L/W* ratio of the resistance sheet, we expect the output signal will not decrease for short MEMS beams. At the same time, by optimizing the piezoresistive material, we expect to increase the output signal to larger than 1 mV, so we can detect the signal directly without amplification.
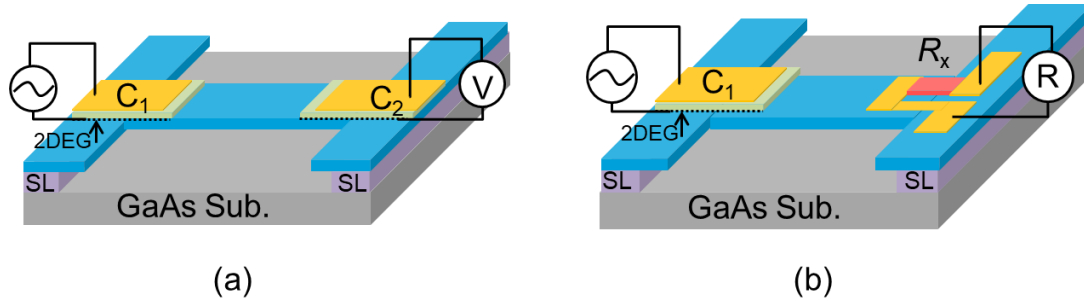
Fig. 5-1 Scheme of (a) piezoelectric detection and (b) piezoresistive detection.
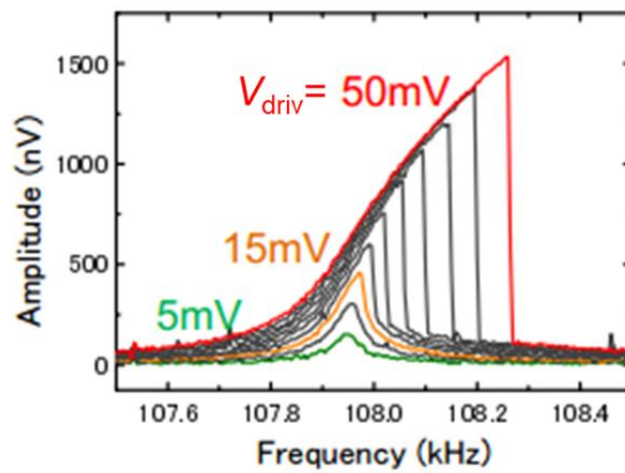
Fig. 5-2 Resonance spectra of a 200 μm MEMS beam detected by piezoelectric detection scheme.

5.2　　Piezoresistive detection using metal film

Firstly, we use NiCr film as the piezoresistive material to detect the MEMS beam vibration. Resistance of the NiCr film on MEMS beam will change due to its dimension change.[89–93] Fig. 5-3 shows an image of the fabricated sample. A piezoresistor R_x is placed at right end of the MEMS beam, whose resistance changes when the MEMS beam has a strain. By comparing the resistance of R_x and a reference resistor R_0, an output voltage V_o can be obtained as the vibration signal. V_o caused by the resistance change ΔR_x is calculated as:

$$V_o = V_{DD}\left(\frac{R_x+\Delta R_x}{R_0+R_x+\Delta R_x} - \frac{R_x}{R_0+R_x}\right), \tag{5.2}$$

where V_{DD} is the source voltage. When $R_0 \approx R_x$, V_o can be expressed as:

$$V_o = \frac{\Delta R_x}{4R_x}V_{DD}. \tag{5.3}$$

As seen, the output voltage is in proportional to the source voltage V_{DD}. Fig. 5-4 shows the measured resonance spectra of a 100 μm MEMS beam, when we linearly increase V_{DD} from 700 mV to 1.5 V. The amplitude of output voltage is less than 10 μV, and will linearly increase with V_{DD}. At the same time, the resonance frequency decreases with increasing V_{DD}, which is due to the heating effect on R_x. We can also convert the output into the change of resistance, $\Delta R_x/R_x$, as shown in Fig. 5-5. The change in resistance is around 15 ppm (parts per million) and does not change with V_{DD}, since the driving of MEMS beam is not changed.

Compared with the piezoelectric detection, the output signal of MEMS beam vibration V_o increases from several times by adopting the piezoresistive detection. However, the signal is still very small and we need an amplifier to measure the signal. If we look at the principle of piezoresistive effect, for metallic films, the resistance change is dominated by dimension change of the metal film after applying a strain. In

the strain direction it becomes shorter, and in the perpendicular direction it becomes fatter. As a result, for metallic films, the factor of relative resistance change divided by strain is around 2, and the resistance change is typically in the 10^{-6} order. On the other hand, for semiconductors, applying strain can change the band structure and the carrier mobility change may be much larger. Therefore, in the next we investigate semiconductor material as the piezoresistor.
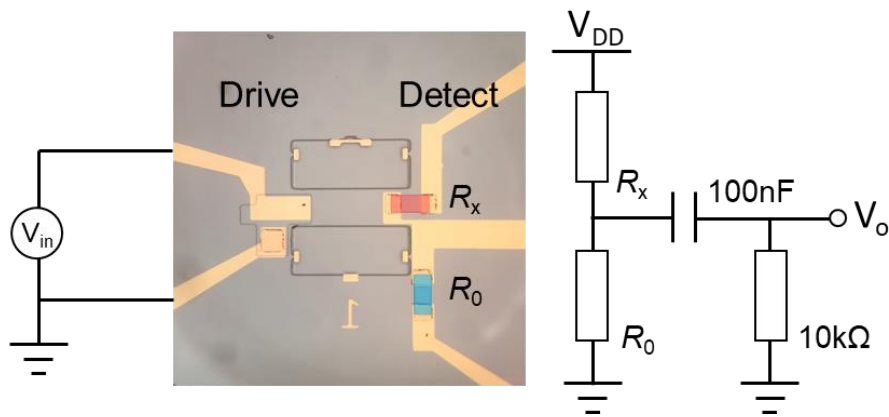
Fig. 5-3 Sample design and measurement circuit of piezoresistive detection.
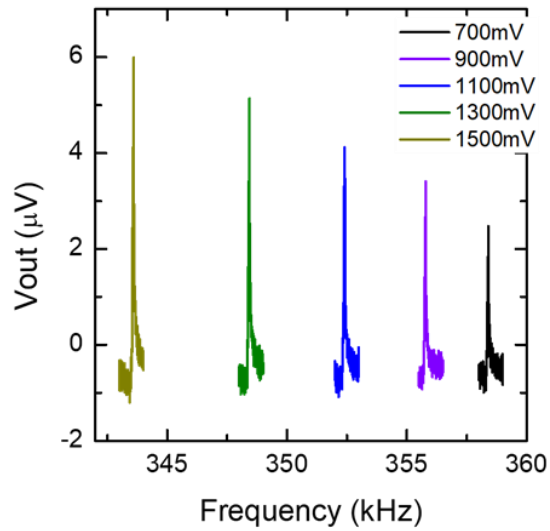
Fig. 5-4 Resonance spectra of the NiCr piezoresistive detection sample with linearly increasing the source voltage V_{DD}.
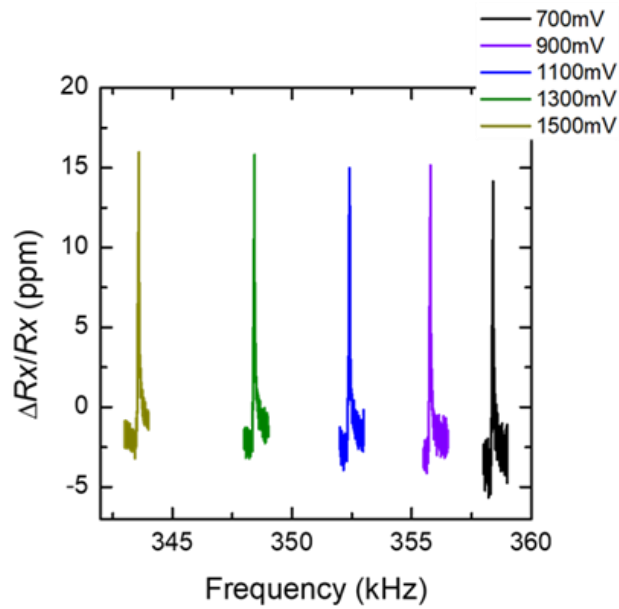
Fig. 5-5 Relative resistance change in the NiCr piezoresistive detection sample with linearly increasing the source voltage V_{DD}.

5.3   Piezoresistive detection using 2-dimensional electron gas

In this section we use the 2-dimensional electron gas (2DEG) in AlGaAs/GaAs heterojunctions on the beam surface as a piezoresistive material.[94–97] The 2DEG is used for bottom electrode of the piezoelectric capacitors, and we do not need to change the wafer design and fabrication process.

We fabricated samples with 2DEG as the piezoresistive material. The sample design and measurement circuit are same as Fig. 5-3. We first measured the vibration amplitude of the sample, by using a doppler vibrometer. Fig. 5-6 plots the vibration amplitude as a function of the driving voltage, which shows a linear relationship. According to the result, we fix the driving voltage at 27 mV, and the vibration amplitude of the beam keeps about 200 nm. Then we measured the resonance spectrum by using piezoresistive detection. Fig. 5-7 shows the result. With $V_{DD} = 2$ V, the output signal $V_o = 24$ μV and we can calculate the resistance change $\Delta R_x / R_x = 48$ ppm.

By using 2DEG as the piezoresistive material, the resistance change is not dramatically increased. This is due to the singly degenerated conduction band of GaAs, of which the electron mobility will not be affected significantly by strain. However, for the valence bands of GaAs, it has three branches and a strain can affect its degeneracy. Therefore, we can expect a significant change of the valence band structure and a large resistance change by applying strain.
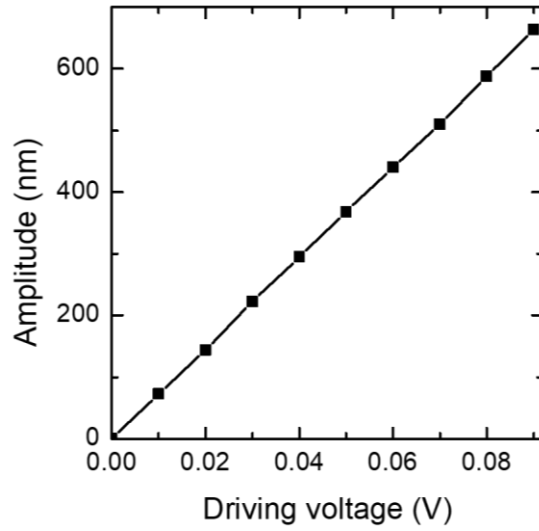
Fig. 5-6 Vibration amplitude of 100 μm MEMS beam as a function of the driving voltage.
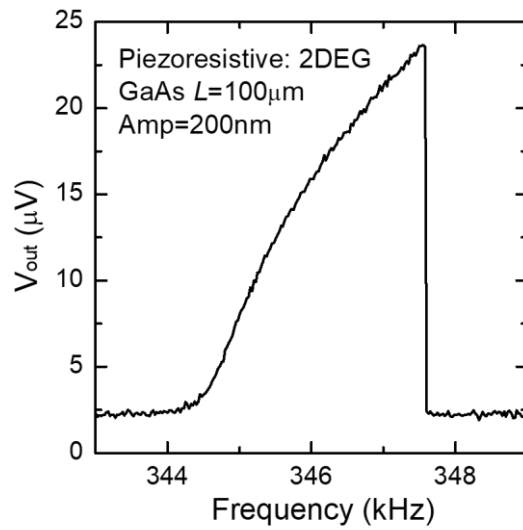
Fig. 5-7 Resonance spectrum measured with piezoresistive detecion. The vibration amplitude is 200 nm.

5.4 Piezoresistive effect of 2-dimensional hole gas

Owing to the singly degenerate conduction band of GaAs, electron mobility is not affected significantly by strain, and resulting resistance change of 2DEG is not. On the other hand, the valence band of GaAs has three branches and shows a complicated structure.[98–101] Therefore, the hole mobility is expected to change significantly under strain. In the following a piezoresistive detection realized by using two-dimensional hole gas (2DHG) will be introduced.

Two-dimensional hole gas (2DHG) in GaAs exhibits a piezoresistive feature due to spin-orbit coupling and band mixing of holes. Spin-orbit coupling is the interaction of electron spin with its orbital motion, as a consequence of relativistic effects,[99,102–105] and it results in the splitting of the uppermost valance band of GaAs into states with a total angular momentum $j = 3/2$ and $j = 1/2$. Fig. 5-8 shows a schematic plot of the valence band structure near the Γ point of a GaAs bulk crystal. The $j = 3/2$ states are fourfold degenerate at the Γ point, consisting of two subbands separated in energy at the in-plane wave vector $k_\parallel \neq 0$: the heavy-hole (HH) subband with a z component of angular momentum $m = \pm 3/2$ and the light-hole (LH) subband with $m = \pm 1/2$. The HH (LH) subbands refer to the higher (lower) effective mass of the holes for the motion along the growth axis, for in-plane motion their character is reversed, the HH states have a smaller effective mass characterizing the in-plane motion than the LH states have.

The subband structure of 2DHG in GaAs consists of individual HH and LH subbands. In contrast to bulk, a size quantization along the growth axis z takes place in 2DHG, and lifts the size quantization of HH band. As a result, the HH and LH subbands are separated. This HH-LH splitting causes mixing of HH and LH subbands, and the HH-LH anticrossing takes place, as illustrated in Fig. 5-8. Fig. 5-9 plots the hole subband dispersions of a [001] GaAs/Al$_{0.5}$Ga$_{0.5}$As heterojunction ($N_s = 7.6 \times 10^{11}$ cm^{-2}), where the anticrossings are clearly visible.
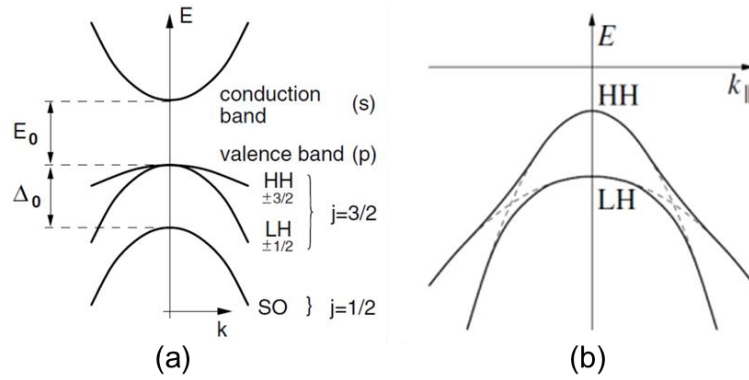
Fig. 5-8 (a) Qualitative sketch of GaAs band structure near the Γ point.[99] (b) Scheme of the HH-LH anticrossing in a 2DHG.[99]
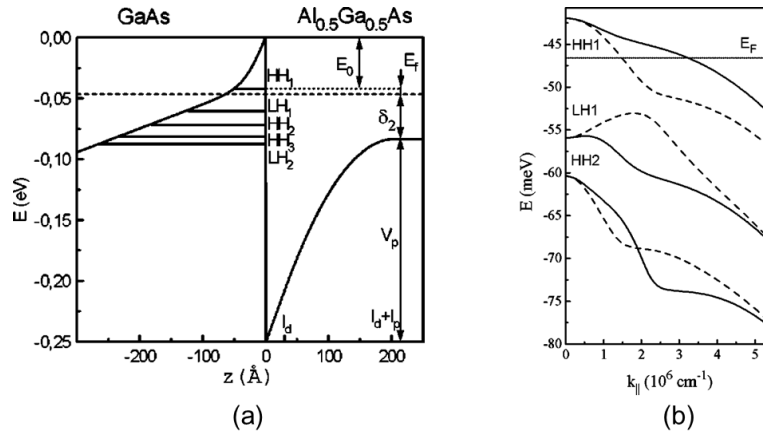
Fig. 5-9 (a) Calculated valence-band edge for a [001] GaAs/Al$_{0.5}$Ga$_{0.5}$As heterojunction ($N_s = 7.6 \times 10^{11}$ cm^{-2}).[98] (b) Energy of the first three hole subbands in the [001] GaAs/Al$_{0.5}$Ga$_{0.5}$As heterojunction versus $k_\parallel$ parallel to [110] direction.[98]

Such a band mixing effect makes the 2DHG states anisotropic and nonparabolic, and as a result, the subbands are found to depend strongly on uniaxial stress. Fig. 5-10 plots (a) the subband energies, (b) hole concentration, (c) effective mass and (d) relative resistance as a function of external uniaxial compression applied along [110]. Results shows that a uniaxial compression strongly affect the Fermi-surface topology of 2DHG, which reduce the difference between the effective masses (Fig. 5-10(b)) and the carrier concentrations in the subband of the hole ground state (Fig. 5-10(c)), and finally result in a strong piezoresistive effect.
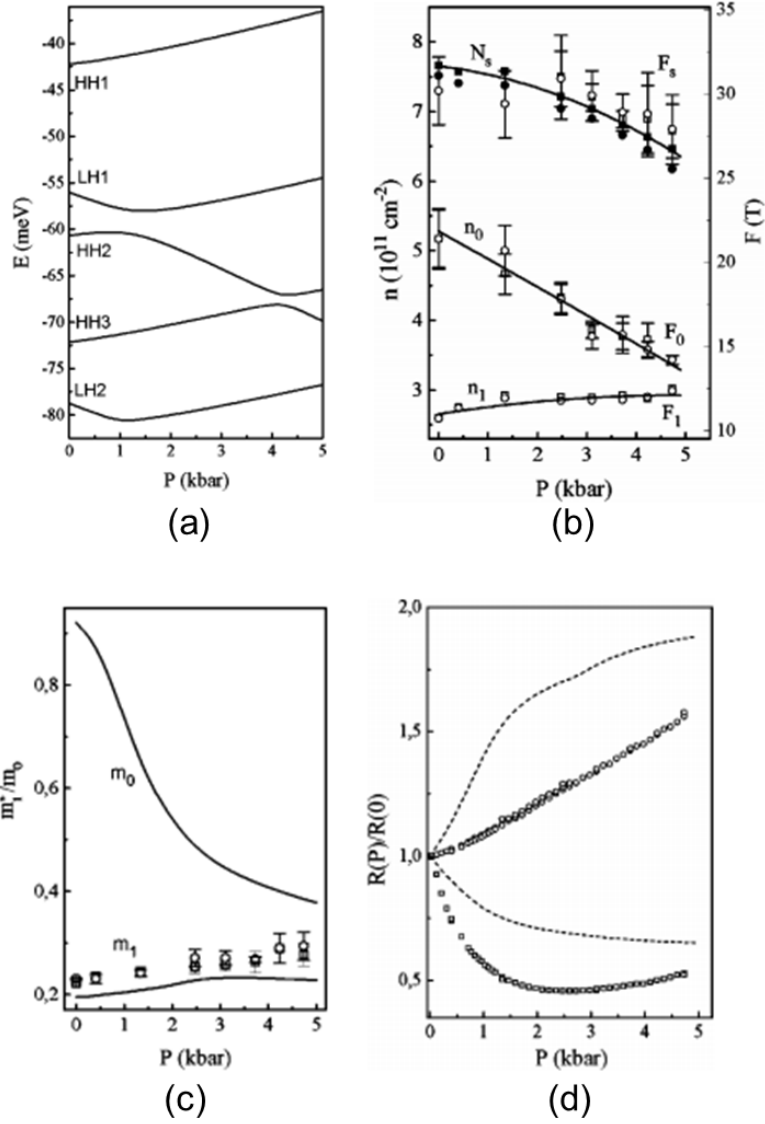
Fig. 5-10 (a) Energy of hole subbands, (b) hole concentration in HH (denoted as n_1) and LH (n_0) subbands, (c) effective masses of holes in HH (m_1) and LH (m_0) subbands and (d) relative resistance in the [001] GaAs/Al$_{0.5}$Ga$_{0.5}$As heterojunction as a function of external uniaxial compression applied along [110].[98]

5.5   Piezoresistive detection using 2-dimensional hole gas

5.5.1   Wafer structure

In order to obtain a strong piezoresistive effect and increase the output rf signal of the MEMS beam vibration, we propose to use 2D hole gas (2DHG) as the piezoresistive material to detect the MEMS beam vibration. Fig. 5-11 shows the designed wafer structure. We formed a 2DHG in the wafer by using modulation-doped AlGaAs/GaAs heterostructures. Fig. 5-12 shows the calculated band structure. Holes accumulate at the interface of GaAs and undoped AlGaAs spacer layer.

Table 5.1 shows a result of Hall measurements of the grown wafer at room temperature as well as liquid N_2 temperature (77K). At room temperature, the hole density N_s is high but shows low mobility, while at 77K there is less hole density but much higher mobility. This result indicates that in the grown wafer, free holes exists not only in 2DHG, but also in the doping region. Both types of the holes will contribute to the piezoresistive effect. However, since the size quantization only happens in the 2DHG, free holes in the doping region does not show large piezoresistive effect and degrade the output voltage.

Table 5.1 Hall measurement result of the p-GaAs wafer.

Temperature	R_s (ohm/sq)	RHs (m^2/C)	Mobility (cm^2/V·s)	N_s (/cm^2)
297K (RT)	8054	+89.8	111	+6.952*10^{12}
77K (LN$_2$)	1094	+245	2.25*10^3	+2.547*10^{12}
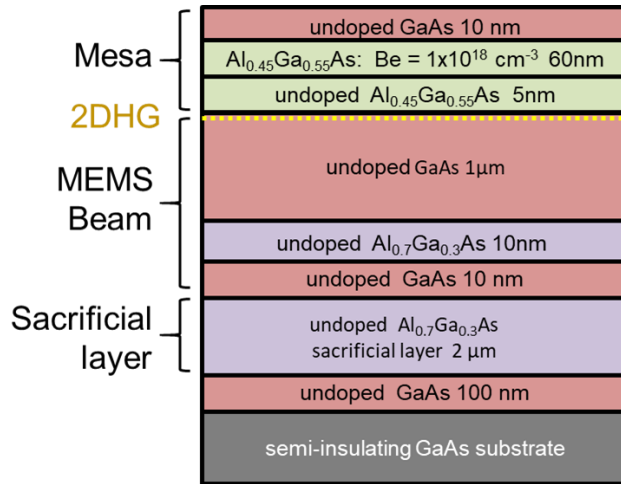
Fig. 5-11 Wafer structure of 2DHG piezoresistive sample.
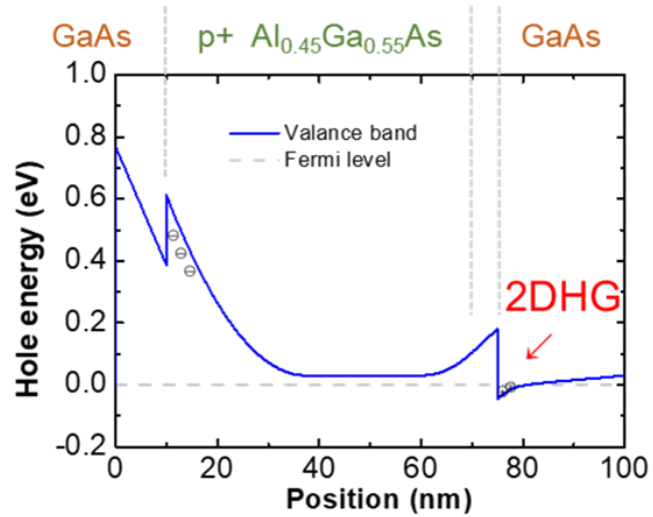
Fig. 5-12 Band structure of 2DHG piezoresistive sample.

5.5.2 Piezoresistive detection using 2-dimensional hole gas

We fabricated samples for piezoresistive detection using 2DHGs and measured the output signal. The MEMS beam and the piezoresistor were both set along the [110] direction. Fig. 5-13 shows a microscope image of a fabricated sample and a measurement result. R_0 and R_x were both around 20 kΩ. V_{DD} was set at 2 V. With a driving amplitude V_{in} of 50 mV, we obtained an output signal $V_{pp} = 2.96$mV as shown in the inset.

Fig. 5-14 plots the resonance spectra of the sample at various driving voltage V_{in} form 10mV to 140mV. We see the output rf signal increases with increasing V_{in}. We expect the output rf signal can be increased to more than 10 mV if we increase V_{in} furthermore. The resonance frequency is around 320kHz and it shifts to higher frequency with increasing driving amplitude of the beam, due to the Duffing effect.

Fig. 5-15 plots the frequency noise of the sample. With increasing V_{in}, low frequency noise increase and high frequency noise decrease, which is a standard behavior for a Duffing oscillator. The measured minimum frequency noise is 7mHz/Hz$^{1/2}$, at a modulation frequency of 1kHz. With higher modulation frequency the frequency noise will decrease but it was not measured due to a limitation of the equipment. For the previous piezo-capacitive measurement, the lowest frequency noise was around 4mHz/Hz$^{1/2}$. The observed difference in frequency noise may be due to the Nyquist noise on the large resistor R_0 and R_x.
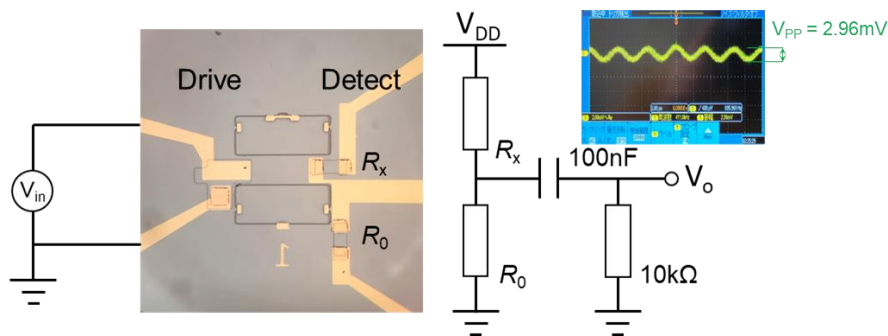
Fig. 5-13 Sample of 2DHG piezoresistive detection and measurement circuit. The inset figure shows the output signal measured by the oscilloscope.
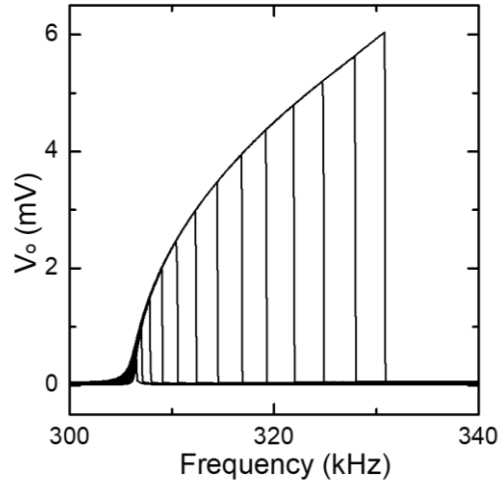
Fig. 5-14 Measured resonance spectra of the 2DHG piezoresistive detection sample with linearly increasing driving amplitude.
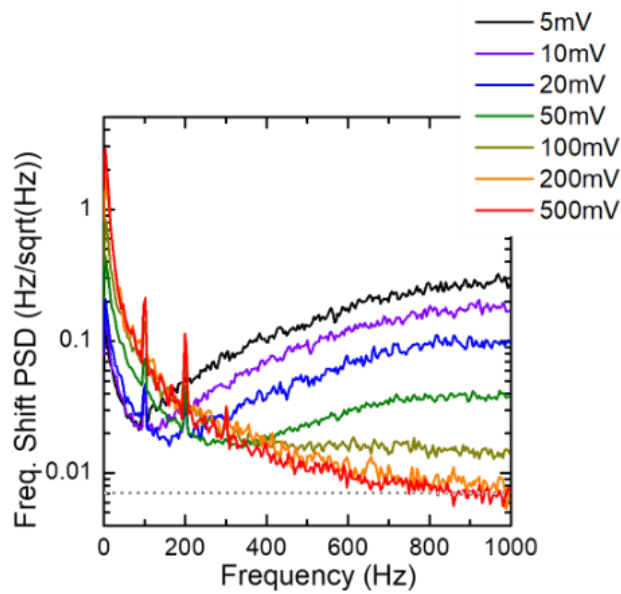
Fig. 5-15 Frequency noise of the 2DHG piezoresistive detection sample as a function of modulation frequency, when the MEMS beam is driven at various dricing voltages.

5.6 Factors affecting the piezoresistive detection

Next, some factors that will affect the performance of piezoresistive detection are discussed.

5.6.1 Joule heating of detection resistor

Since we apply a source voltage V_{DD} to R_x to measure the resistance, joule heat is generated and heat the MEMS beam. Fig. 5-16 plots the resonance spectra as V_{DD} increases from 0 to 5.0V. As V_{DD} increases, the MEMS beam is heated and the resonance frequency shift to lower frequency. On the other hand, the output signal increases with V_{DD}, as expected in Eq. 5.3. However, the relationship between output signal and V_{DD} is not strictly linear. Fig. 5-17 plots the amplitude of output signal as a function of V_{DD}. The amplitude of the output signal superlinearly increases with V_{DD}, which is different with the expectation from Eq. 5.3.

Fig. 5-18 plots the relative resistance change as a function of V_{DD}. By using 2DHG as the piezoresistive material, a resistance change of ~1% is observed, with is 1000 times of that of NiCr metal film. On the other hand, even though the vibration amplitude doesn't change, with increasing V_{DD} the resistance change slightly increase, such difference may be due to temperature rise of the 2DHG layer.
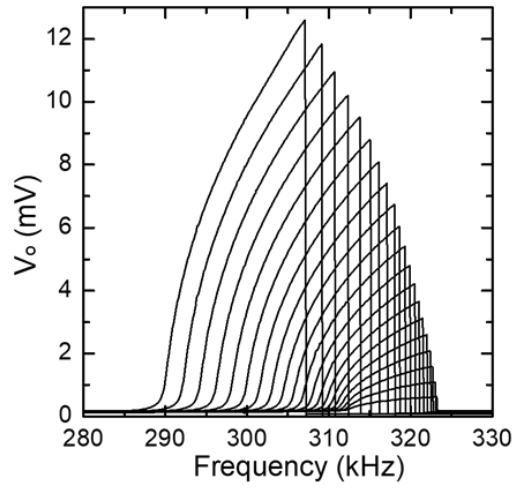
Fig. 5-16 Resonance spectra of the 2DHG piezoresistive detection sample with linearly increasing the source voltage V_{DD}.
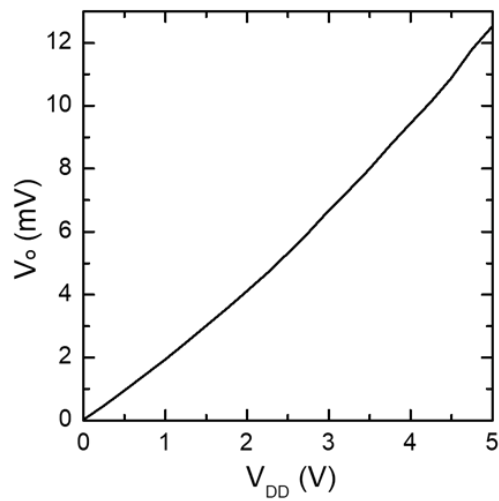
Fig. 5-17 Output signal amplitude of the 2DHG piezoresistive detection sample as a function of the source voltage V_{DD}.
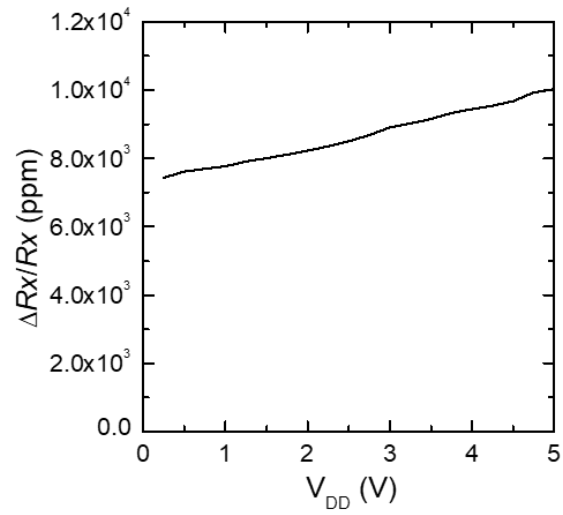
Fig. 5-18 Relative resistance change of the 2DHG piezoresistive detection sample as a function of the source voltage V_{DD}.

5.6.2　Orientation dependence of the piezoresistive detection

Crystallographic orientation of the piezoresistive detection system also affects the detection performance. Fig. 5-19 shows a polar plot of the absolute value of the piezoresistive constants calculated for p-GaAs in {001} plane. The piezoresistive constant is defined as the ratio of relative resistance change and the stain applied to the material. For samples discussed in section 5.5, the MEMS beam was placed along the [110] direction, which is parallel with the direction of current flow in the piezoresistor. In this case, piezoresistive constant can be estimated from the solid line in Fig. 5-19, and in the [110] direction we expect the highest piezoresistive constant.

We fabricated samples in which the MEMS beam and piezoresistor were placed along different directions. All the samples here were of the longitudinal type due to the limited beam area. Results for samples with 0°, 30° and 45° rotation from the [110] direction is listed in Table 5.2. The V_{DD} is fixed at 2V. We used a Doppler vibrometer to measure the vibration amplitude. And, at same time measure the output voltage amplitude from the piezoresistive detector. Since the vibration amplitude is proportional to the internal strain, we can compare the piezoresistive constants for different orientations by comparing the value of V_o / amplitude.

As seen in Table 5.2, by changing the orientation, the piezoresistive constants can be changed by more than 10 times. Therefore, it is important to fix the orientation of the MEMS beam and the piezoresistor. One more thing is that, because of the limited MEMS beam area, currently the piezoresistor is parallel with strain direction. However, as seen in Fig. 5-19, the perpendicular case has a higher piezoresistive constant, which is worth trying in future works.
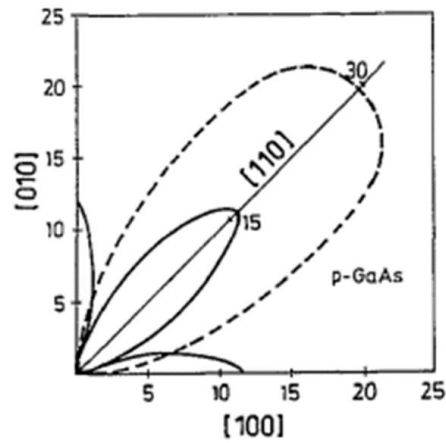
Fig. 5-19 Polar plot of the piezoresistive constants of p-GaAs for longitudinal (solid line) and transverse (dashed line) effect in {001} plane.[106] The unit is 10^{-11} Pa^{-1}

Table 5.2 Results of piezoresistive detection in different orientation

Shift from [110]	Amplitude (nm)	V_o (mV)	V_o / amplitude (V/m)
0°	523.6	1.99	3800
30°	257.1	0.57	2217
45°	21.89	0.0065	297

5.7   Summary

In this chapter we discuss the detection scheme of the MEMS beam resonator. Previously we used a piezoelectric capacitor to detect the vibration of MEMS beam. However, due to the stray capacitance of measurement cables, the output signal is typically less than 1μV and we need to use a buffer amplifier to suppress the effects of stray capacitance.

To enhance the signal, we propose to use a piezoresistive effect instead of piezo-capacitive effect to detect the MEMS beam vibration. Since the resistance is determined by *L/W* ratio of a resistor, the limited MEMS beam area does not decrease the signal amplitude. Performance of different piezo-resistive material is compared. For metallic films such as NiCr, the resistance change is dominated by the dimension change of the metal film and in our case the output signal is less than 10μV. On the other hand, for semiconductors, applying strain can change the band structure and the carrier mobility change can be thousand times larger. We first tried to use the 2DEG in MEMS beam as the piezoresistive material. However, due to the singly degenerate conduction band structure of GaAs, the electron mobility cannot be modulated significantly by strain, and the output signal is around 20μV.

Valence band of GaAs has three branches and shows a complicated structure. Therefore, the hole mobility is expected to change significantly under strain. We propose to use a 2D hole gas as the piezoresistive material to detect the beam vibration. The signal amplitude of the beam vibration by detected using 2DHG shows an rf voltage as large as 6mV and the resistance changes is calculated to be 1%, which is 1000 times larger than that of metallic films. Finally, factors that will affect the 2DHG piezoresistive detection are studied. Large source voltage applied to the piezoresistor can lead to a large output signal amplitude, but also will generate a joule heating which will heat the MEMS beam, and shift its resonance frequency. On the other hand, orientation of the piezoresistor is of higher importance. Results shows that a MEMS beam and piezoresistor in the [110] direction has the best detection efficiency, and in

the [100] direction the efficiency will be reduced by 90%. Thus it is very important to fix the orientation of piezoresistive detection.

Chapter 6
Conclusion and outlook

6.1   Conclusions

In this thesis, effect of internal strain and detection scheme on doubly clamped MEMS beam is investigated for THz bolometer applications. Previously, we reported a very sensitive bolometer structure by using a GaAs doubly clamped beam resonator. The MEMS resonator detects THz radiation by measuring a shift in its resonance frequency induced by heating of the MEMS beam due to THz absorption. Speed of the device can be up to 10kHz, which is much faster than other kinds of room temperature THz thermal sensors. The MEMS bolometers are superior to other room-temperature THz bolometers, but still not comparable with the low temperature detectors in aspect of the sensitivity and speed.

In this thesis, we have proposed to obtain the high sensitivity and high speed of the MEMS bolometer by using short InGaAs MEMS beam detected by piezoresistive detection. This method can evade the speed-sensitivity trade-off of the MEMS bolometer. Changing the beam material to InGaAs provides a high thermal responsivity, the short MEMS beam provides a high speed and the piezoresistive detection provides a large output voltage.

We first discussed about the beam deflection. Such a deflection of the beam brings difference from the theory to the experiment result of the MEMS bolometers and makes it difficult to predict the devices' performance. There are two factors that induce the beam deflection. First is the initial bending of MEMS beam. This kind of initial bending will increase with the MEMS beam length. In order to reduce the initial bending, we introduce a tensile strain to the MEMS beam using GaAsP as the beam material and induce a lattice mismatch against the GaAs substrate. Results shows that the deflection reduces from 150 nm to 50 nm, and the responsivities of long MEMS beams are enhanced. Another factor of the beam deflection is the mesa structure on the beam surface. We find that, a step structure on two ends of the beam will effectively induce a deflection of the MEMS beam. By reducing the step height, the beam deflection is reduced to as small as 10 nm.

For sample with a small deflection, the thermal responsivity of the beam can be enhanced by 6 times around its buckling point. To achieve this responsivity enhancement, we propose to introduce a critical buckling strain to the MEMS beam by using InGaAs as beam material. This method can evade the speed-sensitivity trade-off of the MEMS bolometer and make it available to achieve high responsivity and high speed of the device at the same time. In order to adjust the compressive strain and set the MEMS beam exactly around the buckling point, we propose to change the MEMS beam length instead of changing the indium composition. By fabricating a MEMS beam of 90 μm, we achieve a thermal responsivity as high as 2400 W^{-1}, which is 15 time higher than that of the standard GaAs samples. The 90 μm InGaAs MEMS beam also shows a mixed behavior between hardening and softening beam resonator. By utilizing this phenomenon, we observe a frequency stabilized region of the MEMS resonator, in which the resonance frequency will not change with fluctuating driving amplitude, and the frequency noise of the device is suppressed.

Since the speed-sensitivity trade-off is evaded, short beams can exhibit a high sensitivity and high speed at same time. However, the piezo-capacitive detection of the present device is not suitable for detecting vibration of short beam, because the output voltage from the piezoelectric capacitor is shunted by the stray capacitance of measurement cables and shows smaller than 1 μV. Therefore, we need to develop another detection scheme. To enhance the output voltage, we propose to use a piezoresistive effect to detect the MEMS beam vibration. Since the resistance is determined by L/W ratio of a resistor, the short beam length does not decrease the output voltage. We have tried to use metallic film (NiCr) as well as semiconductive material (2DEG and 2DHG) as the piezoresistive material. Results shows that the output voltage detected by 2DHG shows as large as 10mV which is 10000 times of that of the piezo-capacitive detection. Effect of the source voltage and crystallographic orientation of the piezoresistor is discussed. Results shows that in the [110] direction, the piezoresistive constant shows maximum.

6.2   Outlook

We have proposed to obtain the high sensitivity and high speed of the MEMS bolometer by using short InGaAs MEMS beam detected by piezoresistive detection. We believe the knowledge we have obtained from this research will be useful for the developing of the MEMS bolometers Furthermore, with the MEMS beam size reduced to 10 µm level, which is the THz wavelength range, the device can be coupled with traditional THz antenna such as bowtie antenna, which provides a high absorption efficiency of THz radiation and improves the device sensitivity. Also, the integration of MEMS beam arrays becomes easier by adopting the piezoresistive scheme, and finally broaden the scope of application of the MEMS bolometer.

Reference

1. Ishigaki K, Shiraishi M, Suzuki S, Asada M, Nishiyama N, Arai S. Direct intensity modulation and wireless data transmission characteristics of terahertz-oscillating resonant tunnelling diodes. *Electron Lett*. 2012;48(10):582-583.

2. Semenov A, Pohl A, Hübers HW, et al. Schottky diode detectors for monitoring coherent THz synchrotron radiation pulses. In: *Proceedings of the 5th International Particle Accelerator Conference*. ; 2014.

3. Sizov F, Rogalski A. THz detectors. *Prog quantum Electron*. 2010;34(5):278-347.

4. Bozhkov VG. Semiconductor detectors, mixers, and frequency multipliers for the terahertz band. *Radiophys Quantum Electron*. 2003;46(8):631-656.

5. Richards PL. Bolometers for infrared and millimeter waves. *J Appl Phys*. 1994;76(1):1-24.

6. Mauskopf PD, Bock JJ, Del Castillo H, Holzapfel WL, Lange AE. Composite infrared bolometers with Si 3 N 4 micromesh absorbers. *Appl Opt*. 1997;36(4):765-771.

7. Nishioka NS, Richards PL, Woody DP. Composite bolometers for submillimeter wavelengths. *Appl Opt*. 1978;17(10):1562-1567.

8. Niklaus F, Vieider C, Jakobsen H. MEMS-based uncooled infrared bolometer arrays: a review. In: *MEMS/MOEMS Technologies and Applications III*. Vol 6836. International Society for Optics and Photonics; 2008:68360D.

9. Rogalski A. Infrared detectors for the future. *Acta Phys Pol A Gen Phys*. 2009;116(3):389.

10. Oda N, Yoneyama H, Sasaki T, et al. Detection of terahertz radiation from quantum cascade laser using vanadium oxide microbolometer focal plane arrays. In: *Infrared Technology and Applications XXXIV*. Vol 6940. International Society for Optics and Photonics; 2008:69402Y.

11. Stowe TD, Yasumura K, Kenny TW, Botkin D, Wago K, Rugar D. Attonewton force detection using ultrathin silicon cantilevers. *Appl Phys Lett*. 1997;71(2):288-290.

12. Boisen A, Dohn S, Keller SS, Schmid S, Tenje M. Cantilever-like micromechanical sensors. *Reports Prog Phys*. 2011;74(3):36101.

13. Ekinci KL, Huang XMH, Roukes ML. Ultrasensitive nanoelectromechanical mass detection. *Appl Phys Lett*. 2004;84(22):4469-4471.

14. Dohn S, Sandberg R, Svendsen W, Boisen A. Enhanced functionality of cantilever based mass sensors using higher modes. *Appl Phys Lett*. 2005;86(23):233501.

15. Yang Y-T, Callegari C, Feng XL, Ekinci KL, Roukes ML. Zeptogram-scale nanomechanical mass sensing. *Nano Lett*. 2006;6(4):583-586.

16. Jensen K, Kim K, Zettl A. An atomic-resolution nanomechanical mass sensor. *Nat Nanotechnol*. 2008;3(9):533-537.

17. Pang W, Yan L, Zhang H, Yu H, Kim ES, Tang WC. Femtogram mass sensing platform based on lateral extensional mode piezoelectric resonator. *Appl Phys Lett*. 2006;88(24):243503.

18. Hanay MS, Kelber S, Naik AK, et al. Single-protein nanomechanical mass spectrometry in real time. *Nat Nanotechnol*. 2012;7(9):602-608.

19. Schmid S, Dohn S, Boisen A. Real-time particle mass spectrometry based on

resonant micro strings. *Sensors*. 2010;10(9):8092-8100.

20. Ilic B, Czaplewski D, Zalalutdinov M, et al. Single cell detection with micromechanical oscillators. *J Vac Sci Technol B Microelectron Nanom Struct Process Meas Phenom*. 2001;19(6):2825-2828.

21. Naik AK, Hanay MS, Hiebert WK, Feng XL, Roukes ML. Towards single-molecule nanomechanical mass spectrometry. *Nat Nanotechnol*. 2009;4(7):445-450.

22. Sharos LB, Raman A, Crittenden S, Reifenberger R. Enhanced mass sensing using torsional and lateral resonances in microcantilevers. *Appl Phys Lett*. 2004;84(23):4638-4640.

23. Cleland AN, Roukes ML. A nanometre-scale mechanical electrometer. *Nature*. 1998;392(6672):160-162.

24. Knobel R, Yung CS, Cleland AN. Single-electron transistor as a radio-frequency mixer. *Appl Phys Lett*. 2002;81(3):532-534.

25. Buehler TM, Reilly DJ, Starrett RP, et al. Development and operation of the twin radio frequency single electron transistor for cross-correlated charge detection. *J Appl Phys*. 2004;96(8):4508-4513.

26. Turin VO, Korotkov AN. Numerical analysis of radio-frequency single-electron transistor operation. *Phys Rev B*. 2004;69(19):195310.

27. Aassime A, Johansson G, Wendin G, Schoelkopf RJ, Delsing P. Radio-frequency single-electron transistor as readout device for qubits: Charge sensitivity and backaction. *Phys Rev Lett*. 2001;86(15):3376.

28. Masmanidis SC, Tang HX, Myers EB, et al. Nanomechanical measurement of magnetostriction and magnetic anisotropy in (Ga, Mn) As. *Phys Rev Lett*. 2005;95(18):187206.

29. Onomitsu K, Mahboob I, Okamoto H, Krockenberger Y, Yamaguchi H. Ferromagnetic-induced component in piezoresistance of GaMnAs. *Phys Rev B*. 2013;87(6):60410.

30. Pandey AK, Gottlieb O, Shtempluck O, Buks E. Performance of an AuPd micromechanical resonator as a temperature sensor. *Appl Phys Lett*. 2010;96(20):203105.

31. Larsen T, Schmid S, Grönberg L, et al. Ultrasensitive string-based temperature sensors. *Appl Phys Lett*. 2011;98(12):121901.

32. Larsen T, Schmid S, Boisen A. Micro string resonators as temperature sensors. *AIP Conf Proc*. 2013;1552 8:931-936. doi:10.1063/1.4819669

33. Laurent L, Yon J-J, Moulet J-S, Roukes M, Duraffourg L. 12− μ m-pitch electromechanical resonator for thermal sensing. *Phys Rev Appl*. 2018;9(2):24016.

34. Zhang XC, Myers EB, Sader JE, Roukes ML. Nanomechanical torsional resonators for frequency-shift infrared thermal sensing. *Nano Lett*. 2013;13(4):1528-1534.

35. Hui Y, Rinaldi M. Fast and high resolution thermal detector based on an aluminum nitride piezoelectric microelectromechanical resonator with an integrated suspended heat absorbing element. *Appl Phys Lett*. 2013;102(9):93501.

36. Yamada S, Schmid S, Larsen T, Hansen O, Boisen A. Photothermal infrared spectroscopy of airborne samples with mechanical string resonators. *Anal Chem*. 2013;85(21):10531-10535.

37. Larsen T, Schmid S, Villanueva LG, Boisen A. Photothermal analysis of

individual nanoparticulate samples using micromechanical resonators. *ACS Nano*. 2013;7(7):6188-6193.

38. Gokhale VJ, Rais-Zadeh M. Uncooled infrared detectors using gallium nitride on silicon micromechanical resonators. *J Microelectromechanical Syst*. 2013;23(4):803-810.

39. Duraffourg L, Laurent L, Moulet J-S, Arcamone J, Yon J-J. Array of resonant electromechanical nanosystems: a technological breakthrough for uncooled infrared imaging. *Micromachines*. 2018;9(8):401.

40. Zhang Y, Watanabe Y, Hosono S, Nagai N, Hirakawa K. Room temperature, very sensitive thermometer using a doubly clamped microelectromechanical beam resonator for bolometer applications. *Appl Phys Lett*. 2016;108(16):163503.

41. Zhang Y, Hosono S, Nagai N, Hirakawa K. Effect of buckling on the thermal response of microelectromechanical beam resonators. *Appl Phys Lett*. 2017;111(2):23504.

42. Zhang Y, Hosono S, Nagai N, Song S-H, Hirakawa K. Fast and sensitive bolometric terahertz detection at room temperature through thermomechanical transduction. *J Appl Phys*. 2019;125(15):151602.

43. Zhang Y, Qiu B, Nagai N, Nomura M, Volz S, Hirakawa K. Enhanced thermal sensitivity of MEMS bolometers integrated with nanometer-scale hole array structures. *AIP Adv*. 2019;9(8):85102.

44. Morohashi I, Irimajiri Y, Sekine N, et al. Active THz Imaging Using MEMS Resonator-Based Bolometer and Quantum Cascade Laser. In: *International Conference on Infrared, Millimeter, and Terahertz Waves, IRMMW-THz*. Vol 2018-Septe. ; 2018. doi:10.1109/IRMMW-THz.2018.8510107

45. Zhang Y, Qiu B, Nagai N, Nomura M, Hirakawa K. Enhanced sensitivity of MEMS bolometers by introducing two-dimensional phononic crystal structures. In: *Optics InfoBase Conference Papers*. Vol Part F78-J. ; 2017.

46. Qiu B, Zhang Y, Hosono S, Akahane K, Nagai N, Hirakawa K. GaAsP microelectromechanical beam structures for terahertz bolometer applications. In: *Optics InfoBase Conference Papers*. Vol Part F78-J. ; 2017.

47. Zhang Y, Yoshioka Y, Morohashi I, Liu X. 1:1 internal mode coupling strength in GaAs doubly-clamped MEMS beam resonators with linear and nonlinear oscillations. *Appl Phys Express*. 2021;14(1):1-6. doi:10.35848/1882-0786/abd198

48. Mahboob I, Yamaguchi H. Bit storage and bit flip operations in an electromechanical oscillator. *Nat Nanotechnol*. 2008;3(5):275-279.

49. Brueckner K, Niebelschuetz F, Tonisch K, et al. Two-dimensional electron gas based actuation of piezoelectric AlGaN/GaN microelectromechanical resonators. *Appl Phys Lett*. 2008;93(17):173504.

50. Faucher M, Grimbert B, Cordier Y, et al. Amplified piezoelectric transduction of nanoscale motion in gallium nitride electromechanical resonators. *Appl Phys Lett*. 2009;94(23):233506.

51. Karabalin RB, Matheny MH, Feng XL, et al. Piezoelectric nanoelectromechanical resonators based on aluminum nitride thin films. *Appl Phys Lett*. 2009;95(10):103111.

52. Berthomieu C, Hienerwadel R. Fourier transform infrared (FTIR) spectroscopy. *Photosynth Res*. 2009;101(2):157-170.

53. Cleland AN, Krim J. *Foundations of Nanomechanics: From Solid-State Theory to Device Applications*. Vol 57.; 2004. doi:10.1063/1.1768678

54. Rao SS. Mechanical vibrations fifth edition in SI units. 2012.

55. Younis MI. *MEMS Linear and Nonlinear Statics and Dynamics*. Vol 20. Springer Science & Business Media; 2011.

56. Kim CS, Dickinson SM. The flexural vibration of slightly curved slender beams subject to axial end displacement. *J Sound Vib*. 1986;104(1):170-175. doi:10.1016/S0022-460X(86)80139-0

57. Bouwstra S, Geijselaers B. On the resonance frequencies of microbridges. In: *Dig. Tech. Papers 6th Int. Conf. Solid-State Sensors and Actuators*. ; 1991:24-27.

58. TIMOSHENKO S. VIBRATION PROBLEMS IN ENGINEERING. *Text*.

59. Kagawa S, Mikawa T, Kaneda T. Chemical Etching of Germanium with H3PO4–H2O2–H2O Solution. *Jpn J Appl Phys*. 1982;21(11R):1616.

60. Tahamtan S, Goodarzi A, Abbasi SP, Hodaei A, Zabihi MS, Sabbaghzadeh J. Investigation on the effect of annealing process parameters on AuGeNi ohmic contact to n-GaAs using microstructural characteristics. *Microelectron Reliab*. 2011;51(8):1330-1336.

61. Kumar P, Kanakaraju S, Devoe DL. Sacrificial etching of Al x Ga 1-x As for III–V MEMS surface micromachining. *Appl Phys A*. 2007;88(4):711-714.

62. Ukita H, Uenishi Y, Tanaka H. A photomicrodynamic system with a mechanical resonator monolithically integrated with laser diodes on gallium arsenide. *Science (80-)*. 1993;260(5109):786-789.

63. Wu XS, Coldren LA, Merz JL. Selective etching characteristics of HF for AlxGa1-xAs/GaAs. *Electron Lett*. 1985;21(13):558-559.

64. Jafri IH, Busta H, Walsh ST. Critical point drying and cleaning for MEMS technology. In: *MEMS Reliability for Critical and Space Applications*. Vol 3880. International Society for Optics and Photonics; 1999:51-58.

65. Popa LC, Weinstein D. Switchable piezoelectric transduction in AlGaN/GaN MEMS resonators. In: *2013 Transducers & Eurosensors XXVII: The 17th International Conference on Solid-State Sensors, Actuators and Microsystems (TRANSDUCERS & EUROSENSORS XXVII)*. IEEE; 2013:2461-2464.

66. Shevyrin AA, Pogosov AG, Budantsev M V., et al. The role of Euler buckling instability in the fabrication of nanoelectromechanical systems on the basis of GaAs/AlGaAs heterostructures. *Appl Phys Lett*. 2012;101(24). doi:10.1063/1.4772472

67. Yamaguchi H, Kato K, Nakai Y, Onomitsu K, Warisawa S, Ishihara S. Improved resonance characteristics of GaAs beam resonators by epitaxially induced strain. *Appl Phys Lett*. 2008;92(25):251913.

68. Onomitsu K, Mitsuhara M, Yamamoto H, Yamaguchi H. Ultrahigh-Q micromechanical resonators by using epitaxially induced tensile strain in GaNAs. *Appl Phys Express*. 2013;6(11):111201.

69. Yamaguchi H, Tokura Y, Miyashia S, Hirayama Y. Quantum Interference Effects in the Magnetopiezoresistance of I n A s/A l G a S b Quasi-One-Dimensional Electron Systems. *Phys Rev Lett*. 2004;93(3):36603.

70. Verbridge SS, Parpia JM, Reichenbach RB, Bellan LM, Craighead HG. High quality factor resonance at room temperature with nanostrings under high tensile stress. *J Appl Phys*. 2006;99(12):124304.

71.   Bellaiche L, Wei S-H, Zunger A. Band gaps of GaPN and GaAsN alloys. *Appl Phys Lett*. 1997;70(26):3558-3560.

72.   Noel JG. Review of the properties of gold material for MEMS membrane applications. *IET Circuits, Devices Syst*. 2016;10(2):156-161.

73.   Soskin S, Chan HB, Ninios K, Mannella R. Noise-induced spectral narrowing in a micro-electromechanical resonator. *2013 22nd Int Conf Noise Fluctuations, ICNF 2013*. 2013:23-26. doi:10.1109/ICNF.2013.6579009

74.   Nayfeh AH, Mook DT, Holmes P. Nonlinear oscillations. 1980.

75.   Dykman M. *Fluctuating Nonlinear Oscillators: From Nanomechanics to Quantum Superconducting Circuits*. Oxford University Press; 2012.

76.   Lifshitz R, Cross MC. Nonlinear dynamics of nanomechanical and micromechanical resonators. *Rev nonlinear Dyn Complex*. 2008;1(1).

77.   Aldridge JS, Cleland AN. Noise-enabled precision measurements of a duffing nanomechanical resonator. *Phys Rev Lett*. 2005;94(15):156403.

78.   Stambaugh C, Chan HB. Noise-activated switching in a driven nonlinear micromechanical oscillator. *Phys Rev B*. 2006;73(17):172302.

79.   Kozinsky I, Postma HWC, Bargatin I, Roukes ML. Tuning nonlinearity, dynamic range, and frequency of nanomechanical resonators. *Appl Phys Lett*. 2006;88(25):253101.

80.   Eichler A, del Álamo Ruiz M, Plaza JA, Bachtold A. Strong coupling between mechanical modes in a nanotube resonator. *Phys Rev Lett*. 2012;109(2):25503.

81.   Huang L, Soskin SM, Khovanov IA, Mannella R, Ninios K, Chan HB. Frequency stabilization and noise-induced spectral narrowing in resonators with zero dispersion. *Nat Commun*. 2019;10(1):1-10. doi:10.1038/s41467-019-11946-8

82.   Kacem N, Hentz S, Pinto D, Reig B, Nguyen V. Nonlinear dynamics of nanomechanical beam resonators: Improving the performance of NEMS-based sensors. *Nanotechnology*. 2009;20(27). doi:10.1088/0957-4484/20/27/275501

83.   Ouakad HM, Younis MI. Modeling and simulations of collapse instabilities of microbeams due to capillary forces. In: *ASME International Mechanical Engineering Congress and Exposition*. Vol 48746. ; 2008:187-195.

84.   Lenci S, Rega G. Control of pull-in dynamics in a nonlinear thermoelastic electrically actuated microbeam. *J Micromechanics Microengineering*. 2006;16(2):390.

85.   Gottlieb O, Champneys AR. Global bifurcations of nonlinear thermoelastic microbeams subject to electrodynamic actuation. In: *IUTAM Symposium on Chaotic Dynamics and Control of Systems and Processes in Mechanics*. Springer; 2005:117-126.

86.   Nayfeh AH, Balachandran B. Applied Nonlinear Dynamics, Wiley Series in Nonlinear Science. 1995.

87.   Kacem N, Hentz S. Bifurcation topology tuning of a mixed behavior in nonlinear micromechanical resonators. *Appl Phys Lett*. 2009;95(18):183104.

88.   Najar F, Nayfeh AH, Abdel-Rahman EM, Choura S, El-Borgi S. Dynamics and global stability of beam-based electrostatic microactuators. *J Vib Control*. 2010;16(5):721-748.

89.   Angadi MA, Whiting R. Longitudinal and transverse strain sensitivity of nichrome films. *Mater Sci Eng B*. 1990;7(1-2):L1. doi:10.1016/0921-5107(90)90020-C

90.   Kazi IH, Wild PM, Moore TN, Sayer M. The electromechanical behavior of nichrome (80/20 wt.%) film. *Thin Solid Films*. 2003;433(1-2 SPEC.):337-343. doi:10.1016/S0040-6090(03)00390-0

91.   Parker RL, Krinsky A. Electrical resistance-strain characteristics of thin evaporated metal films. *J Appl Phys*. 1963;34(9):2700-2708. doi:10.1063/1.1729795

92.   Ahmed M, Chitteboyina MM, Butler DP, Celik-Butler Z. MEMS Force sensor in a flexible substrate using nichrome piezoresistors. *IEEE Sens J*. 2013;13(10):4081-4089. doi:10.1109/JSEN.2013.2272881

93.   Sohgawa M, Hirashima D, Moriguchi Y, et al. Tactile sensor array using microcantilever with nickel-chromium alloy thin film of low temperature coefficient of resistance and its application to slippage detection. *Sensors Actuators, A Phys*. 2012;186:32-37. doi:10.1016/j.sna.2011.12.055

94.   Shkolnikov YP, Vakili K, De Poortere EP, Shayegan M. Giant low-temperature piezoreslstance effect in AlAs two-dimensional electrons. *Appl Phys Lett*. 2004;85(17):3766-3768. doi:10.1063/1.1808883

95.   Christensen NE. Electronic structure of GaAs under strain. *Phys Rev B*. 1984;30(10):5753.

96.   Okamoto H, Watanabe T, Ohta R, et al. Cavity-less on-chip optomechanics using excitonic transitions in semiconductor heterostructures. *Nat Commun*. 2015;6:1-6. doi:10.1038/ncomms9478

97.   Barlian AA, Park WT, Mallon JR, Rastegar AJ, Pruitt BL. Review: Semiconductor piezoresistance for microsystems. *Proc IEEE*. 2009;97(3):513-552. doi:10.1109/JPROC.2009.2013612

98.   Kolokolov KI, Savin AM, Beneslavski SD, Hansen OP. ʰʳˈ 2ˆ. 1999;59(11).

99.   Winkler R. *Spin Orbit Coupling Effects in Two-Dimensional Electron and Hole Systems*.; 2003. https://books.google.com/books?id=LQhcSCuzC3IC&pgis=1.

100.   Habib B, Shabani J, De Poortere EP, Shayegan M, Winkler R. Anisotropic low-temperature piezoresistance in (311) A GaAs two-dimensional holes. *Appl Phys Lett*. 2007;91(1):9-12. doi:10.1063/1.2753735

101.   Dehe A, Fricke K, Mutamba K, Hartnagel HL. A piezoresistive GaAs pressure sensor with GaAs/AlGaAs membrane technology. *J Micromechanics Microengineering*. 1995;5(2):139.

102.   Habib B. Spin-orbit interaction in GaAs two dimensional holes. 2007;(June).

103.   Shabani J, Shayegan M, Winkler R. Strain-induced fermi contour anisotropy of GaAs 2D holes. *Phys Rev Lett*. 2008;100(9):4-7. doi:10.1103/PhysRevLett.100.096803

104.   Hirmer M. High-mobility two-dimensional hole gases in III-V semiconductor heterostructures: growth and transport properties. 2013.

105.   Mughnetsyan V, Kirakosyan A. Strain distribution and band structure of InAs/GaAs quantum ring superlattice. *Superlattices Microstruct*. 2017;112:318-327. doi:10.1016/j.spmi.2017.09.041

106.   Landolt H, Börnstein R. Numerical Data and Functional Relationships in Science and Technology. *Gr III*. 1984;17.

List of publications

Journal papers:

Published journal paper:

   1. <u>Boqi Qiu</u>, Ya Zhang, Kouichi Akahane, Naomi Nagai, Kazuhiko Hirakawa. Effect of beam deflection on the thermal responsivity of GaAs-based doubly clamped microelectromechanical beam resonators[J]. Applied Physics Letters, 2020, 117(20): 203503.

Journal papers in preparing:

   2. <u>Boqi Qiu</u>, Ya Zhang, Naomi Nagai, Kazuhiko Hirakawa. Effect of surface step structure of on the thermal responsivity of GaAs-based doubly clamped MEMS beam resonators.

   3. <u>Boqi Qiu</u>, Ya Zhang, Naomi Nagai, Kazuhiko Hirakawa. Enhancement in thermal responsivities of doubly clamped InGaAs MEMS beam resonators by introducing a critical buckling strain.

   4. <u>Boqi Qiu</u>, Ya Zhang, Naomi Nagai, Kazuhiko Hirakawa. Frequency stabilization in doubly clamped InGaAs MEMS beam resonators.

   5. <u>Boqi Qiu</u>, Naomi Nagai, Kazuhiko Hirakawa. Piezoresistive detection of MEMS beam resonators using GaAs two-dimensional holes.

International conferences

   1. <u>Boqi Qiu</u>, Ya Zhang, Naomi Nagai, Kazuhiko Hirakawa. Enhancement in thermal responsivities of doubly clamped InGaAs MEMS beam resonators by introducing a critical buckling strain, CSW2021, WeC2-4, Online, May 2021.

   2. <u>Boqi Qiu</u>, Ya Zhang, Kouichi Akahane, Naomi Nagai, Kazuhiko Hirakawa. Effect of introducing phosphorous in the GaAs-based terahertz MEMS bolometers, HQS2019, LNP-11, Japan, Dec 2019.

   3. <u>Boqi Qiu</u>, Ya Zhang, Kouichi Akahane, Naomi Nagai, Kazuhiko Hirakawa. Suppressing beam deflections by introducing phosphorous in the GaAs-based terahertz MEMS bolometers, CSW2019, TuP-E-2, Japan, May 2019

4. <u>Boqi Qiu</u>, Ya Zhang, Kouichi Akahane, Naomi Nagai, Kazuhiko Hirakawa. Strain tuning in MEMS beam resonators for terahertz bolometer applications, IRMMW-THz 2018, Th-P2-1a-2, Japan, Sep 2018.

Domestic conferences

1. <u>Boqi Qiu</u>, Ya Zhang, Naomi Nagai, Kazuhiko Hirakawa. Piezoresistive detection of MEMS beam resonators for THz bolometer applications, JSAP Autumn meeting 2021, 13p-N105-13, Japan, Sep 2021 (to be presented).

2. <u>Boqi Qiu</u>, Ya Zhang, Naomi Nagai, Kazuhiko Hirakawa. Effect of the surface step structures on the responsivity of the MEMS terahertz bolometers, JSAP Spring meeting 2020, 18p-Z24-14, Japan, Sep 2021.

3. <u>Boqi Qiu</u>, Ya Zhang, Naomi Nagai, Kazuhiko Hirakawa. Enhancement in thermal responsivities of MEMS bolometers by introducing a critical buckling strain, JSAP Autumn meeting 2020, 12a-B414-10, Japan, Sep 2020.

4. <u>Boqi Qiu</u>, Ya Zhang, Kouichi Akahane, Naomi Nagai, Kazuhiko Hirakawa. Effect of introducing phosphorous in the GaAs-based terahertz MEMS bolometers, JSAP Spring meeting 2019, 20p-E206-7, Japan, Mar 2019.

5. <u>Boqi Qiu</u>, Ya Zhang, Naomi Nagai, Kazuhiko Hirakawa. Effect of the surface step structures on the responsivity of the MEMS, JSAP Autumn meeting 2018, 20p-212A-3, Japan, Sep 2018.